
UNIVERSITÀ DEGLI STUDI DI PADOVA

Dipartimento di Fisica e Astronomia "Galileo Galilei"

Master Degree in Physics


Final Dissertation

# Signal Formation Mechanisms in a Double Micro-Mesh Gaseous Detector Using the T2K Gas Mixture


Thesis supervisor

Prof. Gianmaria Collazuol

Thesis co-supervisor

Dr. Stefano Levorato

Candidate

Leo Mareso


Academic Year 2024/2025

# Abstract

As part of a major upgrade to the near detector of the T2K experiment, two gaseous Time Projection Chambers (TPCs), positioned above and below the active target, were constructed, installed, and brought into operation. Each High-Angle TPC features a large active volume enclosed by field cages with rectangular cross-sections and lightweight composite walls. Readout is performed by two planes, each equipped with eight Encapsulated Resistive Anode Micromegas (ERAM) detectors. A deep understanding of the detector, particularly the signal formation process, is crucial to fully exploit its performance.

This work investigates the signal induction mechanism in Micromegas-based gaseous detectors operating with the T2K gas mixture. Specifically, it aims to develop a detailed understanding of a novel Thick-GEM-like detector incorporating two micro-mesh layers. This sophisticated configuration enables the separation of the electron and ion components of the avalanche. The study combines simulations carried out with Garfield++ and experimental data obtained from a dedicated test setup, and both approaches confirm that, with an optimized detector configuration, the signal induced by electrons can be effectively isolated while the ion-induced component is significantly suppressed. This result is a valuable first step to have a detailed knowledge of the single components of the signals. Further studies on the detector would lead to a deeper understanding of the ion component of the signal, which still has several unclear aspects such as its ion composition and the mobility of each ion type in the gas mixture, and applications to detectors having a resistive anode layer.

# Introduction

T2K is a long baseline neutrino oscillation experiment located in Japan which has been running for the last 15 years. It largely contributed to precision measurements of the PMNS matrix parameters $\theta_{13}$, $\theta_{23}$ and $\Delta m^2_{23}$ and to constraints on the $CP$ violating phase $\delta_{CP}$ in the leptonic sector. During the last few years, the ND280 detector of T2K underwent a major upgrade to meet the requirements set by the recent progress in the research field and to compensate the weaknesses of the former detector revealed during its long lifetime. The upgrade includes the implementation of two large High Angle Time Projection Chambers (HA-TPC) in the detector, above and below the interaction point. Their purpose is to attain a better reconstruction and identification of the charged particles released at a high longitudinal angle with respect to the direction of the beam. Each TPC is made of a lightweight field cage, which defines the gas volume and the electric field inside the detector, and by endcaps hosting Encapsulated Resistive Anode Micromegas (ERAM) modules that read out the electric signal induced by the charges in the detector and allow the precise reconstruction of the incoming tracks. The maximum performance of these new detectors cannot be achieved without a good understanding of all of their peculiarities, the issues they might have and the countermeasures to solve them.

This thesis focuses on the study of the signal induction mechanism, that is the structure of the electric signal induced on the readout anode plane by the motion of charged particles in the detector. In particular, the main goal of this work is the suppression of the ion-induced component of the signal and the isolation of its electron-induced component by means of an original detector (DMM) specifically designed for the purpose.

*Chapter 1* will give an overview of the state of art of neutrino physics, discussing about the upcoming challenges and the experiments under construction to achieve these goals. *Chapter 2* will present the basic notions of T2K and TPCs to display the big picture and explain the root of this work. *Chapter 3* will then explain the fundamentals to understand how a gaseous detector works and show few applications which are commonly used in the experiments. *Chapter 4* is the simulation-related section of the work, and it will show the results of Monte Carlo simulations run on Garfield++ on the performance of Micromegas and DMM detectors. *Chapter 5* will report the results obtained in a real experimental setup, verifying the results obtained in the DMM simulations.

# Contents

# Chapter 1

# Neutrino oscillation physics

## 1.1 Neutrino overview

The existence of neutrinos was first proposed by Pauli in 1930 to try to explain the continuous energy spectrum of the outgoing electron in the $\beta$ decay. Their existence was confirmed in 1956 by the observation of the antineutrino-induced inverse $\beta$ decay in the Savannah River experiment by Reines and Cowan. Nearly 70 years have passed since then, but neutrinos are still particles that have a lot of unclear aspects. They are classified as leptons among the elementary particles of the Standard Model, and there is a flavor of neutrino for each family of charged leptons: electronic ($\nu_e$), muon ($\nu_\mu$) and tau ($\nu_\tau$) neutrino. One of their unique properties which causes them to be so obscure is the fact that they only can interact through the Weak interaction (except for the gravitational one). In fact they do not have electromagnetic charge or strong color charge, meaning that they do not leave any direct ionizing tracks inside the detectors. To this day, neutrinos can only be observed indirectly through the other products of its interaction. Moreover, because of their small cross section in general, detectors of large dimensions running for a long time period are required to be able to observe and study them with enough statistics. The most evident unknown is their mass. Researchers have been working on the issue for a long time, but only part of the puzzle has been put together. At first it was thought that neutrinos were massless particles like photons, as they appeared originally in the Standard Model theory. Over the years instead it was discovered thanks to the observation of neutrino oscillations that neutrinos, although small, have a massive nature. However, although progress has been made, only bounds have been set and the absolute values of the neutrino masses are yet to be determined.
Another less obvious trait which is now a focal point in neutrino research is the $CP$ violation phase value. This is a parameter which can be observed only considering the three-flavor neutrino oscillation, and the determination of its value is crucial for a better understanding of the different behavior between particles and antiparticles. This is a matter that involves even the mystery of the genesis of our matter-only universe, since

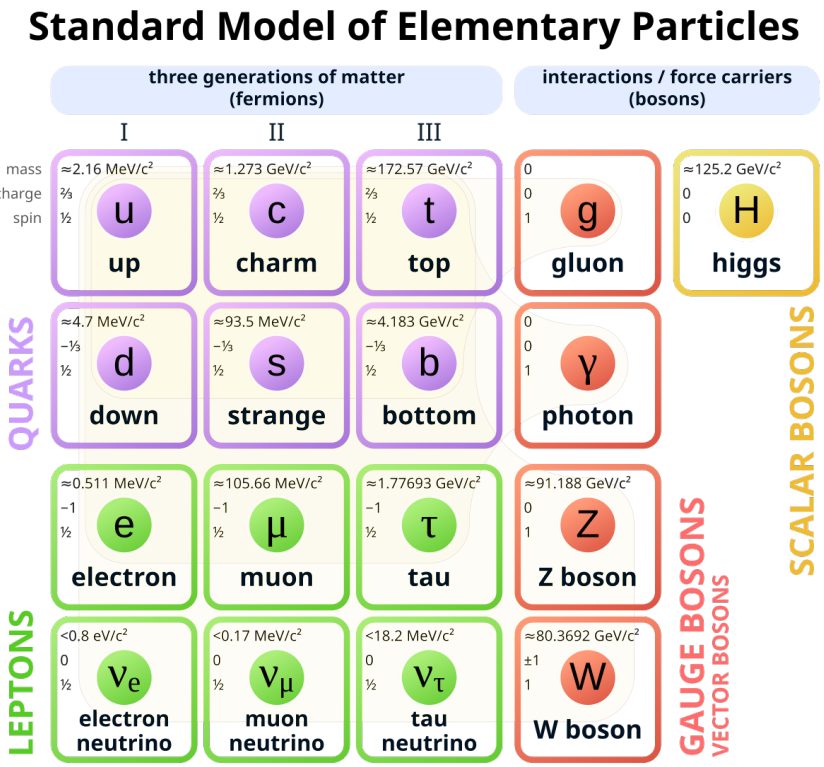


Figure 1.1: *Overview of the elementary particles of the Standard Model of particle physics. Each fermionic particle has its own antiparticle. The three neutrinos are named after their corresponding charged lepton, but they only interact through weak interactions mediated by either the W boson (Charged Current, CC interactions) or the Z boson (Neutral Current, NC interactions).*

$CP$ violation is one of the fundamental conditions that are necessary to explain such phenomenon. [1, 2, 3]

## 1.2 Flavor mixing and neutrino oscillations

Neutrinos have the peculiar property that their flavor and mass eigenstates do not coincide. This means that the flavor states $\nu_e$, $\nu_\mu$ and $\nu_\tau$ in which neutrinos interact are not equal to the mass states $\nu_1$, $\nu_2$ and $\nu_3$ in which they evolve in time and propagate in space. The flavor eigenstates can be written as a linear combination of the mass eigenstates:

$$|\nu_\alpha(t)\rangle = \sum_{n=1}^{N} U_{\alpha i} \, |\nu_i(t)\rangle \tag{1.1}$$

where $\alpha$ is the flavor of the neutrino ($e$, $\mu$ or $\tau$) and $N$ is the number of the considered neutrino families. This flavor mixing is regulated by an $N \times N$ matrix. In the $N = 3$ case this matrix is called PMNS (Pontecorvo-Maki-Nakagawa-Sakata) matrix and it contains

6 parameters: 3 angles ($\theta_{12}$, $\theta_{13}$, $\theta_{23}$), 1 Dirac phase ($\delta_{CP}$) and 2 Majorana phases ($\eta_1$, $\eta_2$).

$$\begin{aligned}\begin{pmatrix}\nu_e\\ \nu_\mu\\ \nu_\tau\end{pmatrix} &= U^{PMNS}\cdot\begin{pmatrix}\nu_1\\ \nu_2\\ \nu_3\end{pmatrix}\\ &= \begin{pmatrix}U_{e1} & U_{e2} & U_{e3}\\ U_{\mu1} & U_{\mu2} & U_{\mu3}\\ U_{\tau1} & U_{\tau2} & U_{\tau3}\end{pmatrix}\cdot\begin{pmatrix}\nu_1\\ \nu_2\\ \nu_3\end{pmatrix}\end{aligned} \tag{1.2}$$

$$\mathrm{U}^{PMNS} = \begin{pmatrix}1 & 0 & 0\\ 0 & c_{23} & s_{23}\\ 0 & -s_{23} & c_{23}\end{pmatrix}\begin{pmatrix}c_{13} & 0 & s_{13}e^{-i\delta_{CP}}\\ 0 & 1 & 0\\ -s_{13}e^{i\delta_{CP}} & 0 & c_{13}\end{pmatrix}\begin{pmatrix}c_{12} & s_{12} & 0\\ -s_{12} & c_{12} & 0\\ 0 & 0 & 1\end{pmatrix}\begin{pmatrix}e^{i\eta_1} & 0 & 0\\ 0 & e^{i\eta_2} & 0\\ 0 & 0 & 1\end{pmatrix} \tag{1.3}$$

where $c_{ij} = cos\,\theta_{ij}$ and $s_{ij} = sin\,\theta_{ij}$[1]. The value of these parameters cannot be determined theoretically, thus the experimental research is crucial for a better understanding of the flavor mixing and CP violation in the leptonic sector. In particular the two Majorana phases can only exist if the neutrinos are Majorana particles, that is a massive particle which states are described by the same field as the one describing the states of its antiparticle, the antineutrino in this case. An experimental evidence of such property would be the long-awaited confirmation of the almost secular Majorana theory.
This mismatch between the flavor and mass eigenstates has a remarkable consequence. When a neutrino of flavor $\alpha$ is produced in an interaction, it is produced in its flavor eigenstate $|\nu_\alpha(t=0)\rangle$. This flavor eigenstate can therefore be written as a composition of the mass eigenstates using determinate coefficient values given by the PMNS matrix. As mentioned in *Equation 1.1*, during its propagation the neutrino evolves in time in the mass basis. This means that each mass component of the original flavor eigenstate evolves on its own, resulting in the variation of the mass composition of the neutrino state.
The crucial point is the fact that when the neutrino interacts again, the probability of it interacting again as a $\nu_\alpha$ is not 1. Given that the probability to detect a neutrino of flavor $\beta$ starting from an initially $\alpha$-flavored neutrino is

$$\begin{aligned}P_{\alpha\beta}(t) &= P(\nu_\alpha \to \nu_\beta)(t)\\ &= |\langle\nu_\beta|\nu_\alpha(t)\rangle|^2\end{aligned} \tag{1.4}$$

[1] $\theta_{ij} \in [0, \pi/2]$, $\eta_i \in [0, 2\pi]$.

the probability to re-obtain $\nu_\alpha$ in the measurement is given by

$$\begin{aligned} P_{\alpha\alpha}(t) &= P(\nu_\alpha \to \nu_\alpha)(t) \\ &= |\langle \nu_\alpha(t=0)|\nu_\alpha(t)\rangle|^2 \\ &= |\sum_{i=1}^{N}\sum_{j=1}^{N} U^*_{\alpha j}U_{\alpha i}\,\langle \nu_j(t=0)|\nu_i(t)\rangle| \end{aligned} \tag{1.5}$$

which tends to 1 for $t \to 0$, but in general $P_{\alpha\alpha}(t) \neq 1$. On the other hand, the probability to detect as $\nu_\beta$ an originally $\nu_\alpha$ neutrino is non-zero. This means that neutrinos propagating for a certain distance have a certain probability to interact as a neutrino of a different flavor from the original one. This non-conservation of the weak flavor during the propagation of the particle is called Neutrino Oscillation.
In the 3-flavor case, the quantity given by the *Equation 1.4*, called oscillation probability[2], turns out to be

$$\begin{aligned} P_{\alpha\beta}(t) &= |\sum_{i=1}^{N}\sum_{j=1}^{N} U^*_{\beta j}U_{\alpha i}\,\langle \nu_j(t=0)|\nu_i(t)\rangle| \\ &= \delta_{\alpha\beta} - 4\sum_{i<j}^{n} Re[U^*_{\alpha i}U_{\beta i}U_{\alpha j}U^*_{\beta j}]sin^2\,\frac{(m_i^2-m_j^2)L}{4E} + \\ &\quad + 2\sum_{i<j}^{n} Im[U^*_{\alpha i}U_{\beta i}U_{\alpha j}U^*_{\beta j}]sin\,2\frac{(m_i^2-m_j^2)L}{4E} \end{aligned} \tag{1.6}$$

Notice the presence of mass terms in the sine arguments. This means that the neutrino oscillation probability would be null if neutrinos were massless particles, implying that neutrino oscillations only occur if neutrinos are massive particles having a different mass for each.
Unfortunately neutrino oscillations are only sensitive to the difference of the square of the masses $m_i^2 - m_j^2 \equiv \Delta m^2_{ij}$[3] between neutrinos, so only bounds have been determined so far regarding the absolute mass values.
It must be also underlined that neutrino oscillations are not sensitive to the Majorana phases since they cancel out in *Equation 1.6*. Since the amplitudes of the processes involving them are suppressed by a generally small factor $m_\nu/E_{process}$, these two parameters would only be observable through few particular processes, namely the neutrino-less double $\beta$ decay.
Regarding the other sensitive oscillation parameters and the $\Delta m^2_{ij}$ values, their estimate has been measured and improved in the last 25 years thanks to the contribution of many experiments. Since it has been observed and confirmed that all of the angles $\theta_{ij}$ have a

[2]On the other hand, the quantity calculated using the same flavor as in *Equation 1.5* is called survival probability.
[3]The parameters $\Delta m^2_{ij}$ are also often called $\Delta m^2_{ji}$ interchangeably.

non-zero value, projects now focus on the measurement of $\delta_{CP}$, which could potentially be non-zero but it is not well constrained yet, and on the mass values, which still have a lot of unclear issues.
In many cases, there is an evident dominance of a single $\Delta m^2_{ij}$ term contribution over the others, such as the observation of solar and atmospheric neutrinos (see *Section 1.5*). In such cases the expression in *Equation 1.6* can be further simplified in the 2-flavor limit: [1]

$$\begin{aligned} P_{\alpha\beta} = P(\nu_\alpha \to \nu_\beta) &= \delta_{\alpha\beta} - (2\delta_{\alpha\beta}1) sin^2 2\theta_{ij}\, sin^2\left(\frac{\Delta m^2_{ij} L}{4E}\right) \\ &= \delta_{\alpha\beta} - (2\delta_{\alpha\beta}1) sin^2 2\theta_{ij}\, sin^2\left(1.267\,\frac{\Delta m^2_{ij} L}{E}\left[\frac{eV^2 km}{GeV}\right]\right) \end{aligned} \tag{1.7}$$

| Parameter | Value |
|---|---|
| $sin^2(\theta_{12})$ | $0.307^{+0.013}_{-0.012}$ |
| $sin^2(\theta_{23})$ | $0.558^{+0.015}_{-0.021}$ (NO)<br>$0.553^{+0.016}_{-0.024}$ (IO) |
| $sin^2(\theta_{13})$ | $2.19^{+0.07}_{-0.07} \cdot 10^{-2}$ |
| $\Delta m^2_{12}$ | $7.53^{+0.18}_{-0.18} \cdot 10^{-5}\ eV^2$ |
| $\lvert\Delta m^2_{23}\rvert$ | $2.455^{+0.028}_{-0.028} \cdot 10^{-3}\ eV^2$ (NO)<br>$2.529^{+0.029}_{-0.029} \cdot 10^{-3}\ eV^2$ (IO) |
| $\delta_{CP}$ | $-0.81^{+0.22}_{-0.22} \cdot \pi\ rad$ |

Table 1.1: *Current estimates of the neutrino oscillation parameters in Normal and Inverted Ordering (see Section 1.3). [1]*

## 1.3 Mass ordering and mass measurement techniques

Thanks to the studies on neutrino oscillations it was possible to attain an experimental value for the mass splitting quantities $\Delta m^2_{12}$ and $|\Delta m^2_{23}|$. It must be underlined that the sign of the splitting $\Delta m^2_{23}$ is still unknown and $\Delta m^2_{12} \ll |\Delta m^2_{23}|$. This gives rise to to two possible neutrino mass spectrum ordering scenarios:

- Normal Ordering (NO), where $\Delta m^2_{23} > 0$ therefore $m_3 > m_2 > m_1$;
- Inverted Ordering (IO), where $\Delta m^2_{23} < 0$ therefore $m_2 > m_1 > m_3$;

However, being oscillations only sensitive to the square mass difference, they can't give much additional information than these constraints. Information regarding the mass scale

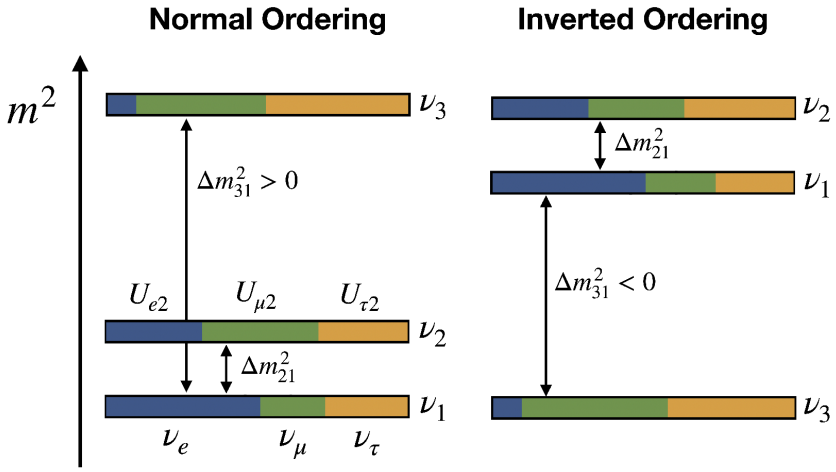


Figure 1.2: *Representation of the potential neutrino mass hierarchies. Each mass state is a linear combination of the flavor eigenstates.*

of neutrinos must be found exploiting other types of experiments.
The kinematic approach is based on the idea that the mass of the neutrino affects the distribution of the electron energy in a nuclear $\beta$ decay. It defines a Kurie function $K(E_e)$ which depends linearly on the electron energy if $m_\nu = 0$. In the case $m_\nu \neq 0$ this linearity is lost, and it manifests as a deformation around the endpoint in the Kurie plot, which is the Kurie function versus the $\beta$-electron energy plot. The most recent result coming from experiments that follow this path is from KATRIN using tritium decay. No indication of $m_\nu \neq 0$ has been found yet, but it set an upper limit on the effective mass of the electronic neutrino, $m_{\nu e}^{eff} < 0.8eV$ at 90% CL.

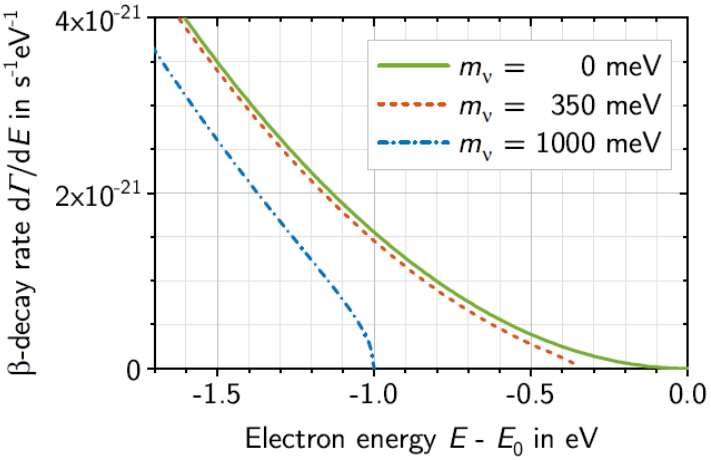


Figure 1.3: *Theoretical differential $\beta$-electron energy spectrum near the endpoint for the decay of molecular tritium showing the dependence of the spectrum on the neutrino mass. [4]*

The alternative available approach is the study of the neutrino-less double $\beta$ decay. On top of verifying the Majorana nature of neutrinos, this process is also sensitive to the effective mass of $\nu_e$. Precisely, the observable exploited by the experiments, which is the decay

half-life of the process $T_{1/2}^{0\nu\beta\beta}$, depends on the inverse square of such mass $(T_{1/2}^{0\nu\beta\beta})^{-1} \propto m_{ee}$. The drawback of this method is the dependence of $m_{ee}$ on the unknown Majorana phases $\eta_i$, which introduces further uncertainties in the process and constrains less the variable, allowing a broader range of $m_{ee}$ values compared to the $m_{\nu e}$ in the kinematic approach. The current strongest bounds on this front are given by KamLAND-Zen and GERDA, which respectively imply an upper bound effective mass of $m_{ee} < 28 - 122\ meV$ and $m_{ee} < 79 - 180\ meV$. [1, 4, 5, 6]

## 1.4 *CP* violation and matter-antimatter asymmetry

The $C$ or Charge conjugation symmetry is said to to be conserved when the application of such $C$ operation, which is the replacement of every particle with its respective antiparticle, does not affect the physical validity of an interaction. Similarly, $P$ or parity symmetry is conserved if the interaction is valid after the inversion of spatial coordinates and momenta. The simultaneous application of these two operations is referred to as the $CP$ symmetry. While these symmetries are respected by both the electromagnetic and strong interaction, $C$ and $P$ are both maximally violated by the weak interaction. It was originally thought that $CP$ instead is always conserved meaning that particles and antiparticles would obey the same laws of nature.
However in 1964 it was discovered that weak interaction also can violate the $CP$ symmetry in certain processes involving the quark sector such as the neutral Kaon decay [7]. Such asymmetry was also observed in B-meson decays in 2001 [8, 9] and D-meson decays in 2019 [10]. Since lepton flavor mixing parameters and neutrino mass splittings were defined, the $CP$ violation is expected to be violated in the leptonic sector too. This is also encouraged by the fact that $CP$ violation is one of the three essential Sakharov conditions for the genesis of the present matter-only universe. Furthermore, the amount of this asymmetry seems to be too large to be explained considering only the $CP$ violation in Kaons and B-mesons.
The $CP$ violation in the leptonic sector can be determined by studying the Dirac phase of the PMNS matrix $\delta_{CP}$. Experiments can measure the value of this parameter by means of an asymmetry quantity $A_{CP}^{\alpha\beta}$ defined as: [1, 11]

$$\begin{aligned} A_{CP}^{\alpha\beta} &= P(\nu_\alpha \to \nu_\beta) - P(\bar{\nu}_\alpha \to \bar{\nu}_\beta) \\ &= 4 \sum_{i<j}^{n} Im[U_{\alpha i} U_{\beta i}^* U_{\alpha j}^* U_{\beta j}] \, sin\, 2X_{ij} \end{aligned} \tag{1.8}$$

## 1.5 Experimental study on neutrino oscillations

The experimental study of neutrino oscillations in practice consists in the measurement of the flux of the studied neutrino flavors and compare the obtained results with the predicted oscillation or survival probability depending on the considered transition. In the first case the experiment is said to work in appearance mode, in the latter in disappearance mode. As it can be deduced by the oscillation probability in *Equation 1.6* and *Equation 1.7*, there are two parameters over which it is possible to design an experiment: the oscillation length $L$ and the neutrino energy $E$, whose choice is fundamental to maximize the oscillation effects. In fact, the oscillation effects are the most visible when the argument of the sine function is of order 1, that is

$$\frac{\Delta m^2_{ij} L}{4E} \sim 1 \tag{1.9}$$

Once fixed the $\Delta m^2_{ij}$ range of interest, $L$ and $E$ have to be chosen accordingly. The requirement for an experimental study of the effects of neutrino oscillations is the knowledge of the flux and flavor components of the neutrinos close to the the source and at the distance $L$ from the source where neutrinos could potentially have changed flavor. In general, neutrinos seen by a detector could come from various sources at different energy scales ranging over several orders of magnitude. Therefore neutrinos can mostly be categorized depending on their origin:

- Solar Neutrinos, electron neutrinos ($\nu_e$) produced in the thermonuclear reactions occurring in the sun; they typically have energies of few $MeV$s, and they historically contributed to better understand the Standard Solar Model and to the experimental observation of the MSW effect[4];
- Atmospheric Neutrinos, neutrinos produced in the decays of pions and kaons generated by the interaction of the cosmic rays with the earth's atmosphere; they contain all flavors of neutrinos and antineutrinos and have a broad range of energy spreading from tenths of $GeV$ to few $TeV$s; they are also the neutrinos that led to the discovery of neutrino oscillations in 1998;
- Accelerator Neutrinos, neutrinos produced in the decays of pions and kaons generated by the interaction of a proton beam colliding on a target; they mostly consist of muon neutrinos ($\nu_\mu$) right after production, and they have the advantage that they are the most manageable type of neutrino, in terms of energy (typically few $GeV$) and flux (for instance they can be produced in short pulses and the detector can receive beam data at source such as timings);

[4]Often referred to also as "matter effect", it consists in the variation of the flavor composition of the mass eigenstates of neutrinos propagating in a dense medium with varying density. It has to be taken into account when neutrinos propagate in matter for long distances, for instance when escaping the sun or when crossing the earth.

- Reactor Neutrinos, electron antineutrinos ($\bar{\nu}_e$) produced in large quantities at energies of few $MeV$ in the nuclear fission of heavy isotopes in a nuclear reactor;
- Astrophysical Neutrinos, neutrinos having astronomical origins that have a very wide energy spectrum ranging from the $MeV$ to the $EeV$ scale; to this day this is the only source of information for neutrinos at few hundreds of $TeV$ to energies in the $PeV$ scale and above; neutrinos coming from supernova bursts belong to this category.

The recent experiments focused on neutrino oscillations generally exploit accelerator or reactor neutrinos since they provide a large flux of neutrinos having a narrow energy spectrum. In particular accelerator neutrino experiments are the only source of neutrinos that can be controlled and they can be designed to work at the desired energy, while reactor neutrino experiments can exploit the by-products of electric energy production, supplied in large quantity by already existing structures. Moreover, these two types of experiments can be built having the desired $L$ value, called baseline, to maximize the oscillation effects. The detector right next to the source is usually referred as the Near Detector, while the one built at a distance $L$ from it is called Far Detector. When the baseline is of the order of a few hundred meters to few kilometers, the experiment is called to be a Short-Baseline oscillation experiment (SBL) and it focuses to relatively large mass splitting dominant oscillations. If the baseline is much longer, reaching few hundreds to few thousand $km$, the experiment is said to be a Long-Baseline oscillation experiment (LBL), and it generally focuses more on oscillations having the effects given by smaller mass splitting values. [1]

| Source | | $L$ $(m)$ | $E$ $(MeV)$ | $\lvert\Delta m^2\rvert$ $(eV^2)$ |
|---|---|---|---|---|
| Solar | | $10^{10}$ | 1 | $10^{-10}$ |
| Atmospheric | | $10^4 - 10^7$ | $10^2 - 10^5$ | $10^{-1} - 10^{-4}$ |
| Reactor | SBL | $10^2 - 10^3$ | 1 | $10^{-2} - 10^{-3}$ |
| | LBL | $10^4 - 10^5$ | | $10^{-4} - 10^{-5}$ |
| Accelerator | SBL | $10^2$ | $10^3 - 10^4$ | $> 0.1$ |
| | LBL | $10^5 - 10^6$ | $10^3 - 10^4$ | $10^{-2} - 10^{-3}$ |

Table 1.2: *Characteristic values of the quantities in the oscillation probability for experiments using neutrinos from various sources. Astrophysical neutrinos are not constrained to a limited range since both L and E can assume very different values and they would feel the effects of most mass splitting values. [1]*

### Hyper-Kamiokande (HK, Hyper-K)

Hyper-Kamiokande is a large-scale water Cherenkov neutrino detector that will be the follow-up of Super-Kamiokande, the experiment that in 1998 discovered neutrino oscil-

lations through the observation of atmospheric neutrinos. Its working principle is based on the detection of the Cherenkov rings generated by the products of the interaction occurring in the detector by means of photomultipliers covering the internal surface of the 260 $kt$ water tank. It will be able to detect incoming solar, atmospheric and supernova burst neutrinos, but also accelerator neutrinos coming from the J-PARC accelerator 295 $km$ away, working as an upgrade of the T2K experiment that has been using Super-Kamiokande as far detector. Its main focus is the measurement of the CP violation phase, but it has a rich physics program that includes the precision measurement of the PMNS matrix parameters, the search of the nucleon decay and the observation of supernova burst neutrinos. The experiment is planned to start its operation in 2027. [12]

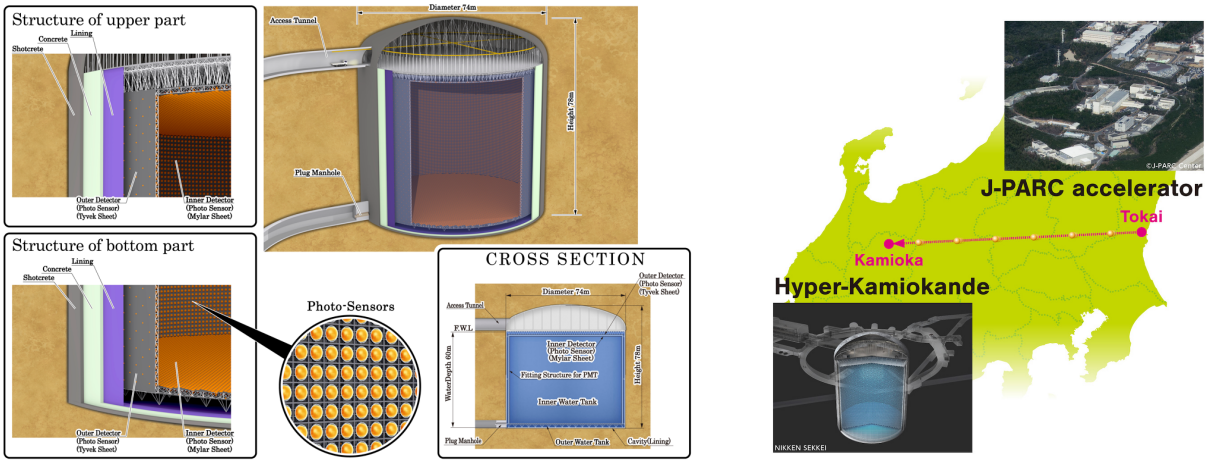


(a) (b)

Figure 1.4: *Schematic view of the Hyper-Kamiokande detector (1.4a) and its position relative to the accelerator (1.4b).*

### Deep Underground Neutrino Experiment (DUNE)

DUNE is a liquid argon neutrino oscillation experiment under construction in the US. It mainly consists of two liquid Argon Time Projection Chambers (LAr-TPC) containing 17.5 $kt$ of liquid argon each. These detectors will act as the far detector of the experiment, 1300 $km$ apart from the beam source at Fermilab providing accelerator neutrinos. Additionally, it also plans to detect and study solar, atmospheric and supernova neutrinos. A phase II upgrade of the detector is planned at a later stage, increasing the number of detectors from 2 to 4, powering up the beam power and upgrading the near detector.
DUNE has a program that is similar to Hyper-Kamiokande's one, however thanks to the different target and baseline the two experiments can attain complementary measurements. In particular, Hyper-K will have a better sensitivity to the CP violation, while DUNE will have a better sensitivity on the mass hierarchy because of its longer baseline therefore larger impact of the matter effect. The experiment aims to start the scientific exploitation in 2029. [13]

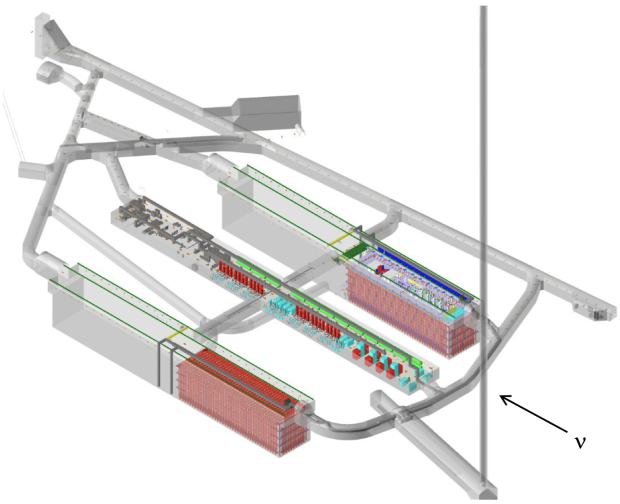


(a)

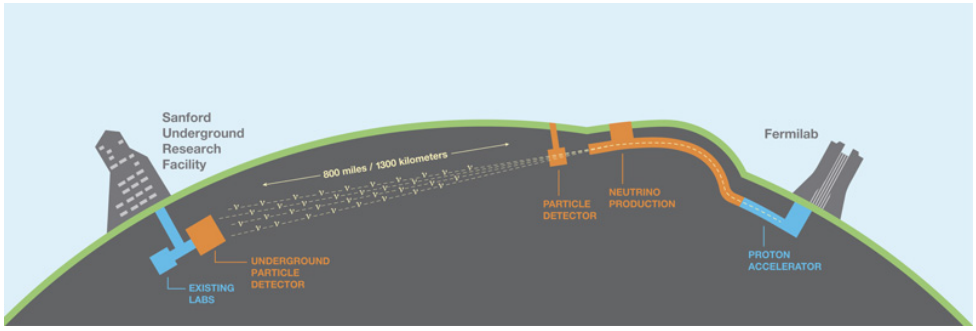


(b)

Figure 1.5: *Schematic view of the DUNE far detector (1.5a) and of the whole experiment (1.5b).*

### Jiangmen Underground Neutrino Observatory (JUNO)

JUNO is a large liquid scintillator detector that aims to determine the neutrino mass ordering by observing reactor neutrinos coming from 2 nuclear power plants located at 52.5 $km$ from the detector. It contains 20 $kt$ of liquid scintillator that emit photons when an event occurs, and these photons are collected by photomultipliers mounted on the structure that forms the central detector. While the experiment focuses on the determination of the mass ordering and on the precision measurement of the oscillation parameters, the multi-purpose detector studies multiple topics similarly to the other two experiments, such as the supernova neutrinos and the proton decay. The experiment is expected to finish its construction in 2025. [14]

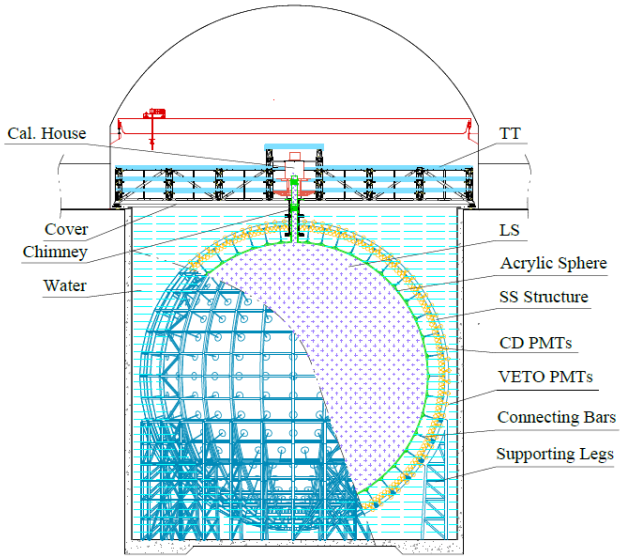


(a)


(b)

Figure 1.6: *Schematic view of the JUNO detector (1.6a) and its position relative to the reactors (1.6b).*

# Chapter 2

# The T2K Experiment and Time Projection Chambers

This chapter will give an overview of the fundamentals of the T2K experiment and Time Projection Chambers (TPC), as these topic are crucial to get the big picture and understand where this study originated from.

## 2.1 T2K

T2K is a long-baseline neutrino oscillation experiment located in Japan that has been running and collecting data since 2010. Its original major purposes were:

- The search of $\nu_\mu \rightarrow \nu_e$ oscillation and measurement of the $\theta_{13}$ parameter which was unknown at the time;
- The precise measurement of the parameters involved in the $\nu_\mu \rightarrow \nu_\mu$ disappearance mode, namely $\theta_{23}$ and $\Delta m^2_{23}$.

At a later stage, thanks to the confirmation of a non-zero $\theta_{13}$ value and of the involvement of all three neutrino mass eigenstates in the oscillation phenomenon, a new additional objective was added:

- The delimitation of the values of the $CP$ violation phase $\delta_{CP}$ to confirm whether the $CP$ symmetry is conserved in the leptonic sector or not.

A long-baseline neutrino oscillation experiment studies neutrino oscillations by comparing the properties of the neutrino flux between a location right next to the source and a location which can be hundreds if not thousands of kilometers far away. The measured data includes information such as flux, energy and flavor components of the generated neutrinos, and it is collected by at least two detectors located at a different distance from the source of the experiment, which could be an accelerator or a nuclear reactor. The

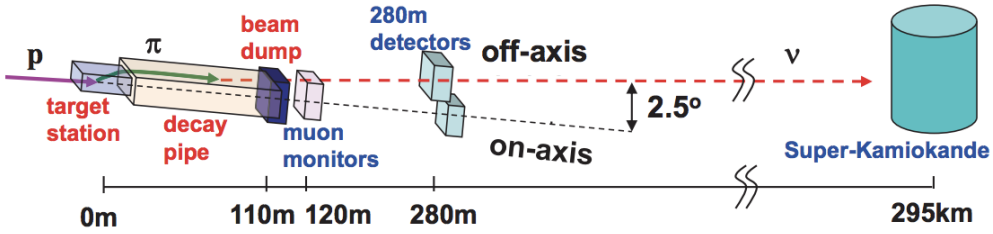


Figure 2.1: *Diagram of the T2K experiment showing the relative position of each detector.*

closer one is usually called near detector and it monitors the properties of the neutrino flux right next to the source reducing the systematic errors that enter the measurements, while the farther one, usually referred to as far detector, is located at a distance where oscillation effects become visible and it has the task of checking how these properties did change during the propagation along the baseline.

The source of the neutrino beam of T2K is the 30 $GeV$ proton accelerator of the J-PARC accelerator facility situated in the Ibaraki prefecture. After bending their trajectory towards the direction of the detectors, the accelerated protons are shot on a graphite target and produce mesons in the interaction that decay into neutrinos while propagating in a decay tunnel. After production, the beam first reaches the near detector complex situated at 280 $m$ downstream of the collision point. The near detector complex consists of several detectors: INGRID, which monitors the intensity and the direction of the incoming beam, ND280, which measures flux, energy spectrum and flavor composition of the beam, and WAGASCI-BabyMIND, which studies the cross section of neutrinos on water and scintillators. The beam then propagates further moving beneath the surface of the earth for 295 $km$ before reaching the Super-Kamiokande far detector, a large water cherenkov detector situated in the Kamioka mines in the Gifu prefecture[5].

It is important to mention that not all of the detectors are located directly on the beam axis, but some of them were built in positions having an off-axis angle with respect to the beam axis going up to 2.5°. The advantage of placing a detector off-axis is the fact that the energy distribution of the neutrino beam is narrower compared to the on-axis spectrum. This means that the spread of the measured energy spectrum is smaller and that there are less background events coming from unwanted high-energy components of the beam. Additionally, the peak value of the energy distribution gradually decreases as the off-axis angle increases implying that the position of the detector can be adjusted in such a way that it is reached by a neutrino flux having a smaller energy spread around a desired peak value. [15, 16]

[5]The letters of the name of the experiment stand for "Tokai to Kamioka".

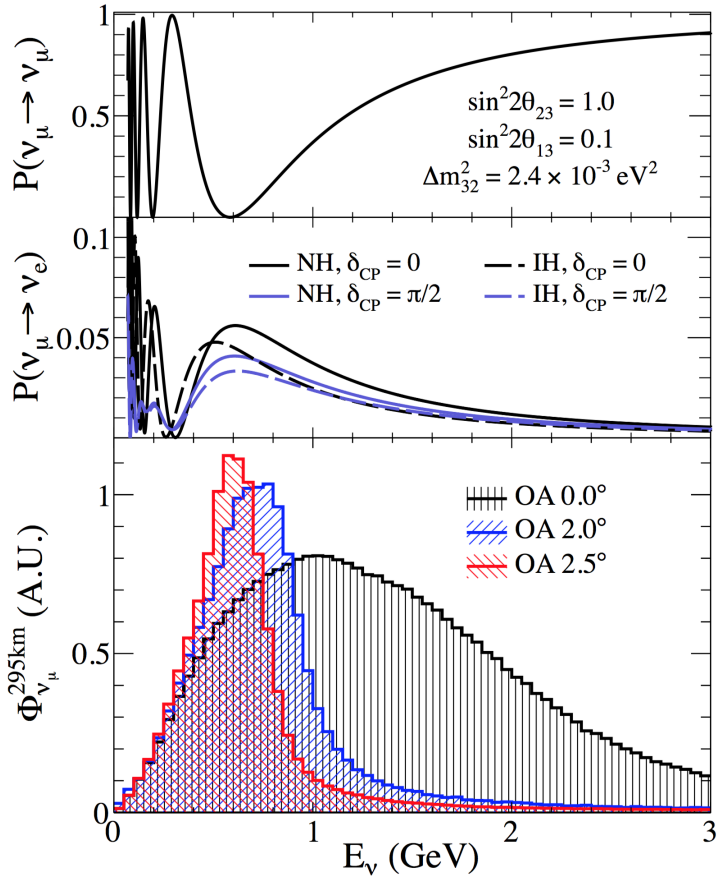


Figure 2.2: *Plot showing the disappearance probability of a $\nu_\mu$, the appearance probability of a $\nu_e$ and the flux of $\nu_\mu$ depending on the neutrino energy at a fixed oscillation distance of 295 km. [11]*

### 2.1.1 Accelerator and Neutrino Beamline

The J-PARC accelerator increases the energy of the protons in three gradual steps. The last acceleration step is carried out in the Main Ring, which can bring their energy up to 30 GeV. These protons are then injected into the Neutrino Beamline, which is made of a Primary Beamline and a Secondary Beamline. In the Primary Beamline the beam is focused and bent to face towards Kamioka combining the use of normal conducting and superconductive magnets. The Second Beamline can be split in three sections: target station, decay volume and beam dump. The target station hosts a graphite target and three magnetic horns. The target is preceded by a baffle that protects the horns and an optical transition radiation monitor that checks the profile of the incoming proton beam. These protons hit the graphite target and produce a large number of mesons in the interaction, namely pions and kaons. The three magnetic horns have the task of collecting such interaction products, filter unnecessary particles and focus the beam towards the detectors, especially its pion component. Additionally, these horns define the operation mode of the experiment, as they can toggle it between neutrino and antineutrino

| Particle | Decay Channel | Branching Ratio |
|---|---|---|
| $\pi^{\pm}$ | $\pi^+ \to \mu^+\nu_\mu$ | 99.9877 % |
| | $\pi^+ \to e^+\nu_e$ | $1.23 \cdot 10^{-4}$ % |
| $K^{\pm}$ | $K^+ \to \mu^+\nu_\mu$ | 63.56 % |
| | $K^+ \to \pi^0 e^+\nu_e$ | 5.07 % |
| | $K^+ \to \pi^0\mu^+\nu_\mu$ | 3.352 % |
| | $K^+ \to e^+\nu_e$ | $1.582 \cdot 10^{-5}$ % |
| $K^0_L$ | $K^0_L \to \pi^- e^+\nu_e$ | 40.55 % |
| | $K^0_L \to \pi^-\mu^+\nu_\mu$ | 27.04 % |
| | $K^0_L \to \pi^+\pi^-\pi^0$ | 12.54 % |
| $\mu^{\pm}$ | $\mu^+ \to e^+\bar{\nu}_\mu\nu_e$ | 100 % |

Table 2.1: *List of the main neutrino-producing decay channels of the particles generated in the collision between the proton beam and the graphite target and their branching ratios [1]. The charge conjugated modes of the charged particles are valid as well with the same values of branching ratio.*

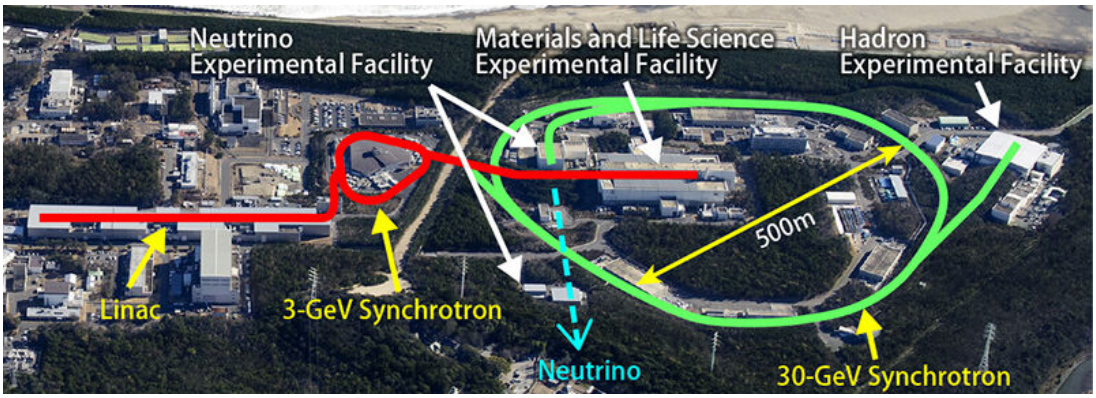


Figure 2.3: *Scheme showing the acceleration stages of the J-PARC accelerator.*

mode by inverting the direction of the current flowing inside of them. This functionality is very important in the study of $CP$ violation effects, since it makes it possible to study both neutrino and antineutrino data and compare the two. The following decay volume is a $\sim$96 $m$ long steel tunnel where the interaction products gradually decay into neutrinos. A beam dump is located at the end of the tunnel to stop all the non-relevant components of the beam, namely hadrons and low energy muons. Muons having an energy above 5 $GeV$ that make it through the dump are detected by the muon monitor (MUMON) that follows right after and their direction is used to monitor the direction of the outgoing beam.

The resulting neutrino beam has an energy distribution peaking around 1 $GeV$ on-axis which, considering the off-axis geometry of the detector, is optimal for the observation of

$\nu_\mu \rightarrow \nu_e$ oscillation effects. Indeed, the beam specifics were chosen purposely to maximize the sensitivity to oscillation effects for the baseline length of the experiment: since the baseline is equal to $L = 295\ km$ and it was known that $|\Delta m^2_{23}| = 2 \cdot 10^{-3}\ eV$ thanks to previous experiments like Super-Kamiokande, K2K and MINOS, it is possible to estimate the optimal energy of the beam using *Equation 1.9*. It turns out that $E \sim 600\ MeV$, which is indeed the position of the peak of the energy distribution of the beam at 2.5° off-axis angle.
The beam power of the experiment has been gradually increasing since the beginning of the experiment to increase the statistics of collected data, reaching 515 $kW$ in 2020. The beam is currently undergoing an upgrade aiming to reach a goal of 1.3 $MW$ by 2027, the year when Hyper-Kamiokande is planned to start collecting data. Such upgrade is not achieved by an increase of the proton energy, but rather by an increase of the number of beam spills and of the number of protons in each spill. [15, 17, 18]

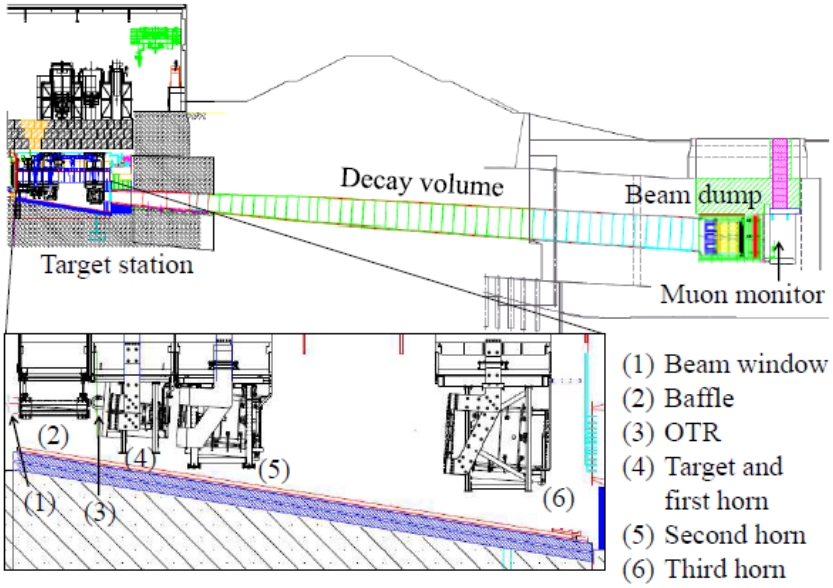


Figure 2.4: *Diagram of the beamline surrounding the collision point.*

### 2.1.2 Near Detector Complex

The near detector complex hosts three different detectors 280 $m$ downstream of the primary target: INGRID, ND280 and WAGASCI-BabyMIND. They all have the common goal of characterizing the beam, predict the interactions in the far detector and reduce the systematic errors in the analysis.

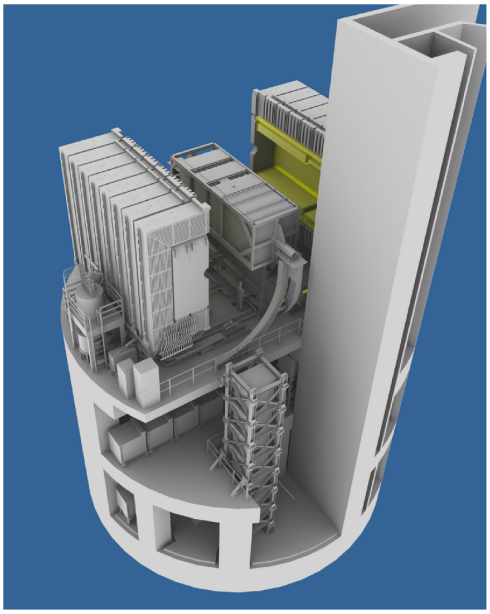

Figure 2.5: *Model of the near detector complex with INGRID and ND280.*

### INGRID

INGRID (Interactive Neutrino GRID) is an on-axis detector which measures directly the intensity and the direction of the neutrino beam by means of $\nu$ interactions. It is made of 16 modules made of 9 iron plates and 11 scintillator layers placed alternately in a sandwich structure surrounded on the sides by veto scintillator planes. 7 of these modules are placed along the vertical axis on a plane that is transverse to the direction of the beam, while other 7 are placed along the horizontal axis on a parallel plane. The remaining 2 modules are located off-axis to check the axial symmetry of the beam. In addition to these 16 modules there is an extra Proton module made purely of scintillator planes and surrounded by veto planes placed on-axis between the two central modules of the two planes. It has the task of detecting muons and protons produced in an INGRID module and study the quasi-elastic interaction channels comparing the data with Monte Carlo simulations.
Checking the stability of the beam direction is fundamental for the sakes of the experiment, since a variation of 1 $mrad$ of the beam direction results in a shift of 25 $MeV$ of the peak of the neutrino energy spectrum, and this is a large number for an experiment trying to achieve a precise measurement of the order of $\delta(\Delta m^2_{23}) \sim 10^{-4}\ eV$. INGRID carries out the job together with MUMON upstream, measuring the direction of the beam with a precision better than 0.4 $mrad$. [15, 19, 20]

### ND280

The ND280 near detector is an off-axis detector that has the task of measuring the specifics of the beam such as flux, energy distribution and flavor content in the direction of the far

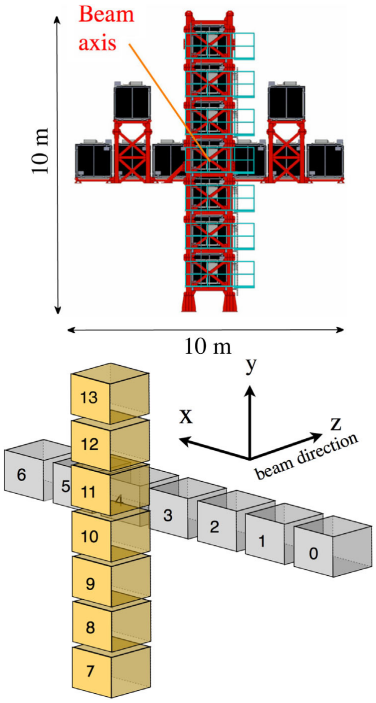


Figure 2.6: *Layout scheme of the INGRID modules.*

Figure 2.7: *Models of an INGRID module (top) and a proton module (bottom).*

detector, 2.5° off the beam axis.
In order to understand the design of the near detector it is crucial to understand the requirements imposed by the experiment. The three main goals of ND280 are:

- Provide information to determine the flux of $\nu_\mu$ at the far detector;
- Measure the $\nu_e$ content of the beam as a function of the energy of neutrinos;
- Study the interactions induced by $\nu_\mu$ to be able to predict the background interactions in the far detector in the search of $\nu_e$ appearance events.

In other words, ND280 has the task of measuring the flavor composition of the neutrino beam and characterizing the signal and background interaction channels of the far detector. To do so, the detector must be able to reconstruct the topology of exclusive events taking place inside of it and measure the rate of inclusive ones. Relevant events include:

- Charged-Current Quasi Elastic (CCQE) interactions

$$\begin{aligned} \nu_l + N &\rightarrow l^- + N' \\ \bar{\nu}_l + N &\rightarrow l^+ + N' \end{aligned} \tag{2.1}$$

- Charged-Current Non Quasi Elastic interactions

$$\begin{aligned} \nu_l + N &\rightarrow l^- + X \\ \bar{\nu}_l + N &\rightarrow l^+ + X \end{aligned} \tag{2.2}$$

- Neutral-Current single $\pi^0$ interactions

$$\begin{aligned} \nu_\mu + N &\rightarrow \nu_\mu + N + \pi^0 + X \\ \bar{\nu}_\mu + N &\rightarrow \bar{\nu}_\mu + N + \pi^0 + X \end{aligned} \tag{2.3}$$

- Neutral-Current Inelastic interactions

$$\begin{aligned} \nu_l + N &\rightarrow \nu_l + X \\ \bar{\nu}_l + N &\rightarrow \bar{\nu}_l + X \end{aligned} \tag{2.4}$$

ND280 consists of a central metal frame containing various detectors called "basket" surrounded by an electromagnetic calorimeter, a magnet formerly used in the UA1/NOMAD experiments and scintillators serving as muon detectors (Side Muon Range Detector, SMRD). The magnet generates a magnetic field of 0.2 $T$, which allows the measurement of the momenta of the charged particles in the detector.
The basket can be split in an upstream section and in a downstream one. The original

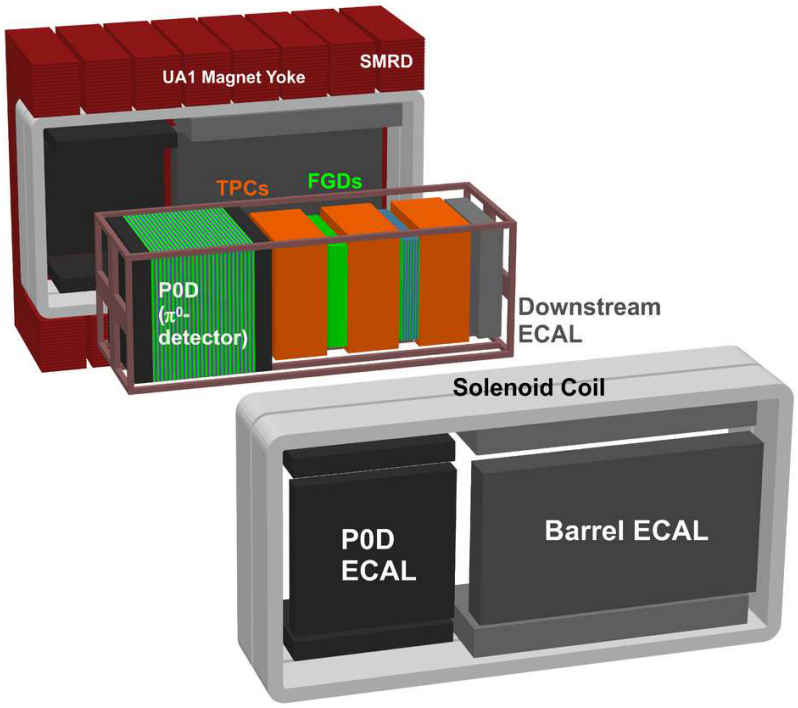


Figure 2.8: *Model of the original ND280 detector.*

design of ND280 contained the Pi-Zero Detector (P0D) in the upstream section, a detector optimized to study the $\pi^0$ producing NC process on water target. It consisted of tracking scintillator bar planes alternated to brass and lead foils, and it also contained passive layers which could be filled with water.
The downstream section on the other hand was optimized to measure the momenta of the incoming charged particles. It contained the tracker, made of three Time Projection Chambers (TPC) and two Fine Grained Detectors (FGD) alternating between each other. The TPCs focus on the measurement of the momenta and on the particle identification by means of charge and $dE/dx$ measurements, while the FGDs are scintillator bars acting as targets that focus on the topology of the events and the identification of the interaction type.
This design however had limitations concerning the efficiency of the reconstruction of events at angles above 50° with respect to the beam axis and the efficiency in selecting $\nu_e$ at energies below 1 $GeV$. These shortcomings were optimized in the ND280 upgrade in 2023-2024, which saw the replacement of the P0D with a new set of detectors in the upstream section. The SuperFGD is a set of approximately 2 million 1 $cm^3$ plastic scintillator cubes acting as an active target, that provides a more precise reconstruction of the event topology and a better identification of protons and pions at low energy. The SuperFGD is sandwiched on its top and bottom between two High-Angle TPCs (HA-TPC), which can reconstruct charged particles events (leptons in particular) at high angle values. These three detectors are finally surrounded by Time-Of-Flight detectors (TOF), scintillator bar planes read out by arrays of silicon photomultipliers that measure the timing of the incoming particles, reconstruct their direction of motion and veto the tracks coming from the surroundings of the detector. [15, 21, 22, 23]

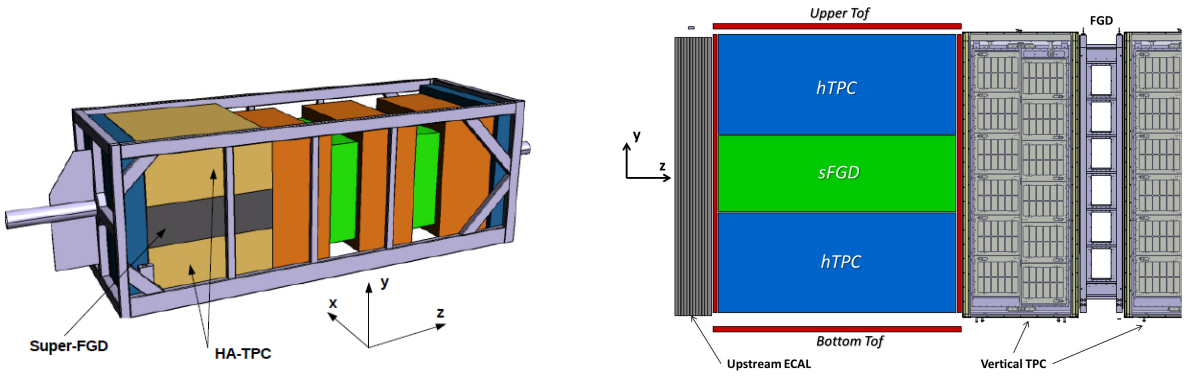


(a) (b)

Figure 2.9: *Scheme of the detector after the ND280 upgrade: view of the entire basket (2.9a) and detail of the upstream section including the TOF detectors (2.9b).*

### WAGASCI-BabyMIND

WAGASCI-BabyMIND (WAter Grid And SCIntillator, Baby Magnetized Iron Neutrino Detector) is a detector whose task is the study of neutrino interactions and their cross sections at energies around 1 $GeV$. It focuses particularly on the cross section of neutrino on water and scintillator targets, as their determination would lead to the reduction of a major systematic uncertainty of the experiment coming from the difference between the target material in ND280 and in Super-Kamiokande.
The detector consists of a segmented target of water and scintillator cells (WAGASCI) surrounded by a magnetic spectrometer (BabyMIND) that measures the momentum and identifies the charge of the outgoing particles. WAGASCI-BabyMIND is a relatively new addition to the near detector complex as it's been operational since 2019. It is positioned off-axis at an angle of 1.5°, which is smaller compared to the other off-axis detector, and as a consequence the energy of the neutrinos reaching the detector is slightly higher than ND280. [24, 25]

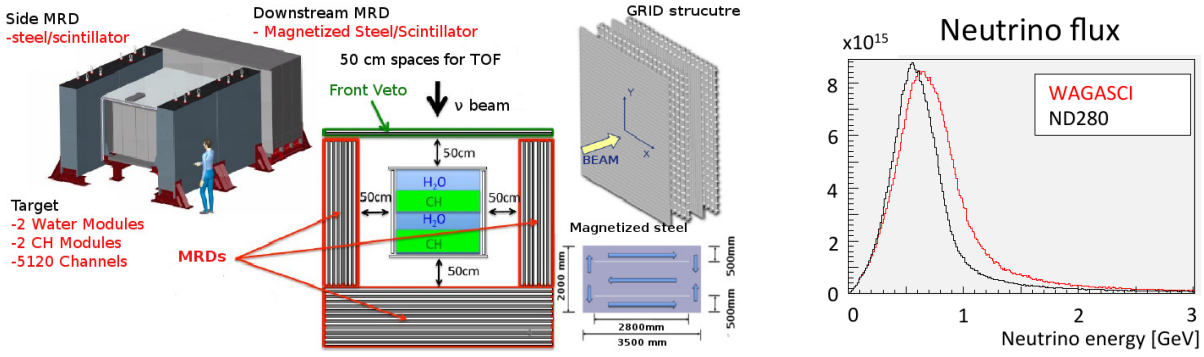


(a) (b)

Figure 2.10: *Scheme of the WAGASCI-BabyMIND detector (2.10a) and energy spectrum of the neutrino beam reaching it (2.10b).*

## 2.1.3 Far Detector

Super-Kamiokande is a large water cherenkov detector located 1000 $m$ (2700 $m$ water equivalent) deep under the surface of the earth in the Kamioka Mozumi mine. It's been operating independently since 1996 observing atmospheric and solar neutrinos and it made a large contribution in the discovery of neutrino oscillations. It's been serving as the far detector of T2K since 2010, adding accelerator neutrinos to its lineup.
The detector is located 2.5° off the axis of the neutrino beam as the ND280 detector. It is separated into two layers by a mechanical structure inside the detector: the Inner Detector and the Outer detector. The inner detector is the bulk of Super-Kamiokande

and it acts as both target and detector. Its internal surfaces are covered by approximately 11000 photomultipliers mounted on the mechanical support. The outer detector serves as shield and veto for incoming particles, and it is monitored by about 1900 photomultipliers. The detector globally contains 50 $kt$ of water, 32 $kt$ of which occupy the inner detector and 22.5 $kt$ of which is considered to be the fiducial mass of the detector.
The interaction events are detected by the photomultipliers through the cherenkov rings generated by the interaction products in water. The number and the sharpness of the rings makes possible the identification of the generated particles and the type of the occurring interaction. The signal channel of main interest is the CCQE scattering that produces a single ring, while the other interactions studied in ND280 are considered background events and may generate multiple rings.
The water cherenkov detector was originally filled with simple purified water, but a load of Gadolinium was added to the tank in 2020 and 2022. The addition was made because of the high neutron capture affinity of the gadolinium atoms, which emit a delayed X-ray photon when capturing a neutron coming from a $\bar{\nu}_l$ CCQE event. The identification of the X-ray signal led to a more precise reconstruction of the signal events inside the detector. Super-Kamiokande is planned to be replaced in 2027 by its successor Hyper-Kamiokande, at the same off-axis angle and distance from the primary target but 5 times larger than its predecessor. [15, 26, 27, 28, 29]

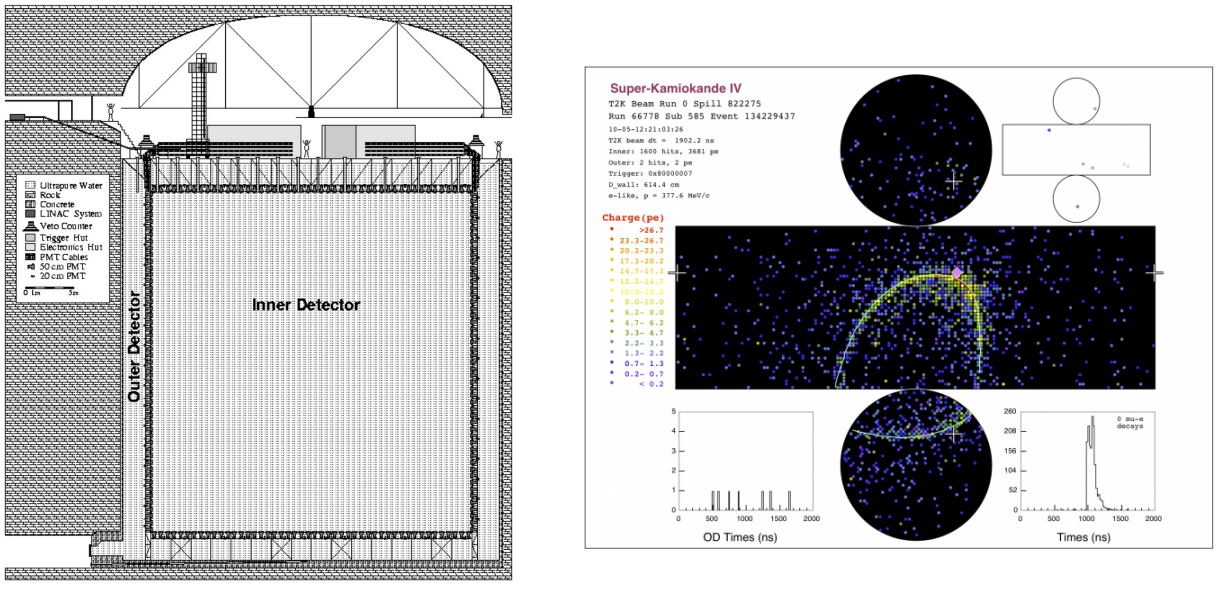


(a) (b)

Figure 2.11: *Scheme of Super-Kamiokande (2.11a) and picture displaying the cherenkov ring generated by an e-like event (2.11b).*

## 2.2 Time Projection Chambers

The Time Projection Chamber (TPC) is a gaseous detector proposed in 1976 by Nygren and Marx which is characterized by their large drift volume hosting an uniform electric field. It allows a three-dimensional reconstruction of the track of the charged particle crossing the detector with limited matter interference effects of the track.
The body of the detector is segmented by field shaping electrodes that are set to appropriate voltages and induce the formation of the uniform electric field inside of it. The body terminates at its end with a cathode plane and an anode readout endcap.
The working principle of the detector is no different from other gaseous detectors: an incoming charged particle ionizes the gas particles along its trajectory in the detector, generating electrons and ions which are drawn apart by an electric field covering the gas volume. Electrons and ions move towards the electrodes under the effect of this field and are eventually collected by them, inducing an electric signal which gives out the information of the event. What characterizes a TPC is its capability of reconstructing a track in the detector three-dimensionally exploiting the uniform electric field inside of it.
Two of the three dimensions of the tracks are reconstructed by the signal induced on the anode electrodes of the detector using a variety of technologies. Originally Multi-Wire Proportional Chambers (MWPC) were the most diffused readouts, but as the years passed Micro Pattern Gas Detectors (MPGD) also started to be an available option. The third dimension is reconstructed using the drift time of the electrons in the detector before reaching the electrodes. The drift time is measured as the difference between the arrival timing and an initial timing when the track crosses the detector, which is usually measured externally. Therefore the uniformity of the field and the knowledge of the drift velocity is crucial for a good reconstruction of the track and an efficient operation of the detector. A more detailed explanation on the behavior of charged particles inside a gas detector is given in *Chapter 3*.
The weakness of TPCs lay in their slowness. Electrons may take $\sim 10^{2-3}$ $\mu s$ to reach the electrode, while the ions have a much smaller mobility and it takes them even longer to be collected by the cathode. This also means that the detector does not tolerate high event rates, as charges pile up in the drift volume and space charge effects deform the electric field. [30, 31]

### 2.2.1 The T2K HA-TPCs

The High Angle Time Projection Chambers (HA-TPCs), implemented in ND280 with the upgrade of the T2K near detector, are two TPCs that have the task of reconstructing the tracks of charged interaction products having a high longitudinal angle with respect to the beam axis. Each TPC is $2.0 \times 0.8 \times 1.8$ $m^3$, and is split in two volumes that have 1 $m$ drift distance by a common central cathode set to approximately -27 $kV$. The volumes are filled

with a specific gas mixture called "T2K gas mixture" (Ar-$CF_4$-$iC_4H_{10}$) at few millibars above atmospheric pressure. The readout anodes consist of 8 Encapsulated Resistive Anode Micromegas (ERAM) per volume, and each module is 34×42 $cm^2$ large containing 32×36 1.1×1.0 $cm^2$ pads mounted on a module frame which serves as the endcap of the TPC. The whole detector is finally covered by a 0.2 $T$ magnetic field parallel to the drift direction in the TPCs, to allow particle identification in the detector by means of the curvature of the tracks. The HA-TPCs are able to reconstruct the tracks with a space resolution of the order of 500 $\mu m$, momentum resolution of $\sigma_p/p < 9\%$ and energy resolution of $\sigma_{dE/dx} < 10\%$. [22, 32]

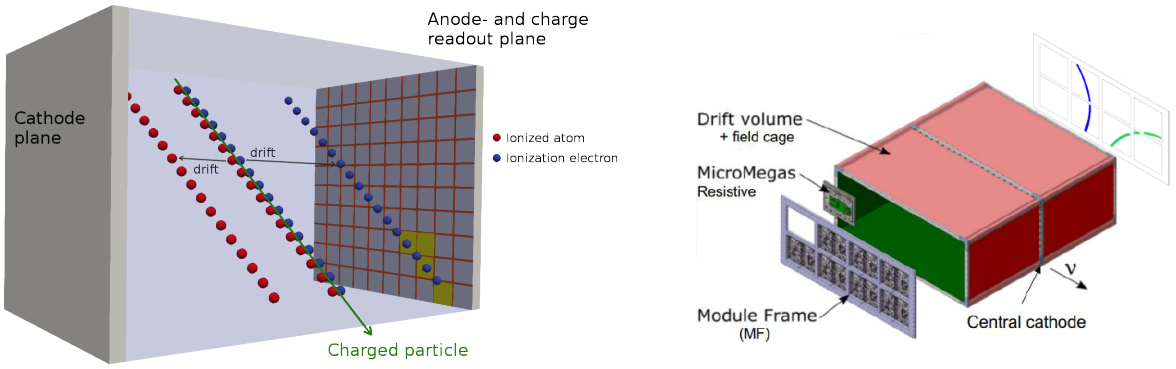


(a) (b)

Figure 2.12: *Working principle of a TPC (2.12a) and structure of the T2K HA-TPC (2.12b).*

# Chapter 3

# Micro Pattern Gaseous Detectors

Micro Pattern Gaseous Detectors (MPGD) are a group of gaseous ionization detectors that emerged at the end of the 1980s thanks to the advance of microelectronics and photolithographic technology on PCB. They are characterized by their fine structure ranging around tens to hundrends of micrometers, and they have better position and multi-track resolution, larger flux and rate capability and better mechanical stability compared to the classic wire chambers.
The working principle of the MPGDs is based on the multiplication along a short distance of the ionization electrons generated in the gas chamber, which makes possible an amplification of the electrical signal in a limited region of the detector, while minimizing its effects throughout the gas chamber. These detectors are largely used as amplification and readout components of TPC-like gaseous detectors in experiments all around the world, including the T2K experiment.

## 3.1 Charged particle behavior in a gaseous detector

The multiplication mechanism inside a gas of the electrons depends on several factors, such as the gas composition and its pressure, but the most fundamental quantity that determines the behavior of an electron is the intensity of the electric field it is subject to.

### 3.1.1 Drift

In the absence of electric fields, charged particles only follow an uniform diffusion motion. Applying an electric field adds to this motion a drift component, which follows the direction of the field the charged particle. Macroscopically in this situation the charged particle is subject to an electric force which is counterbalanced by a viscous friction, which is the result of the microscopic interaction of the drifting particle with the gas molecules

along its path. This makes it such that the drift motion of the charged particles can be represented by a constant speed called drift velocity, which is proportional to the intensity of the electric field and a quantity called mobility, which depends on the particle at hand ($v_{drift} = \mu E$). Ion mobility values are typically smaller by several orders of magnitude compared to electron mobility values, implying that ions are much slower than electrons and therefore it takes them much longer to reach the electrode inside a gas detector. [30]

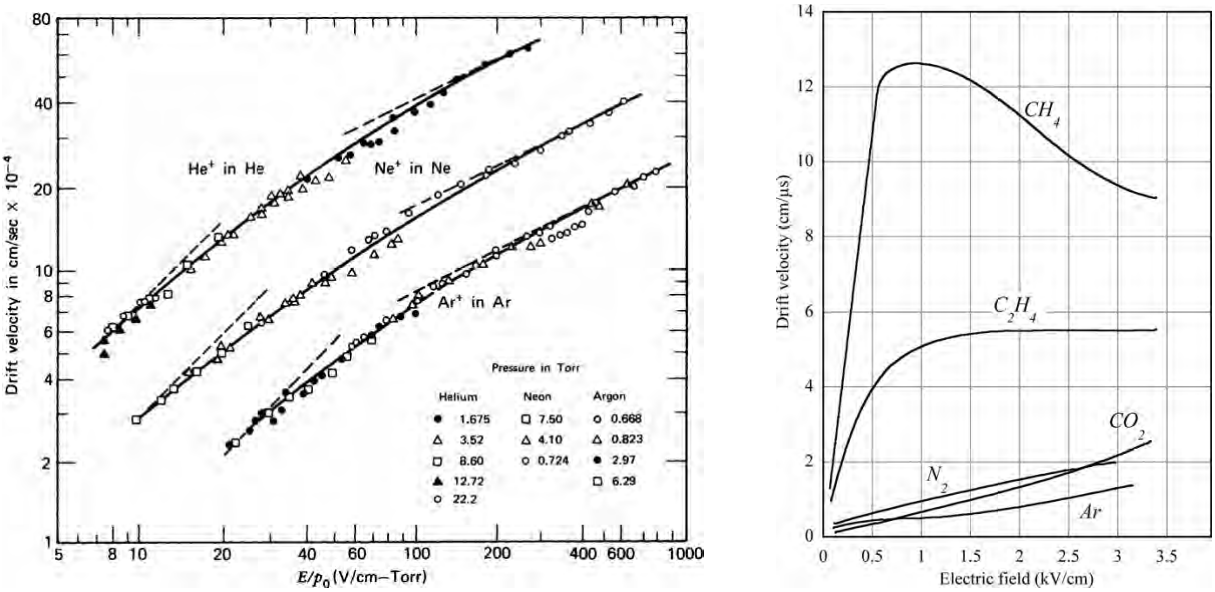


(a) (b)

Figure 3.1: *Plots of drift velocities of ions (3.1a) and of electrons at NTP (3.1b). These results show the distinct difference between the magnitude of the velocities thus the mobilities of ions and electrons. Namely, considering an Argon medium at NTP subject to a 1000 V/cm electric field, the ion drift velocity results to be 17 cm/ms, which is much lower than the electron drift velocity equal to 0.45 cm/μs. [30]*

### 3.1.2 Avalanche and proportional amplification

If the intensity of the electric field is high enough to accelerate the electrons to an energy above the ionization threshold of the atoms and molecules of the gas medium, electrons can ionize these gas particles producing additional electron-ion pairs (Secondary ionization). When these newly generated secondary electrons reach consistently ionization energies too, increasing the number of electrons themselves, the system has reached the proportional amplification mode, where this chain reaction increases the number of the electrons exponentially, creating an avalanche of electrons. This configuration is called so because the charge collected by the electrode is proportional to the number of the primary electrons, and it is the region where the MPGDs typically work at.
In the proportional mode the number of $n$ electrons increases by $dn$ after a path $dx$, and

this could be written as:

$$dn = n\alpha dx \tag{3.1}$$

where $\alpha(E)$ is the First Townsend coefficient, defined as the inverse of the free mean path for ionization $\lambda_{ion}$. $\alpha$ could also be written in terms of the ionization cross section $\sigma_{ion}$ as

$$\alpha = N\sigma_{ion} \tag{3.2}$$

where $N$ is the number of molecules per volume unit. It must be stressed that this is the general definition that holds when considering a gas made of a single component. When considering gas mixtures made of multiple components, there are additional factors that influence the number of newly generated electrons, such as the Penning effect (See *Section 3.1.5*). These effects can be taken into account by slightly modifying the definition of $\alpha$:

$$\alpha_{pen} = \alpha \left(1 + r_{pen}\frac{f_{exc}}{f_{ion}}\right) \tag{3.3}$$

where $r_{pen}$ is the probability that an excited gas particle ionizes a gas particle of a different type by Penning effect and the ratio $f_{exc}/f_{ion}$ considers the frequency of excitation events above Penning threshold compared to the ionization frequency.
The relationship between the amplification path $x$ and the average number of final electrons $n$ starting from $n_0$ electrons can be obtained integrating the expression above, which turns out to be

$$n = n_0 e^{\alpha x} \tag{3.4}$$

The proportionality factor between the number of initial and final electrons is therefore

$$G = \frac{n}{n_0} = e^{\alpha x} \tag{3.5}$$

where $G$ is called charge multiplication factor or gain. In other terms $G$ is the mean number of final electrons generated starting by a single electron in a path $x$. The avalanche size probability follows a Polya distribution having the following expression:

$$P(n_e) = \frac{(1+\theta)^{1+\theta}}{\Gamma(1+\theta)}\left(\frac{n_e}{\bar{n}_e}\right)^{\theta} e^{-(1+\theta)\frac{n_e}{\bar{n}_e}} \tag{3.6}$$

where $\bar{n}_e$ is the number of mean electrons in the avalanche, $\theta$ is a parameter such that the expression reduces to a simple exponential when $\theta = 0$ and $\Gamma$ is the Euler gamma function.
In an ideal setup between two parallel plates the expression $x = E/\Delta V$ holds, so as the intensity of the applied electric field $E$ increases, the value of the gain $G$ increases exponentially. This shows how a small variation in the electric field has a large difference in the size of the final avalanche. [30, 33, 34]

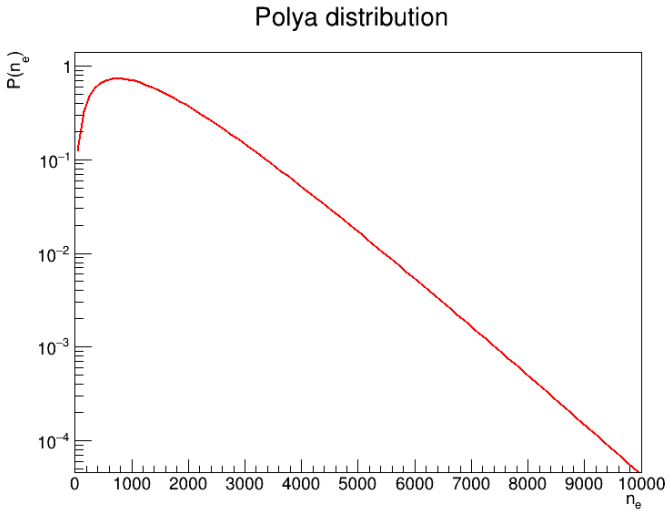


Figure 3.2: *Sample Polya distribution having* $\bar{n}_e = 1500$.

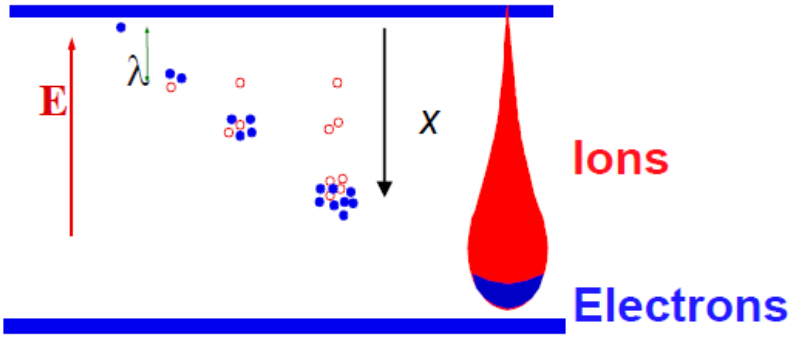


(a)

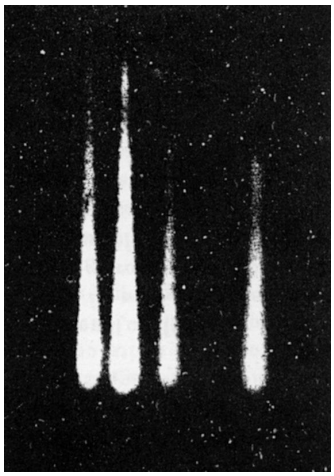

(b)

Figure 3.3: *Diagram showing the progressive evolution of an avalanche (3.3a) and picture of avalanches in a cloud chamber (3.3b).*

### 3.1.3 Space charge effect

The generation of an avalanche in a gas medium leaves behind a cloud of ions which persists much longer compared to the electrons. This is due to the of the difference in their mobility. As a consequence, these ions give rise to spatial charge effects which distort the electric field in the detector, especially at high event rates where ions do not have enough time to be collected as other electrons arrive so they pile up. This shows up as a saturation effect in the charge multiplication factor in the so-called limited proportionality configuration. [30]

### 3.1.4 Secondary avalanches and transition to streamer

When increasing the electric field further, the generation of secondary avalanches becomes a non negligible factor. Differently from the beginning of an avalanche which is triggered by an ionization process, this phenomenon starts from the excitation of a gas atom or molecule induced by an electron. The de-excitation of this particle returning to the ground state implies the emission of a photon having an energy corresponding to the excitation level. If this photon has an energy which is higher than the ionization potential of a gas particle, it could start an avalanche in the gas after propagating for a certain distance from the initial point where the atom or molecule was excited. This means that as the electric field intensity increases and more electrons are produced, the number of emitted photons increases too, meaning that more secondary avalanches will follow the primary one, spreading the charge over the gas medium. This happens mainly in the rear and in the front of the avalanche where the electric field deformation due to space charge effects is more pronounced.
At high electric field values this charge propagation turns an avalanche into a streamer, which could propagate through the whole gas volume leading to a spark breakdown if not damped. This transition point is called Raether's limit. It is reached when $\alpha x \simeq 20$, or at gain values around $10^8$. However considering the probability distribution of the size of an avalanche, a gaseous detector should usually work at lower average gain values to avoid breakdowns, nominally around $10^6$. [30]

### 3.1.5 Penning effect

The Penning effect is a process that may occur in a gas if the energy of a gas molecule excited to an intermediate state is higher than the ionization energy of another gas component. Then a collisional transfer process where the excitation energy of a gas molecule is used to ionize another molecule creates an ion-electron pair by means of the following process:

$$A^* + B \rightarrow A + B^+ + e^- \tag{3.7}$$

where $A^*$ is the gas excited in a metastable state (usually the noble gas acting as the main component of the gas mixture) and B is the other gas component (usually the quencher). This process adds up to the direct impact ionization and contributes to the growth of the avalanches in a gas detector with a high enough electric field, greatly affecting the gain of the setup (See *Section 3.1.2*). Of course the occurrence of this process highly depends on the composition of the gas mixture. [30]

### 3.1.6 Signal induction and Shockley-Ramo theorem

A point charge at a certain distance from a conductive electrode induces a surface charge with a certain distribution on the electrode. The movement of the charge changes the surface charge distribution, implying that it induces a current on the electrode. Such current induction is a very fundamental mechanism as it is the primary source of information of what is going on inside a gaseous detector. Having a good understanding of the mechanism of signal induction is hence important to interpret effectively the outputs of a detector.
It is possible to estimate the induced current using the Shockley-Ramo theorem. The theorem states that the current induced on an electrode by a moving charge is equal to

$$i_{ind} = -qE_V v \tag{3.8}$$

where $q$ is the charge of the particle, $v$ is its velocity and $E_V$ is the electric field that would exist at the position of the particle if the readout electrode was set to unit potential and all the other electrodes were grounded. In other terms, the induced current depends on the charge and on the speed of the inducing particle and on the electric field that can be obtained setting all electrodes to $V = 0\ V$ except for the readout one set to $V = 1\ V$. [30]

## 3.2 Micromegas

The Micro-mesh Gaseous Chamber (Micromegas) consists of a few $\mu m$ thin metal grid stretched at a small distance from the readout electrode, on the order of 100 $\mu m$ (usually 128 $\mu m$ due to the technology of the production procedure). A high voltage difference is applied between the mesh and the electrode, inducing fields between 20-30 $kV/cm$ in the gap. Electrons coming from the drift region enter and multiply in this small gap, potentially approaching even gains that graze the upper limit given by the Raether's condition. To have better mechanical stability and to ensure the uniformity of the gap, insulating pillars are placed with regular spacing to support the mesh.
This sub-millimeter gap configuration was designed specifically to operate at high gain values, and it is the result of the historical development of gaseous detectors and manufacturing technology. Firstly, it resembles a parallel plate configuration having an uniform electric field in the amplification volume. This is not trivial, since other detectors widely used before the MPGD era work with a non-uniform electric field, for instance wire chambers and Micro-Strip Gas Chambers (MSGC). The uniformity of the electric field between mesh and electrode implies favorable statistical properties in the avalanche process. This factor is complemented by the mechanical stability of the parallel plate geometry and its

intrinsic better energy resolution and rate capability. Secondly, the Townsend coefficient shows saturation effects at high field intensities, meaning that the coefficient value depends less on the variations of the field. In other words, applying a high electric field to a small gap reduces the sensitivity of the detector to its imperfections, implying a better stability of the chamber. Furthermore, the mesh is essentially a Frisch grid that separates the gas volume into two parts. This has remarkable beneficial consequences, such as the confinement of the charge multiplication effects in the gap by limiting the backflow of ions into the drift volume, and the limitation of space charge effects thanks to the quick recollection of the positive ions generated in the gap. This short recovery time of the order of 100 $ns$ also implies the high-rate capability of the detector.
The Resistive Micromegas is a variant of the common micromegas that has an additional thin resistive layer of $\sim 50\ \mu m$ over the pads. The resistive layer is usually set at a positive high voltage and is insulated from the pads by an insulator layer. It spreads the incoming charge inducing a signal over several adjacent pads improving the space resolution of the tracks, particularly the ones having a small drift distance hence a small transverse diffusion. Additionally the spreading of the charge prevents charge build-ups and potential sparks in the detector, allowing the operation at higher gains. [30, 35, 36, 37]

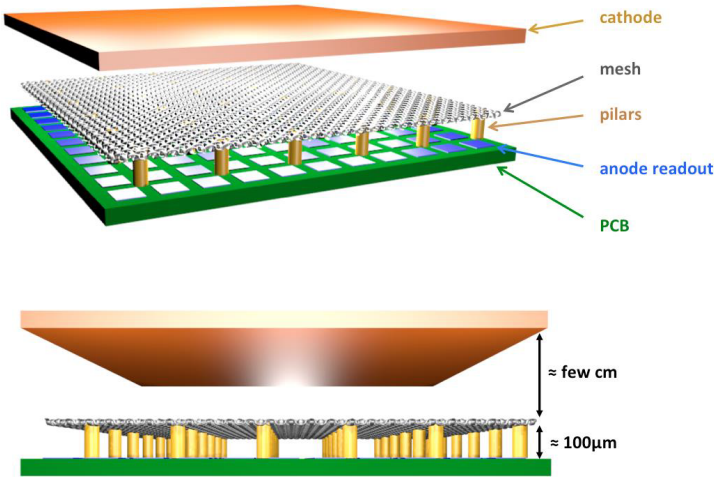


(a)

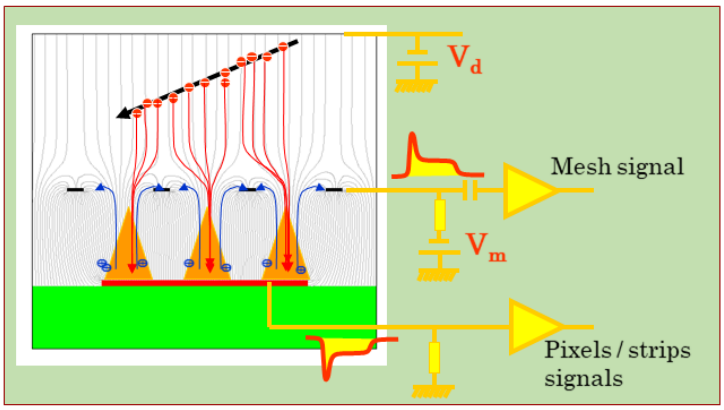


(b)

Figure 3.4: *Model showing the basic geometry of a micromegas (3.4a) and scheme showing its working principle (3.4b).*

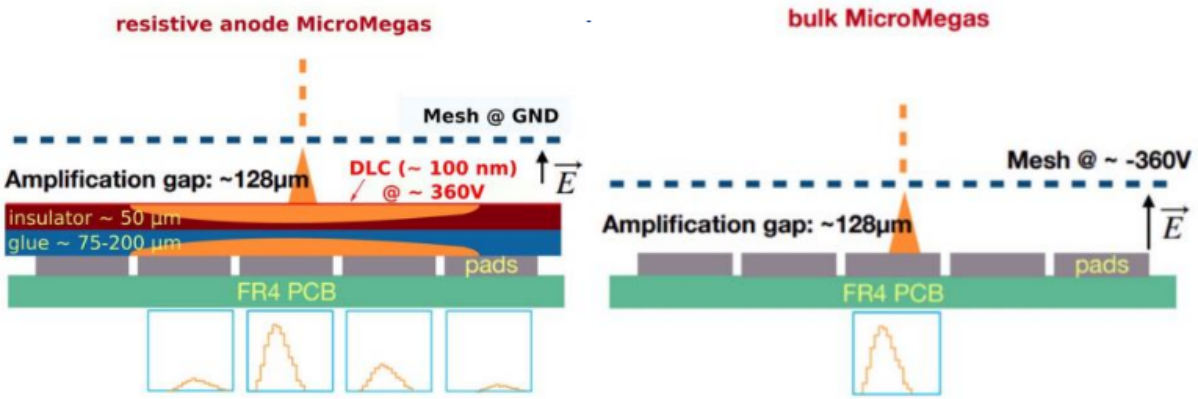


Figure 3.5: *Comparison between a resistive micromegas and a standard bulk micromegas with typical parameter values.*

# Chapter 4

# MPGD simulations in T2K gas

This chapter and first section of this study revolves around Monte Carlo simulations run on Garfield++, a toolkit that allows detailed simulations of gaseous detectors and MPGDs in particular. The aim of these simulations is to gain a better understanding of a gaseous detector using T2K gas and compare the outcomes with real data. In particular, the main focus of this study revolves around the comprehension and prediction of the formation of the signal in the double micro-mesh detector setup discussed in *Section 4.4*. Simulations are exploited to give predictions on the suitable values of parameters to set in the real experimental setups, and their validity is verified if the outcome of the experiment is compatible with the expectations. At the same time these simulations are helpful to have a better qualitative understanding of the detector and its response, and to highlight microscopic effects that were unclear or not considered before.

## 4.1 T2K gas mixture composition

The T2K gas is a mixture of three components: Argon (Ar, 95%), Carbon tetrafluoride (CF4, 3%) and Isobutane (iC4H10, 2%).
Argon is the main component of the mixture, and it's the gas which is most commonly used as a base for mixtures in gaseous detectors. The popularity of this element is the result of mainly two factors:

- Noble gases do not have vibrational or rotational states; in other words they do not have non-ionizing de-excitation modes, meaning that ionization dominates and charge multiplication can be achieved at relatively low electric fields;
- Noble gases with larger atomic number $Z$ are preferred since they have bigger dimensions, therefore the cross section with the ionizing particle increases and a larger number of primary ionizations would be attained; however Kr and Xe are rare and expensive while Rn is radioactive, so Ar is a good cost-performance compromise.

Isobutane is introduced in the mixture as a quenching gas, meaning that it absorbs the photons emitted by the de-excitation of excited Argon atoms to ground state. These photons could potentially photoextract electrons from the cathode and cause further avalanches leading to discharges in the detector at relatively low gain values. Isobutane contains the propagation of these photons dissipating their energy through elastic collisions and allows an operation of the detector at high gain values. Indeed, the presence of this quencher in the mixture brings up the upper limit of the detector gain by even two orders of magnitude compared to the operation in pure Ar gas.
Carbon tetrafluoride increases the drift velocity of the charged particles and lowers their diffusion. Diffusion and drift velocity are both properties that describe the motion of the electrons in the drift region, but still have a large impact on space and time resolution of the readout signal.

## 4.2 Gas modeling and simulation limits

One of the current largest limits of a Garfield++ simulation in T2K gas comes from the limited capability to simulate the ions. When simulating the motion of electrons in a given gas, Garfield++ interfaces the Magboltz program, which calculates the input transport parameters of the gas using the stored electron-atom/molecule cross section data, allowing the microscopic tracking of the electron in the simulation. However this is not possible for ion tracking, since there is no corresponding program able to compute such parameters. As a result only a little variety of ion parameters in specific gases is supplied from external files, allowing just an approximate computation of the ion track.
This combines with the complexity of the T2K gas mixture, which is a three-component gas, implying that many more interaction channels thus product ion types are available in the medium. As a consequence, simulation data involving ion tracking should be taken with a grain of salt, considering more the qualitative aspect of the result rather than the numerical values.
The Penning effect is included in the simulations and can be controlled by fixing the parameter $r$ (equivalent to the $r_{pen}$ in *Equation 3.3*), which represents the probability of an excited state to cause a Penning transfer in a collision. The program is able to calculate autonomously this transfer parameter only for few gas mixtures using pre-implemented parametrizations taken from literature, and generally it has to be manually set by the user. This "effective Penning coefficient" can also include the effects of secondary avalanches generated in a multiplication process by properly adjusting the $r$ value to match the experimental data, even if the microscopic tracking does not include the process.
In the following simulations, all the ions will be considered as $Ar^+$ moving in pure Ar, which is a fair approximation considering that Argon makes up 95% of the gas mixture. Additionally, it must be stressed that Garfield++ can only compute the tracks of the

electrons singularly, meaning that it is not able to consider space charge effects that are not already implemented in the field map in complex geometries, such as the effect coming from the other charged particles in the same avalanche.

## 4.3 Micromegas simulations

Micromegas simulations were run using a geometric model obtained by looping periodically a small cell element along the $x$ and $y$ axis. The model used in the simulation can be split into three sections: drift volume, mesh and amplification gap.

- The drift volume is 700 $\mu m$ high and it has a relatively low electric field intensity of few hundreds of $V/cm$. Typically the electrons in the simulations were released few tens of $\mu m$ below the upper edge of the central cell to avoid an overabundance of electrons going out of bounds because of diffusion effects. If additional drift distance was required, electrons were drifted separately in a parallel plane simulation having arbitrary travel distance. The data of the resulting electrons served as input of the micromegas simulation, which still has a uniform electric field at the starting height.
- The mesh has a 63 $\mu m$ wire pitch in both $x$ and $y$ directions, deriving by the displacement of 18 $\mu m$ thick conductive wires so that they make 45×45 $\mu m^2$ holes. In reality, in the T2K ERAMs, but also in most of the micromegas applications, the mesh is woven and then flattened to decrease the thickness in the intersections. Considering the complexity to model such a geometry, the mesh was approximated to intersecting cylinders in these simulations, which is a good compromise as it will be shown in *Section 4.3.4*.
- The amplification gap is 128 $\mu m$ high and it hosts a high intensity electric field. The applied voltage configuration replicates the 350 $V$ of the T2K HA-TPCs, meaning that the gap is characterized approximately by a 28 $kV/cm$ electric field.

The pillars supporting mechanically the mesh were not included in the simulations. The conductive bodies having adjustable voltage in order to generate the electric fields are the upper cathode surface, the mesh and the lower anode surface. The geometry and the electric field map of the cell were obtained using two different softwares, respectively Gmsh and ElmerFEM.

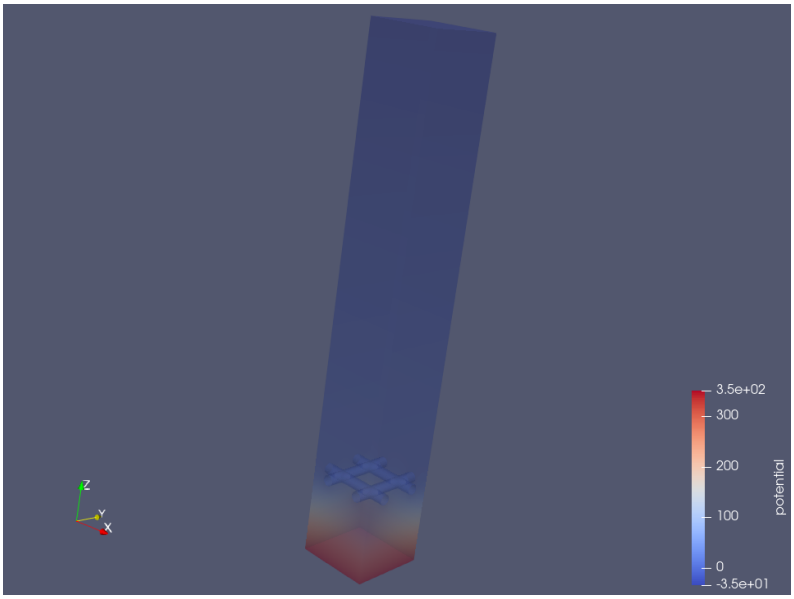


Figure 4.1: *Single micromegas cell including the map of the electric potential inside of it.*

| Layer | Thickness ($z$ axis) | Cumulative height |
|---|---|---|
| Drift volume | 700 $\mu m$ | 846 $\mu m$ |
| Mesh | 18 $\mu m$ | 146 $\mu m$ |
| Amplification gap | 128 $\mu m$ | 128 $\mu m$ |

Table 4.1: *Summary of the layers along the vertical axis composing the micromegas geometric model.*

### 4.3.1 Field map and sample event

*Figure 4.2* shows the field map in a simulated micromegas detector in a standard T2K HATPC field configuration, meaning that $E_{drift} = 275\ V/cm$ and $\Delta V_{gap} = 350\ V$, i.e. $E_{gap} = 350/128\ V/\mu m \approx 28\ kV/cm$. Though the field intensities may vary slightly, this configuration is the basis of all of the following simulations in this section concerning micromegas.
It is clearly visible from both plots that the electric field is mostly uniform, in particular far from the mesh: in the first plot the equipotential lines are mostly horizontal and evenly spaced, while in the second plot the derivative of the plotted function is approximately linear when far from the mesh at 0.0128 $cm$. The only deformation of the field occurs close to the mesh, where the equipotential lines are no longer horizontal. As it will be discussed in *Section 4.3.5*, the distortion level of the field lines depends on the ratio of the electric fields above and below the mesh. This deformation affects the transparency for the electrons trying to pass through the mesh, while simultaneously gatekeeping the

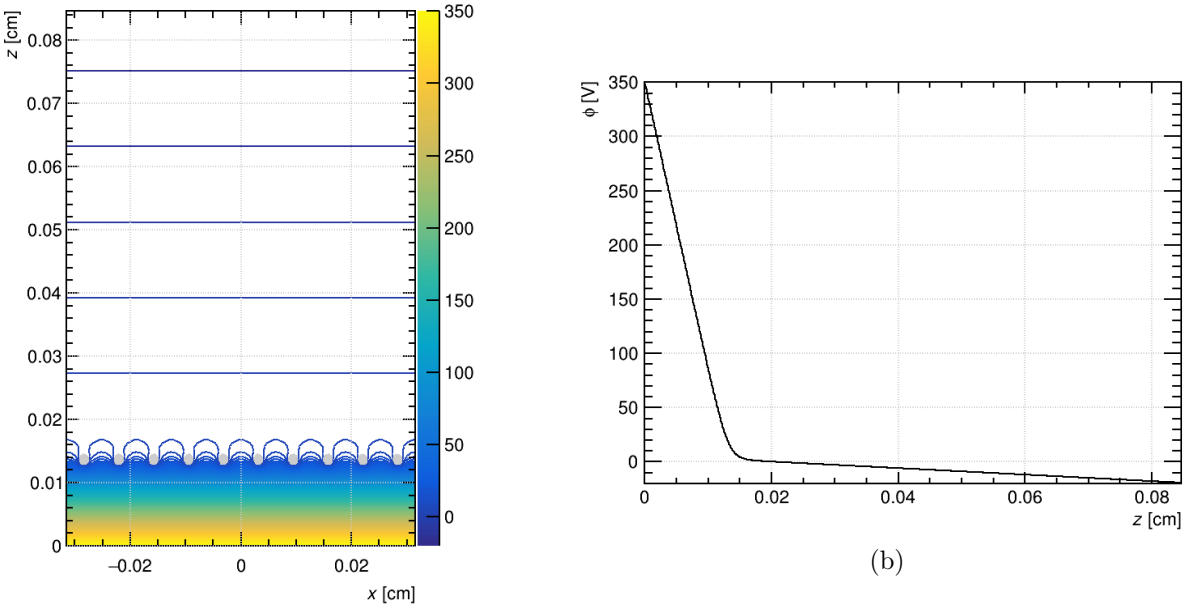


(a) (b)

Figure 4.2: *Plot of equipotential lines in the simulated micromegas detector (4.2a) and plot of the potential profile moving along $z$ at $x, y = 0$ (4.2b). The side section of the mesh is visible in light gray in the left plot. The potentials are set such that $E_{drift} = 275\ V/cm$ and $\Delta V_{gap} = 350\ V$ so $E_{gap} \approx 28\ kV/cm$.*

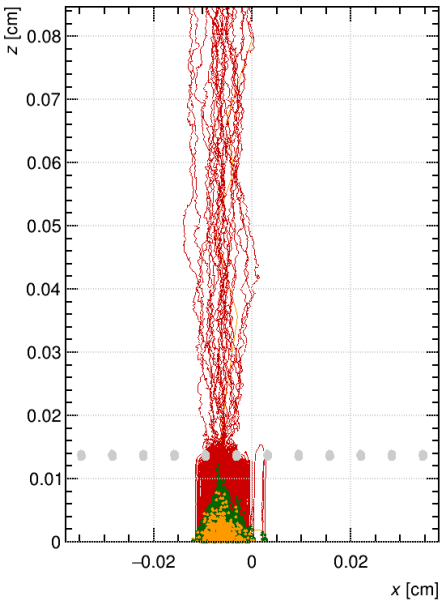


Figure 4.3: *Sample avalanche event in the field configuration shown in Figure 4.2. Orange tracks are the electrons, red tracks are the ions and green dots are the ionization points. The transverse spread of the avalanche is approximately equal to the height of the mesh.*

drift volume from the ions generated in the amplification gap that try to drift towards the cathode.
*Figure 4.3* shows a sample avalanche event in the previous field configuration. This event is a good example of what just mentioned. Indeed, most of the ions generated in the gap drifting upwards are collected by the mesh and do not make it through the grid. This is particularly clear observing the ions on the right edge of the avalanche, where an ion visibly bent its trajectory towards the mesh wire.

### 4.3.2 Penning Coefficient

As mentioned in *Section 4.2*, the determination of the $r$ Penning transfer coefficient is crucial to be able to run a plausible avalanche simulation in T2K gas. This coefficient is obtained empirically, by comparing simulation results with empirical data and adjusting the $r$ value so that the simulation results match the experimental results.
The derived plot showing the dependence of the gain on $r$ is displayed in *Figure 4.4*. The drift field was set to 500 $V/cm$ and a voltage difference of 350 $V$ was applied to the amplification gap. 5000 events were simulated at different $r$ values, and each mean gain value shown in the plot was obtained fitting the obtained gain spectra with a polya distribution. The data is well fit by an exponential curve. This plot was compared with experimental data, namely the mean gain of the micromegas used in the T2K HA-TPCs running in a similar configuration.
The two gain values match at $r = 0.385$, meaning that simulated events resemble the real

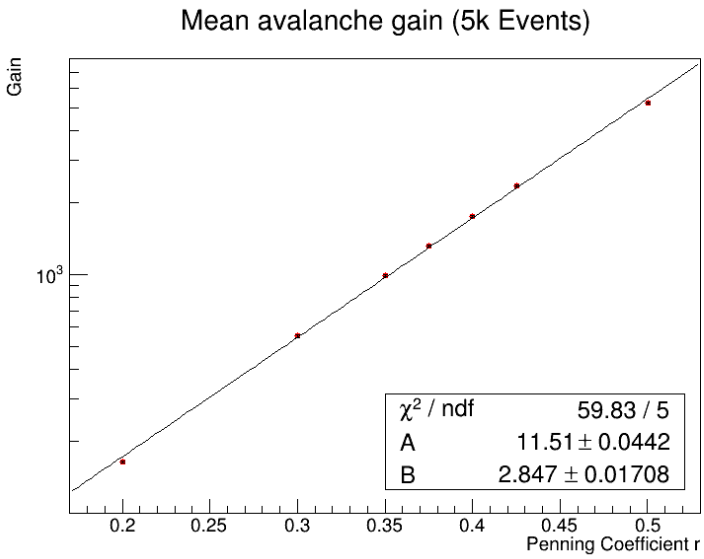


Figure 4.4: *Avalanche gain dependence on the Penning transfer probability r in the simulated micromegas detector in T2K gas. The simulation was run having* $E_{drift} = 500\,V/cm$ *and* $\Delta V_{gap} = 350\,V$. *Each gain is obtained by fitting the Polya distribution obtained by 5000 avalanche events at the set r value.*

ones when $r$ is set to 0.385. All of the following simulations, including the double-mesh detector ones in *Section 4.4*, will use as the Penning transfer coefficient of the T2K gas $r$ = 0.385.

### 4.3.3 Gap height vs Gain

The dependence of the gain on the variation of height of the amplification gap was studied to see the effects of local gap height variations due to potential production defects or other external factors. In a real situation the electrodes of the detector are supplied a fixed voltage, independently from such geometrical irregularities. This means that even if the height of the mesh might change locally, its potential is set to be the same everywhere, implying that the intensity of the electric field in the amplification gap is also affected.
This simulation "at constant $\Delta V$ in the gap" was compared with a simulation "at constant E in the gap", where the intensity of the electric field in the gap was kept to be the same by adjusting the potential of the mesh accordingly to its height. Both simulations were run changing the height of the gap up to $\pm 15\ \mu m$ from the nominal 128 $\mu m$, and the result is displayed in *Figure 4.5*. The drift field was set to 500 $V/cm$, while the amplification gap was subject to $E_{gap} = 350/128 \cdot 10^4\ V/cm$ in the constant $E$ case and to $\Delta V_{gap} = 350\ V$ in the constant $\Delta V$ case.
The two cases show a notably different behavior. In the "constant $E$" case, the data follows an exponential trend as expected from *Equation 3.5*, since the Townsend coefficient $\alpha(E)$

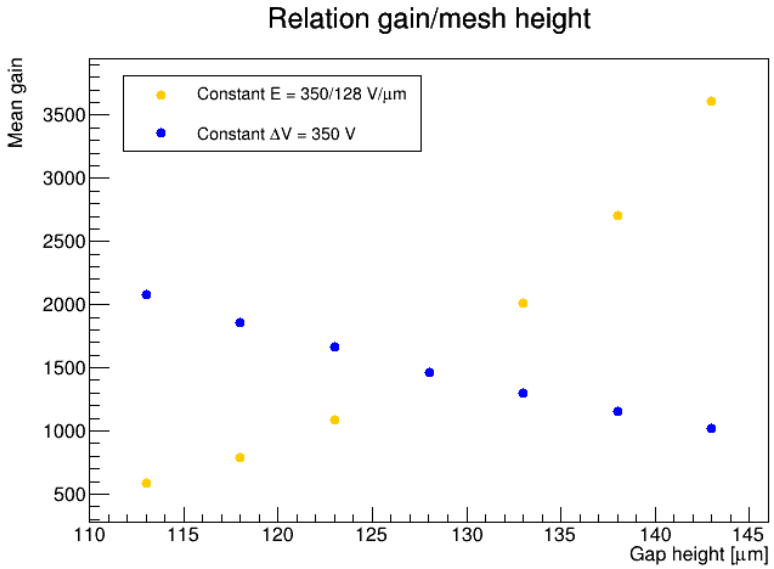


Figure 4.5: *Avalanche gain dependence on the height of the mesh in the simulated micromegas detector in T2K gas considering constant $E_{gap} = 350/128 \cdot 10^4\ V/cm$ in the gap (in orange) or constant $\Delta V = 350\ V$ (in blue). The simulation was run having $E_{drift} = 500\ V/cm$.*

is constant at fixed pressure and temperature[6]. On the other hand, in the more practical "constant $\Delta V$" case, $E$ is no longer constant and it depends on $h$ approximately as it does in a parallel plate capacitor, i.e. $E = \Delta V/h$. This has a huge impact on the performance of the detector, as it changes completely its performance. Indeed the effects of the variation of $E$ make it so that the mean gain of the detector decreases as the distance between mesh and anode increase, oppositely to the previous situation.
It should also be stressed that in the $\Delta V$ case the variation of the gain is more limited than the $E$ case, where a slight variation of $h$ leads to a large variation of the gain. This means that a hypothetical implementation of the latter configuration would be affected more by the mechanical imperfections of the detector compared to the former one.
Overall, this outcome highlights the importance to consider the practical $\Delta V$ between the two electrodes to be constant instead of the ideal electric field for these kind of simulations where the height of the mesh is not constant.

### 4.3.4 Space distribution of the electrons inside the hole

This section studies how the electrons are distributed inside the holes when passing through the mesh and their properties. *Figure 4.6* displays the positional distribution of the electrons reaching the height of the mesh at $z = 146\ \mu m$. The drift field was set to 275 $V/cm$ and a voltage difference of 350 $V$ was applied to the amplification gap. In order to avoid potential biases following from the starting point of the electron drift, the electrons were generated as the ionization product of 70 muon tracks crossing the gas medium horizontally 5.07 $cm$ above the mesh (700 $\mu m$ cell drift volume + additional 5 $cm$ drift in a separate parallel plate simulation). It must be stressed that these plots are distributions on the $xy$ plane at $z = 146\ \mu m$, which is essentially the plane which lays right on top of the mesh. This means that this is the distribution of the electrons right before entering the mesh holes and essentially no electron has been caught by the grid yet.
Thanks to the field lines configuration given by the disparity of the electric field intensities on the two sides of the mesh, the electrons tend to avoid the wires and move towards the center of the hole, mostly making through it and causing this centered distribution. As a consequence this causes the edges of the distribution to have very few remaining electrons, which are more likely to end up on the mesh surface. The projection of the mesh wires on the plane of the plot locates at $|x|, |y| > 22.5\ \mu m$, and it is clearly visible in all plots that the number of electrons drops greatly when approaching this bound.
The corners of the hole are the regions where the simulation is the least accurate because of the different geometry between intersecting cylinders and overlapped and pressed wires. However it is possible to quote that this should have a minor effect on the performance of the micromegas, since very few electrons approach these regions and are affected by

[6]Simulations are run at STP.

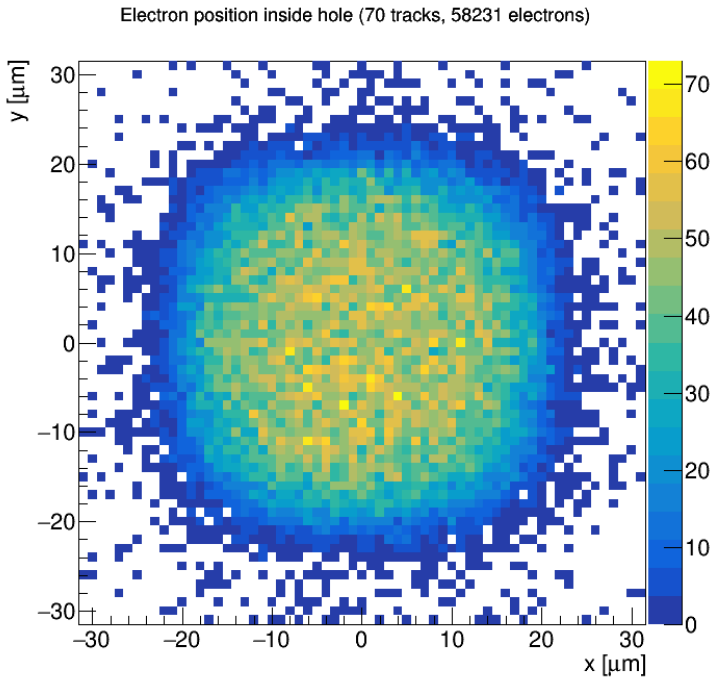


(a)

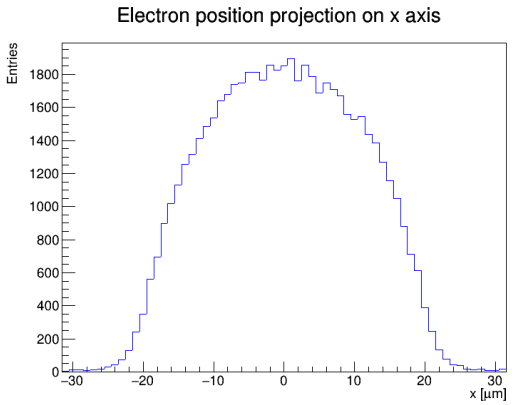


(b)

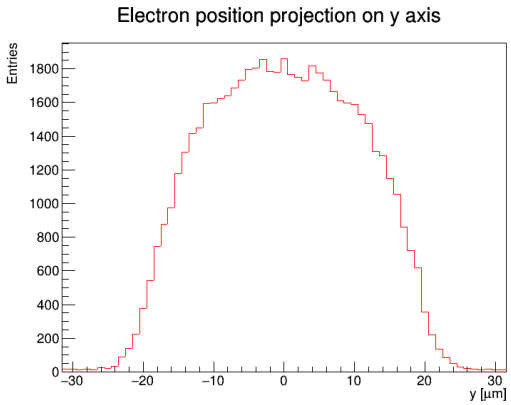


(c)

Figure 4.6: *Distribution of $x$ and $y$ position of the electrons reaching the mesh height $z = 146$ $\mu m$ inside a mesh hole (4.6a) and its projection along the $x$ (4.6b) and $y$ (4.6c) axis. Since the plots are centered on the hole and its dimensions are $45$ $\mu m \times 45$ $\mu m$, the projection of the mesh wires on the $xy$ plane locates at $|x|, |y| > 22.5$ $\mu m$. The simulation was run having $E_{drift} = 275$ $V/cm$ and $\Delta V_{gap} = 350$ $V$.*

such issue. Therefore it is possible to say that the geometric model using a mesh made of intersecting cylinders is a good compromise.

The distribution of the electron energies depending on their position shown in *Figure 4.7* shows that the electrons passing through the center of the hole are more energetic compared to those passing on the edges. Once again this is a consequence of the distortion of the electric field, which has a lower impact on the electrons passing through the center

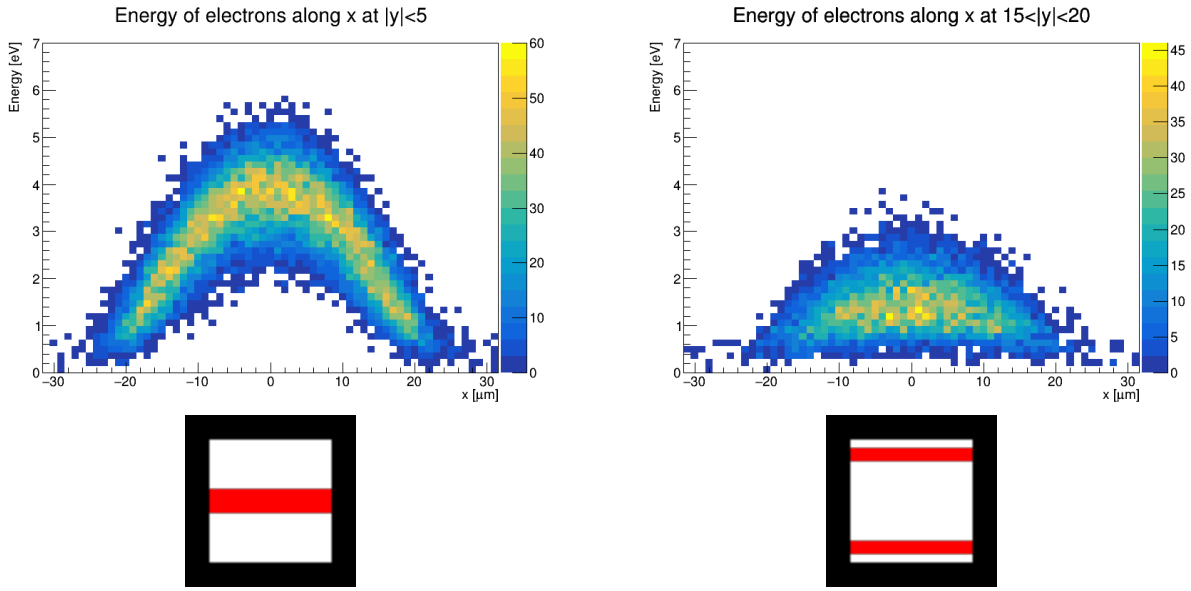


(a) (b)

Figure 4.7: *Energy distribution of the electrons reaching the mesh height varying position along the wire direction in the center (4.7a) and on the edges (4.7b) of the hole, accompanied by the respective schemes showing the considered area inside the hole. Data of the same simulation as Figure 4.6.*

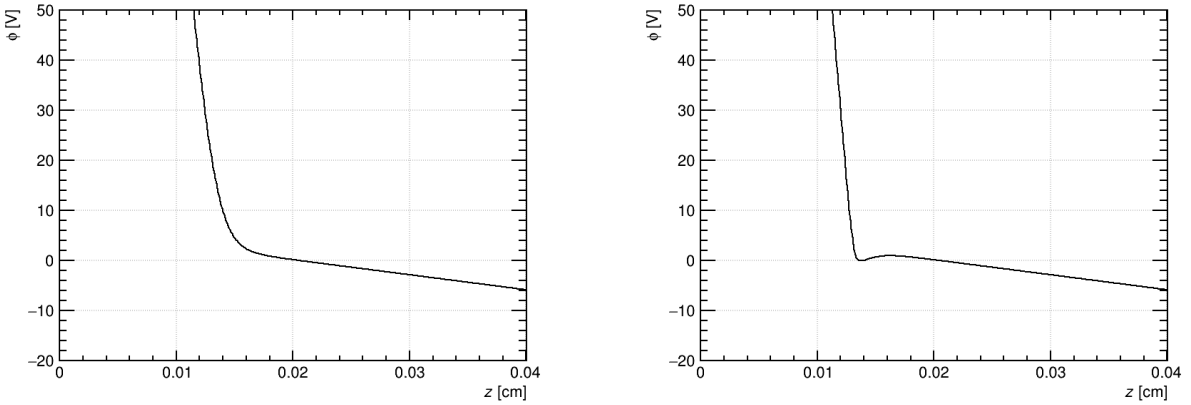


(a) (b)

Figure 4.8: *Detail of the potential profile in the simulated detector moving along the vertical z axis in the center of the hole at x, y = 0 µm (4.8a) and close to the edge at x, y = 22 µm (4.8b).*

of the hole. Indeed, as can be seen in *Figure 4.8*, the electrons approaching the corner of the hole bump into a small potential barrier that slows them down and changes their momentum direction, while this effect is absent in the center of the hole.
*Figure 4.9* displays the mean gain of the electrons passing through the hole depending on their position inside the hole. It's clear in both plots that the avalanche size increases as the distance from the center of the hole goes up. This effect may be explained by the fact that the electric field lines close to the mesh are slightly longer than those near the center of the hole. Since charged particles move approximately following the field lines,

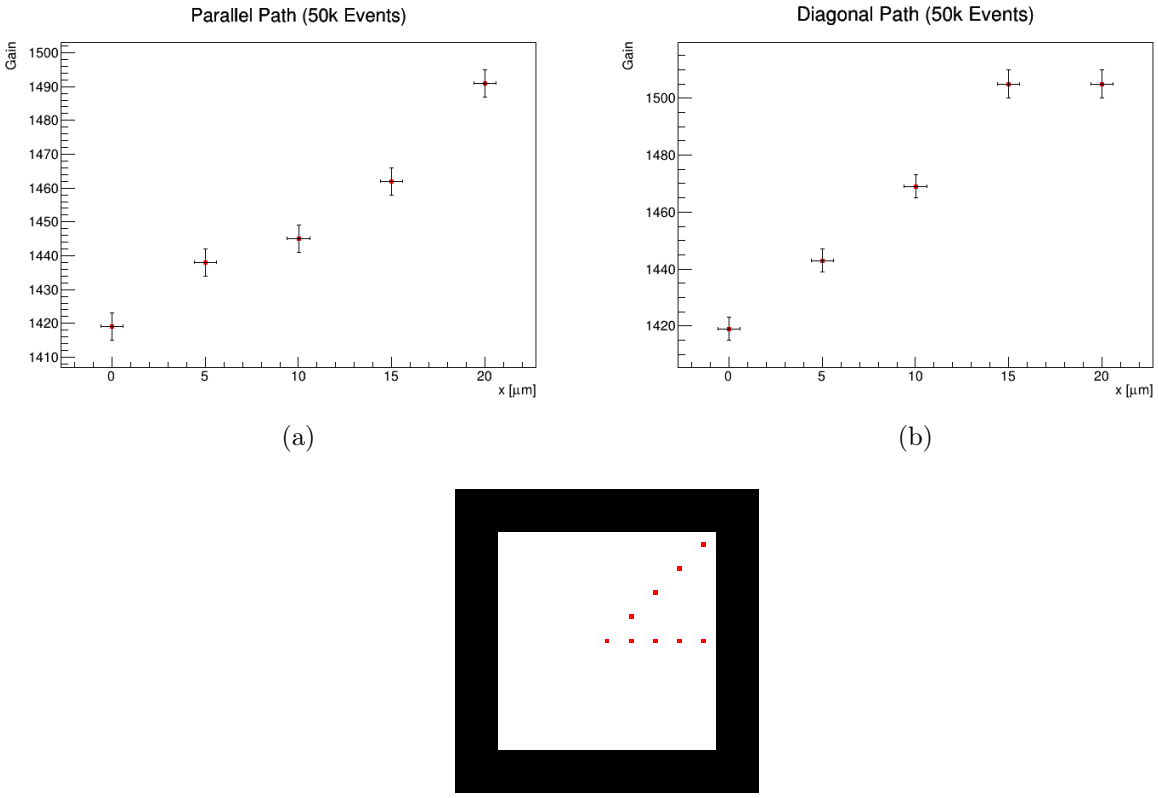


Figure 4.9: *Gain values of electrons passing through the hole in different positions along the wire direction (4.9a) and along the hole diagonal (4.9b), accompanied by a scheme displaying the position of the considered electrons inside the hole. Each gain value was obtained from a Polya fit distribution of about 50000 avalanches starting from each position.*

it follows that the edge electrons have a slightly longer multiplication path compared to the center electrons, resulting in a slightly higher gain value.
It must be reminded though that the number of electrons on the edges is much lower compared to the ones near the hole center, which have a dominant effect on the overall performance of the micromegas. Additionally, the effective gain of the edge electrons are lower than the result shown in the plot, which only considers the successfully passing and multiplying electrons. In fact, as the electron transition point moves towards the edges and corners of the holes, the probability of it being collected by the mesh starts to be non negligible, and the effective gain of the detector is reduced compared to the case where all electrons multiply.

### 4.3.5 Transparency

A micromegas does not work as intended if set in an inappropriate electric field configuration, as an excessive number of electrons might be caught by the mesh and a large

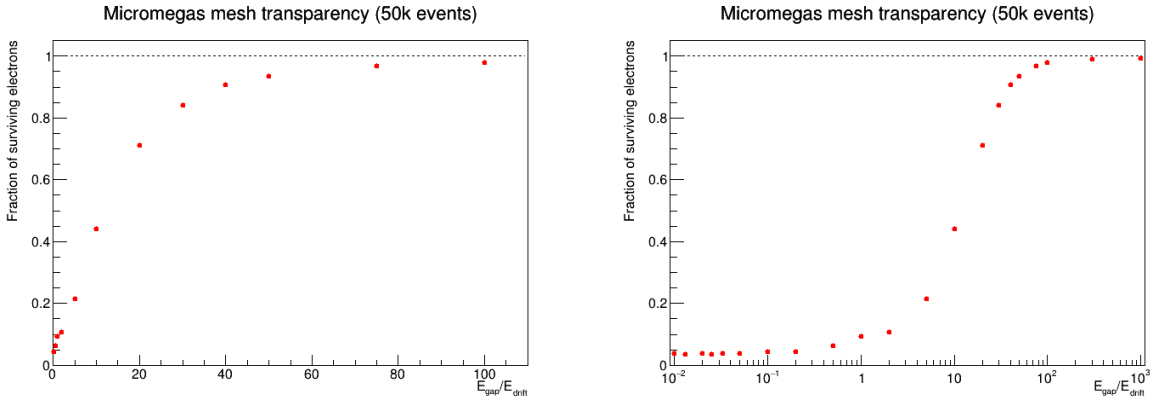


(a) (b)

Figure 4.10: *Transparency of the electrons passing through the mesh from the drift volume to the amplification gap varying the ratio between the electric fields on the two sides of the mesh (4.10a) and extension of the previous plot along the x axis in logarithmic scale (4.10b). The highest field in the ratio was set to 6000 V/cm for each configuration and the other field was calculated accordingly. Each dot is derived from 50000 electron drift events.*

number of ions might make it through the grid into the drift volume. The study of the transparency of the mesh depending on the field intensities on the two sides of the mesh is therefore a key element in order to have a better understanding of the detector and giving correct estimates of its performance.

This study was carried out considering single electrons drifting in electric fields that are not intense enough to start an avalanche, namely up to 6 $kV/cm$[7], for mainly two reasons. Firstly, in a micromegas setup the multiplication process usually generally starts after the mesh and not before it, meaning that the study of the behavior of a single electron gives a more accurate insight on the transparency trend. Secondly, studying the electrons of an avalanche passing through the mesh means that the position of such electrons depend on each other at a certain extent, and this fact might introduce unwanted and unclear biases in the data.

*Figure 4.10* displays the transparency of the mesh, i.e. the fraction of electrons that make it through the mesh during the drift process in various electric field intensity configurations. Considering that the optical transparency of the mesh is $\approx 0.51$, even though it was expected at a certain extent, it is interesting to see that the effective transparency at ratio = 1 is much lower than that, at a value of 0.093. This follows from the fact that the field lines must end perpendicularly on surfaces, meaning that the field lines ending on the mesh wires inside the hole occupy a non negligible area inside the hole and that the fraction of field lines that passes through the mesh without ending up on it is quite low. The transparency increases as the ratio goes up, exceeding 0.9 as the ratio reaches values around 40 before. After this point the transparency increasing speed drops down and it almost stabilizes, approaching very slowly towards 1. A similar behavior can be observed

[7]The reason of the choice of such electric field strength will be explained in *Section 4.4.4*.

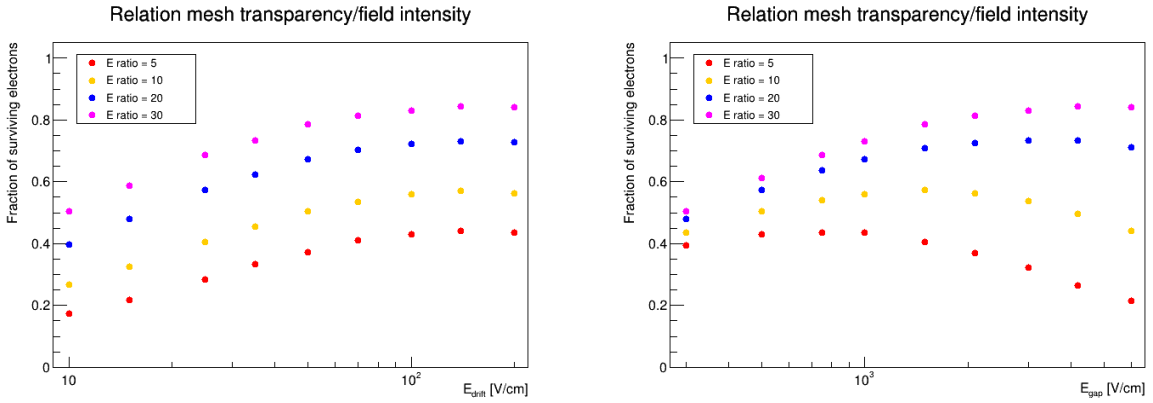


(a) (b)

Figure 4.11: *Transparency of electrons passing through the mesh from the drift volume to the amplification gap varying the intensity of the electric fields on the two sides of the mesh keeping a constant ratio between them, ordered by $E_{drift}$ (4.11a) and by $E_{gap}$ (4.11b). Each dot is derived from 50000 electron drift events, and the used electric fields did not exceed 6000 V/cm.*

in the opposite direction decreasing the ratio between the fields, meaning $E_{drift} > E_{gap}$, where the transparency goes down and stabilizes around 0.03-0.04.
At a first glance, all of these observations would simply lead to the idea that the higher the ratio the better. However this ratio cannot be increased arbitrarily since an excessively low drift field will allow a recombination of the primary electrons and an excessively high amplification field will lead to discharges and detector instability. It should be stressed that the ratio between the electric fields in the standard T2K HATPC configuration is $\approx$ 100, and in all of the other sections concerning micromegas simulations it is always above 50, therefore the number of electrons stopping on the mesh is very small.
Additionally, it must be reminded that both the fractions of passing electrons and ions flowing back are bound to the shape of the field lines. Therefore the two observables are related to each other and the backflowing ions, facing the field lines from the opposite direction, will follow a behavior that is the opposite of the one of the incoming electrons. This means that as the electron transparency increases the number of backflowing ions decreases, solving two issues at once. The ion backflow in the standard T2K HATPC configuration is discussed more in detail in *Section 4.3.7*.
*Figure 4.11* instead shows the dependence of the transparency on the intensity of the electric fields at fixed field ratios. It turns out that the transparency does indeed depend on the intensity of the fields even if the ratio between them is kept constant. In this energy range its value initially increases slightly as the electric fields gain intensity, but then it reaches a maximum and then it even starts decreasing as the fields keep increasing.

### 4.3.6 Signal induction on the anode

The movement of charged particles in the gas medium induces an electrical signal on the electrodes. These signals are the interface to understand what is going on inside a real detector, therefore a good understanding of the induced signal implies a good understanding of the performance of the detector. However, the simulation of the induction of a signal involves the time evolution of the event differently from the previous steps where time played a minor factor and the spatial topology mattered more. This introduces a limit in the simulation capability as mentioned in *Section 4.2* because of the limited knowledge of the mobility of the ions in T2K gas. Therefore the results of this simulation should be considered in their qualitative aspects rather than the precise numerical values.
*Figure 4.12* displays the results of the simulation. The drift field was set to 275 $V/cm$ and a voltage difference of 350 $V$ was applied to the amplification gap. For the above

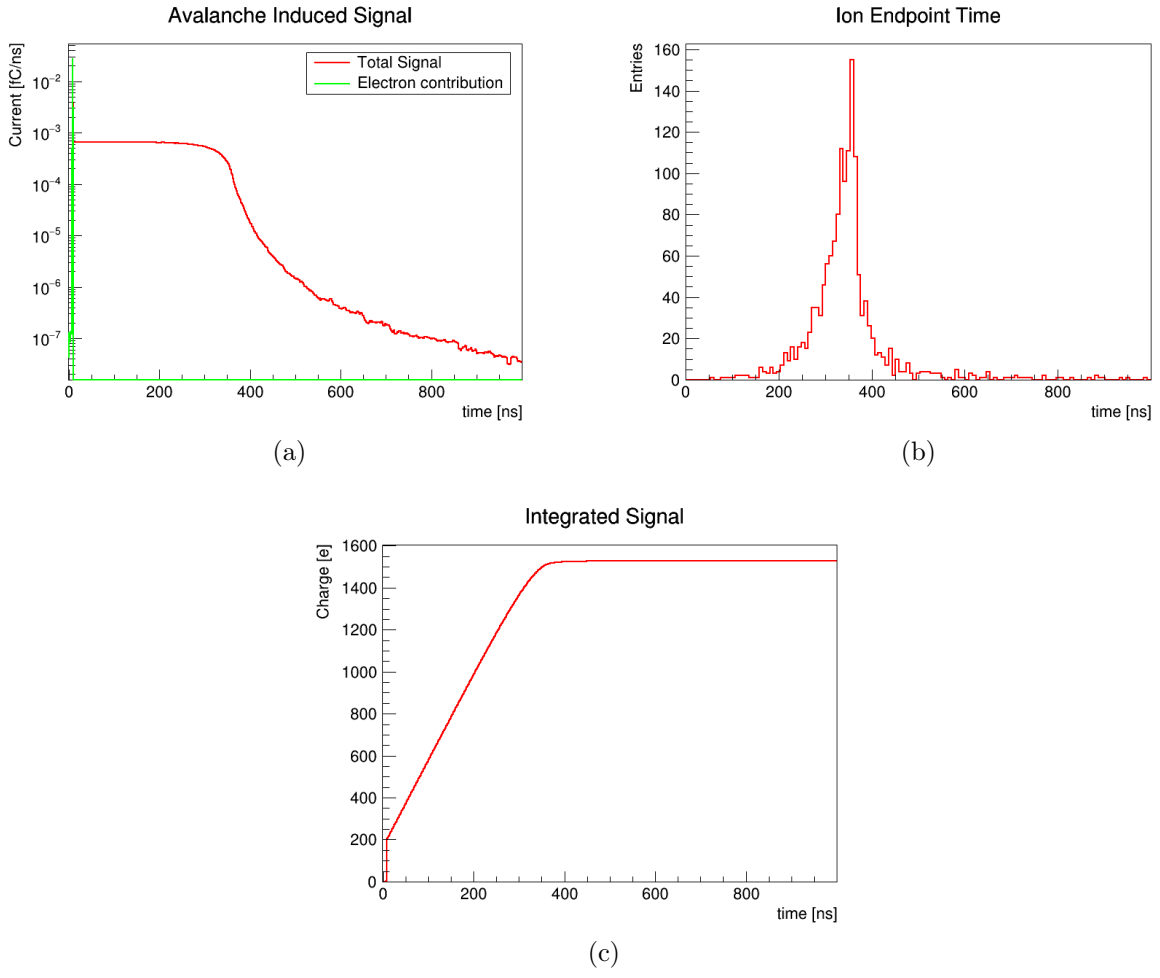


(a) (b)

(c)

Figure 4.12: *Electric signal induced by an avalanche on the anode of a micromegas in all of its components (4.12a), sided by the time at which the ions are collected by the electrodes (4.12b) and the cumulative signal induced on the anode (4.12c). The simulation was run having* $E_{drift}$ *= 275* $V/cm$ *and* $\Delta V_{gap}$ *= 350* $V$.

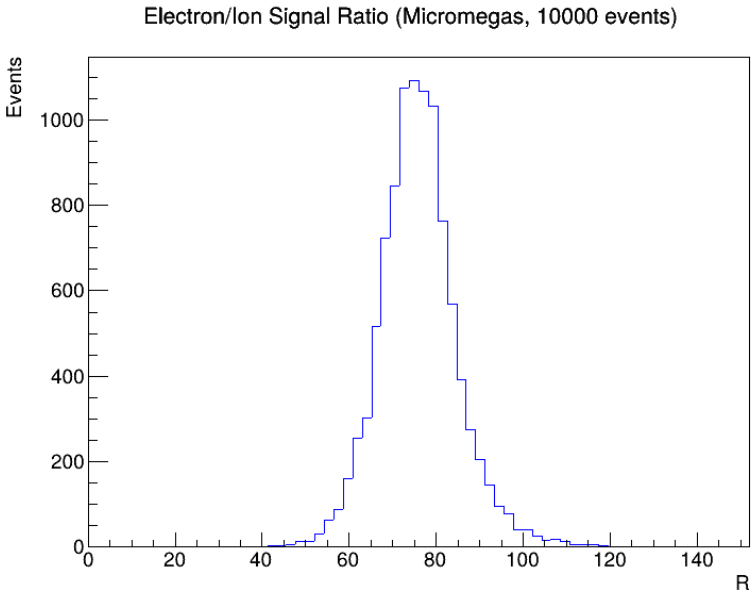


Figure 4.13: *Histogram of the distribution of the signal ratio of 10000 avalanche events.*

mentioned reasons the time scale is not accurate, as the recollection time of the ions is expected to be faster in T2K gas, slightly below 100 $ns$. However the shape of the signal should not be affected much by the approximation since the mechanism of charge multiplication and ion drift themselves are mostly the same.
The induced signal can be roughly split into three sections. The first one is the electron contribution, which is a narrow peak at the beginning of the signal. The peak is very fast since it's induced by the electrons that are collected rapidly by the anode after multiplying in the gap. The high amplitude of the signal can be explained by the Shockley-Ramo theorem (*Equation 3.8*), according to which the induced current is proportional to the velocity of the charged particle. The second section appears as an almost flat plateau, and its the result of the slow drift motion of the ions moving towards the mesh and the cathode. When most of these ions are collected by the mesh, the signal drops further, moving to the last section where the signal is given by the ions moving in the drift volume beyond the mesh towards the cathode. It should be stressed that the last part of the signal is very tiny as it is visible from the scale on the $y$ axis of *Figure 4.12a*, and that this tail is generally not visible in a real setup as it blends with background noise fluctuations. The smallness of this section of the signal is not simply a consequence of the reduction of the number of ions in the mesh-crossing process, but it is also due to the screening effect of the mesh staying between the readout electrode and the charged particle.
The cumulative signal shows an interesting result too, as the total charge induced on the anode stabilizes at around $1500e$. This is equal to the value of the sample avalanche gain, which is approximately $1500e$. In other terms the cumulative signal reaches approximately a value equal to the number and negative charges collected by the readout electrode as a consequence of the Shockley-Ramo theorem.

*Figure 4.13* displays the distribution of the "Signal ratio" quantity $R = i_{emax}/i_{ionmax}$, which is the ratio between the maxima of the electron and ion components of the current signals. This quantity is an index of the ion tail suppression, and it will be used in *Section 4.4.5* to quantify the suppression capability of the double-mesh detector compared to the micromegas.

### 4.3.7 Ion backflow

Ion backflow refers to the fraction of ions generated in the amplification gap in a single avalanche that make it through the mesh into the drift region. Obviously, as for the transparency of the mesh for electrons, this value depends on the ratio between the electric fields on the two sides of the mesh. In this case, the fields were considered in a standard T2K TPC configuration, meaning that the ratio between the fields is >100. *Figure 4.14* displays the distribution of ion backflow for 1000 avalanches and the dependence of their value on the gain of the avalanche. The drift field was set to 275 $V/cm$ and a voltage difference of 350 $V$ was applied to the amplification gap. As expected from the high field ratio, the ion backflow usually has a low value peaking around 1-2%. The distribution features a tail having a slightly higher backflow fraction which is mainly due to avalanches of smaller size. This is simply a consequence of the fact that the occasional fluctuation of the number of passing ions has a larger impact on small-sized avalanches compared to big-sized ones. Indeed, low gain avalanches have most of their backflow fractions at low values too, and taking into account large gain avalanches too it's safe to say that the tail events have a minor impact on the major trend and to an eventual estimate of the number of backflowing ions.

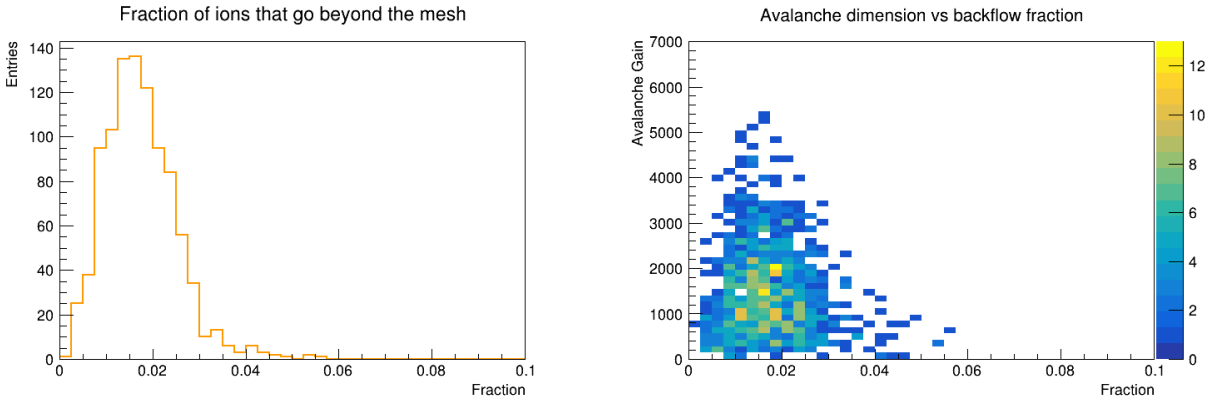


(a) (b)

Figure 4.14: *Fraction of ions flowing into the drift region for 1000 avalanche events (4.14a) and relation between avalanche size and backflow fraction (4.14b). The simulation was run having* $E_{drift} = 275\ V/cm$ *and* $\Delta V_{gap} = 350\ V$.

### 4.3.8 Ion and electron diffusion along a drift distance

The diffusion of charged particles along a certain drift distance does not directly involve the performance of the micromegas working on a very small dimension scale. However its study has an important role in understanding the impact of the backflowing ions in the drift region and potentially on the cathode. The simulations were run considering a parallel plate setup and drifting the particles for 1 $m$, which is equal to the drift length inside the T2K HATPC.
The results are shown in *Figure 4.15*. The electric field was set to 275 $V/cm$. Once again, the time related data of the ion case should only be considered qualitatively because of the limited knowledge of the ion mobilities. Both cases have their particles distributed in a gaussian distribution in drift time, $x$ and $y$ position. The positional spread of the ions is smaller compared to the one of the electrons because of their reduced mobility, but they are both around a few $cm$ spread along a meter long drift distance. Even considering the approximated ion time result, the drift time displays a completely different time scale for the two cases as expected from their difference of mobility.
This result should be considered as an upper limit, since the HATPCs are also subject to a magnetic field which is parallel to the direction of the electric field. This limits the transverse diffusion of the charge during the drift of the charges thanks to the E×B effect.

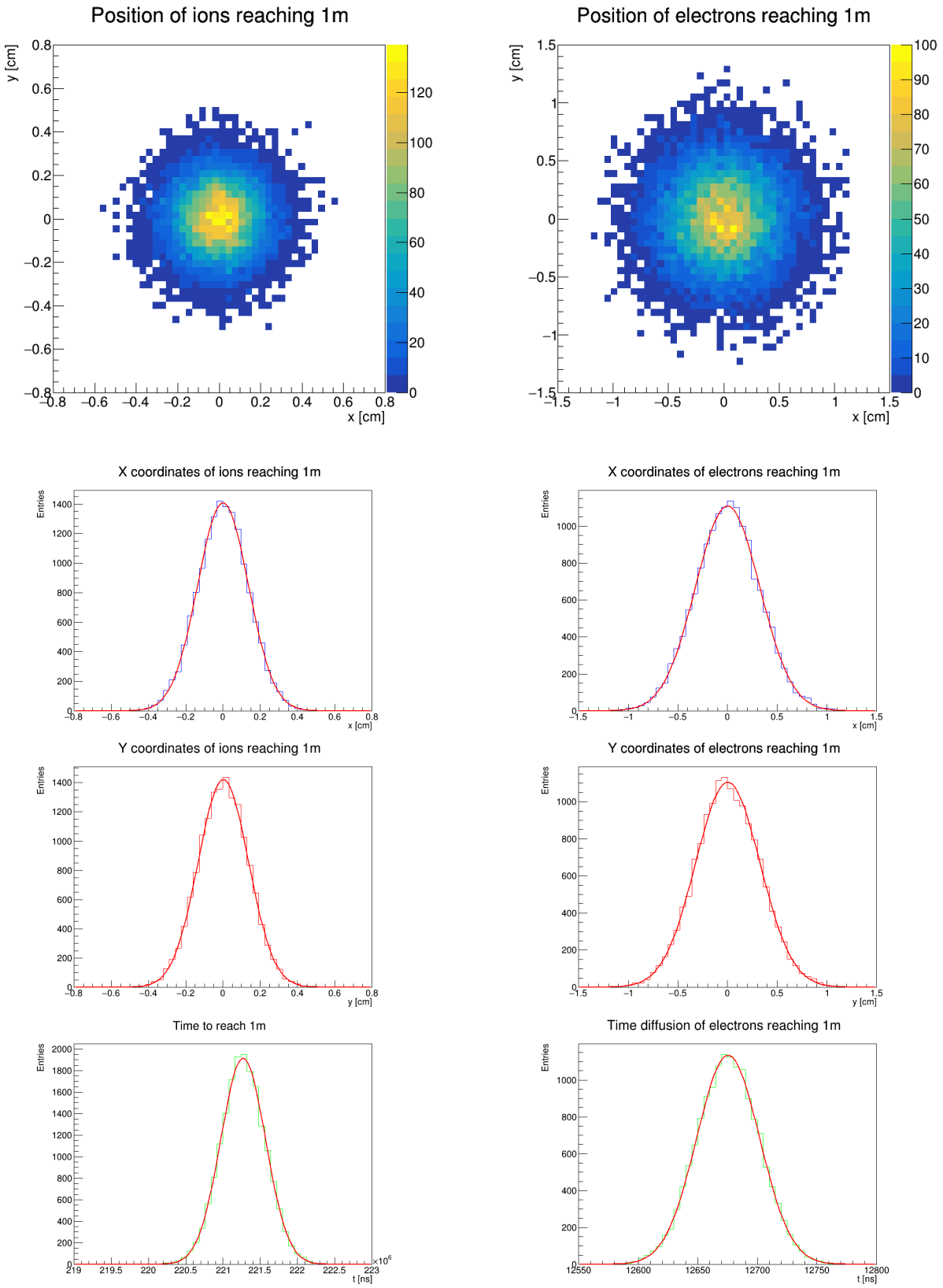


(a) (b)

Figure 4.15: *1 m diffusion results for ∼18000 ions (4.15a) and 15000 electrons (4.15b). The simulation was run having $E = 275\ V/cm$. The transverse spread of the electrons is about 150 times the height of the mesh in the micromegas.*

## 4.4 DMM simulations

The double micro-mesh detector is an original detector thought to isolate the electron-induced component of the induced signal from the ion-induced one. It has a THGEM-like structure that incorporates two mesh layers inside of it, meaning that its holes are split into three distinct sections which can be set to have different electric field intensities. This structure is directly placed on top of the anode and it has no bottom copper layer. The detector will be referred to as Double Mesh Micromegas (DMM) from here on. The DMM used in the experimental setup in *Chapter 5* has the same structure.
The unique structure of this detector is the result of an attempt to separate the electron component from the ion component of the induced signal. Indeed, this detector can apply an intense electric field triggering the multiplication process only between the two meshes, so that the signal that the ions would induce on the anode are screened by the lower mesh. Since only electrons are present in the layer right above the anode, the ion

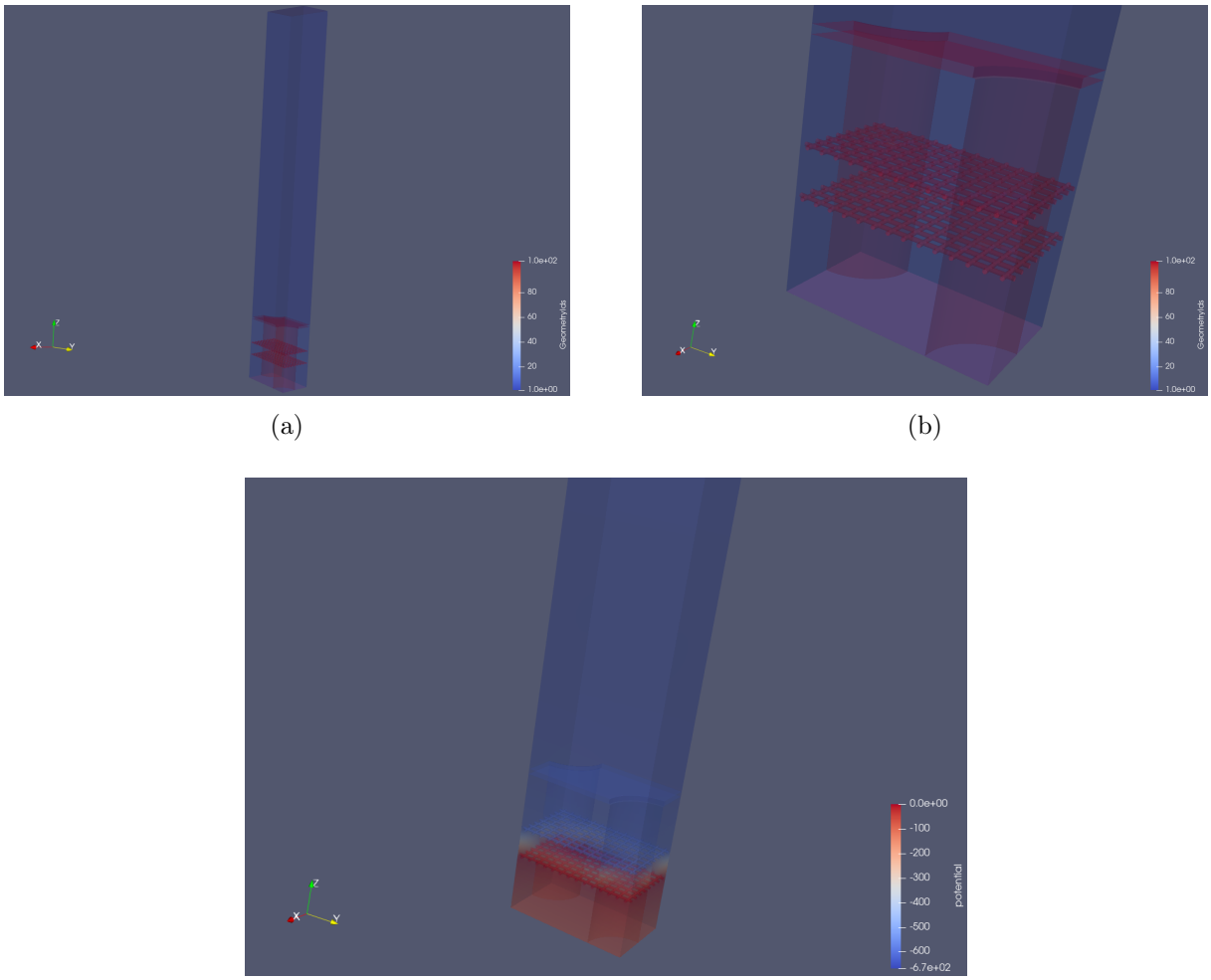


(a) (b)

(c)

Figure 4.16: *Full (4.16a) and detailed (4.16b) view of a single DMM cell with a sample field map (4.16c).*

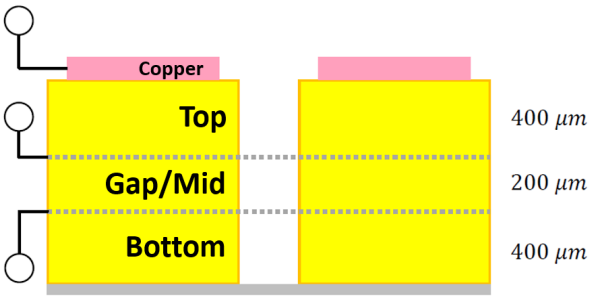


Figure 4.17: *Scheme showing the inner structure of the DMM detector.*

tail of the induced signal would be suppressed because of the screening and a distinct signal caused almost entirely by electrons would be generated.
The geometry of the detector is more complex than a simple micromegas. Similarly to the previous case, the geometric model was obtained looping a single cell along both the $x$ and $y$ axis directions. However in this case the cell is flipped at every step, meaning that each cell is surrounded in all directions by its mirrored copy. This results in the formation the typical GEM hole pattern which finds the six closest holes of each hole on an hexagonal shape. The holes have a diameter of 0.5 $mm$ each and the their pitch is equal to 1 $mm$. Each one of them has a 10 $\mu m$ rim without the top copper layer. Dissecting the model once again from top to bottom, it can be split into the drift volume and the DMM body, which can be further split into its internal layers.

- The drift volume was set to be 5 $mm$ high as it was its original experimental plan. Similarly to the micromegas case, electrons were usually released few tens of $\mu m$ below the upper cathode surface of the cell to avoid the electrons to go out of bounds backflowing to the cathode.
- The copper layer is the first layer of the DMM body facing the drift volume. It is 35 $\mu m$ thick and it collects most of the electrons that do not enter any of the holes. The hole rims do not have this layer.
- The three lower layers and the inner sides of the holes are entirely made of G10 fiberglass and they have a total thickness of 1 $mm$.
- The first mesh separates the first 0.4 $mm$ thick fiberglass layer from the lower ones. The mesh structure is identical to the one used in the micromegas simulation, having a pitch of 63 $\mu m$ and an approximated structure made of intersecting cylinders.
- The second mesh is located 0.2 $mm$ below the first one, and it has exactly the same attributes as the other one. It separates the upper layers from the last fiberglass layer which is directly placed on the anode pads and is 0.4 $mm$ thick.

The electrodes of this simulated detector are the top cathode surface, the copper layer (commonly referred to as "top layer"), the two meshes and the bottom anode surface. Consequently, the gas medium can be roughly divided into 4 sections potentially having

| Layer | Thickness ($z$ axis) | Cumulative height |
|---|---|---|
| Drift volume | 5 $mm$ | 6.035 $mm$ |
| Copper layer | 35 $\mu m$ | 1.035 $mm$ |
| Fiberglass "top" | 400 $\mu m$ | 1 $mm$ |
| Upper Mesh | | |
| Fiberglass "gap/mid-mesh" | 200 $\mu m$ | 600 $\mu m$ |
| Lower Mesh | | |
| Fiberglass "bottom" | 400 $\mu m$ | 400 $\mu m$ |

Table 4.2: *Summary of the layers along the vertical axis composing the DMM geometric model. The two meshes are sandwiched between the fiberglass layers and they do not additional thickness to the structure.*

different electric field intensities: "drift" ($\sim$5 $mm$), "top" (0.4 $mm$), "amplification gap" or "mid-mesh" (0.2 $mm$) and "bottom" (0.4 $mm$).

### 4.4.1 Field map and sample event

*Figure 4.18* shows the field map in the simulated DMM detector in a sample field configuration. Because of the little knowledge of the detector and the larger number of available field combinations, a larger number of field intensities was tested compared to the micromegas simulations, where the fields were almost fixed except for the transparency studies in *Section 4.3.5*.
Having 4 different field intensity regions implies 3 different transition zones and correspondingly 3 different transparency factors that enter the scene: the funnel at the entrance of the hole and the two meshes. Setting an optimal field configuration that takes into account all the requirements such as transparencies and gains at the same time is much more difficult compared to the micromegas case. The field maps that were mainly studied can be roughly divided in two categories: the ones having the dominant multiplication process in the 200 $\mu m$ gap region (mid-mesh amplification) and the ones having it in the last 400 $\mu m$ bottom gap (bottom gap amplification). The two configurations differ in the impact that the ions have on the signal current induced on the readout anode. A detailed analysis on the signals will be covered in *Section 4.4.5*.
*Figure 4.20* displays the number of electrons in 20000 independent avalanche events that reach each layer inside the detector in a mid-mesh configuration detector. The number of electrons in the upper layers of the detector is 1 in most of the events until the amplification gap is reached, where the electrons start the avalanche process and the size of the avalanche follows a Polya distribution. The number of entries gradually decreases as some of the electrons get captured by the detector or by gas molecules before starting multi-

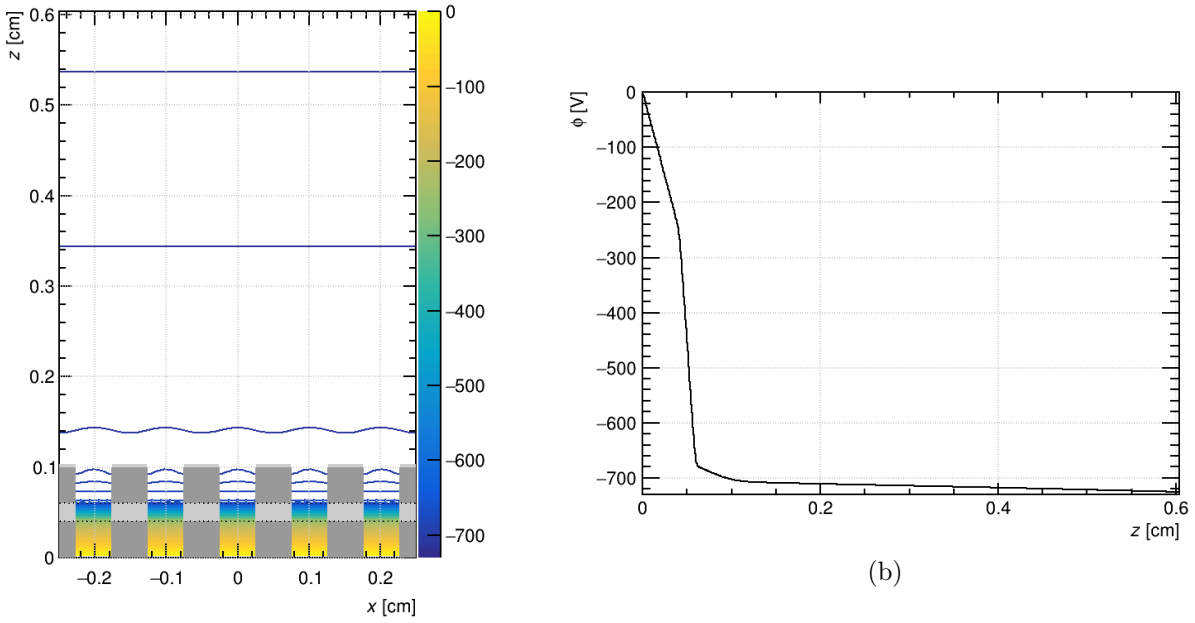


(a) (b)

Figure 4.18: *Plot of equipotential lines in the simulated DMM detector (4.18a) and plot of the potential profile moving along $z$ at $x, y = 0$ (4.18b). The side section of the mesh is visible in light gray in the left plot. The potentials are set such that $E_{drift} = 35\ V/cm$, $E_{top} = 700\ V/cm$, $E_{drift} = 22000\ V/cm$, $E_{bottom} = 6000\ V/cm$.*

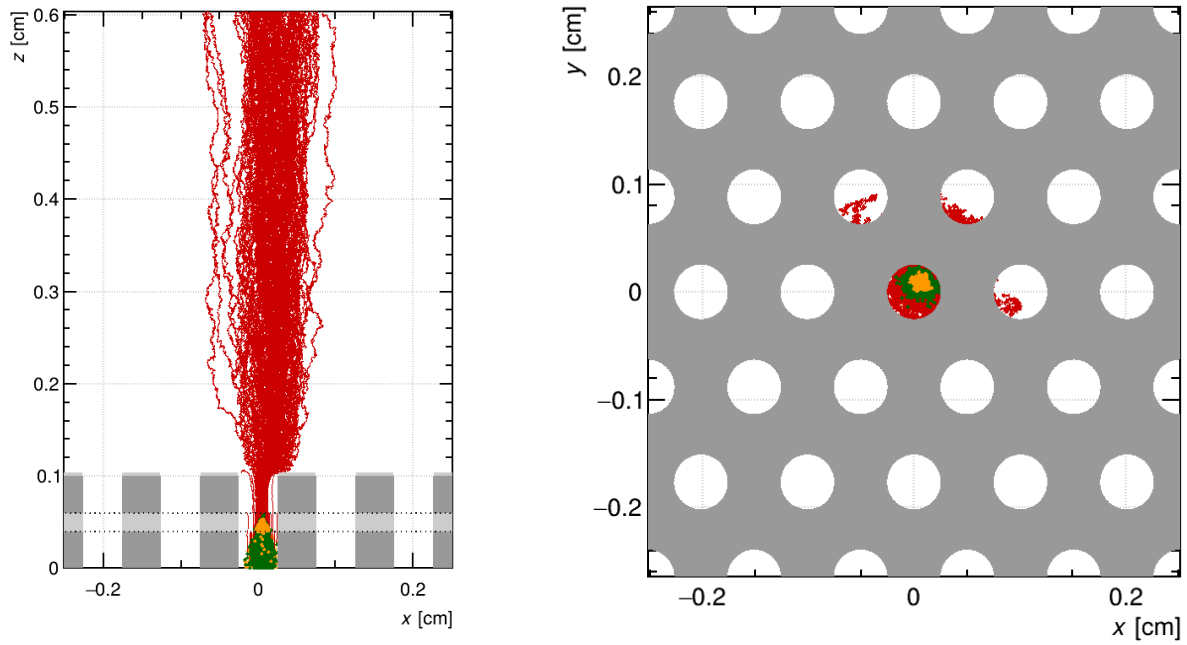


(a) (b)

Figure 4.19: *Sample avalanche event in the field configuration shown in Figure 4.18 from the side (4.19a) and from the bottom (4.19b). Orange tracks are the electrons, red tracks are the ions and green dots are the ionization points.*

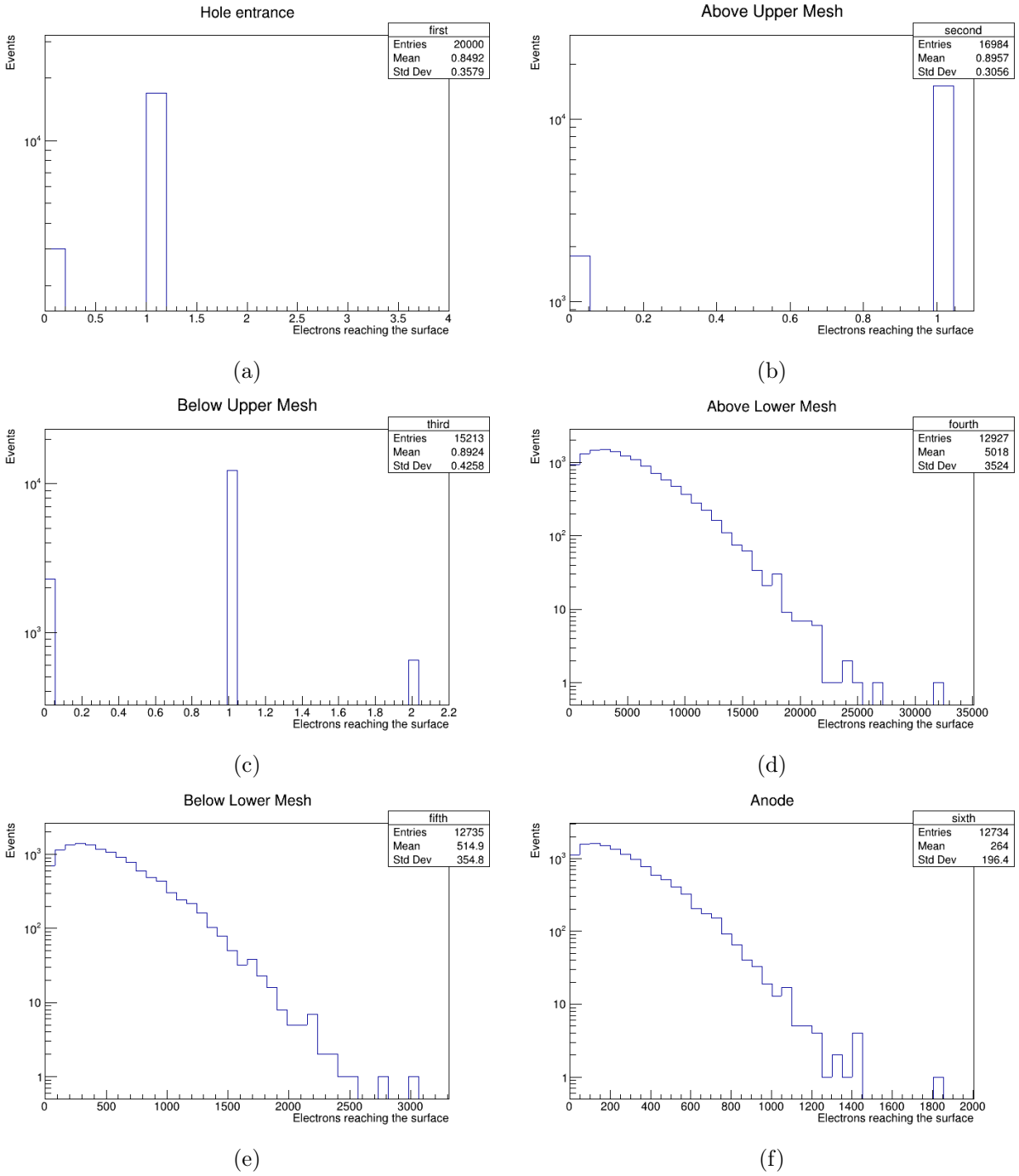


Figure 4.20: *Distribution of the number of surviving electrons inside the detector at the entrance of the hole (4.20a), right above (4.20b) and below (4.20c) the upper mesh, right above (4.20d) and below (4.20e) the lower mesh and at the anode (4.20f) for 20000 independent events in a mid-mesh configuration detector. The simulations were run with* $E_{drift} = 35\ V/cm$, $E_{top} = 700\ V/cm$, $E_{gap} = 22000\ V/cm$ *and* $E_{bottom} = 6000\ V/cm$ *with a nominal total gain of* $\sim 550$.

plication. It also must be stressed that these histograms only count the electrons that do reach a certain depth in the detector, and that they do not count the few electrons that move inside the detector and are captured before reaching the detection surface. This is a fundamental point that must be reminded when studying signal induction, as a charge moving near an electrode is enough to induce a current on it and these charges that do not make it to the the electrode also contribute to the formation of the readout signal. This is particularly relevant for the electrons in the bottom layer of the detector, since there are no screening layers and it is the region affecting the signal the most.

### 4.4.2 Drift-top funnel transparency

As in the micromegas mesh case, the shape of the field lines affects the number of electrons that enter the holes from the drift volumes without stopping on the copper surface of the DMM. Such lines are once again defined by the ratio between the electric fields inside and outside the hole, namely $E_{top}$, determined by the voltage difference between the upper mesh and the copper layer, and $E_{drift}$, determined by the copper surface and the cathode. It must be stressed that considered the diameter and the depth of the hole, the approximation of the electrodes to a parallel planes configuration is quite limited in

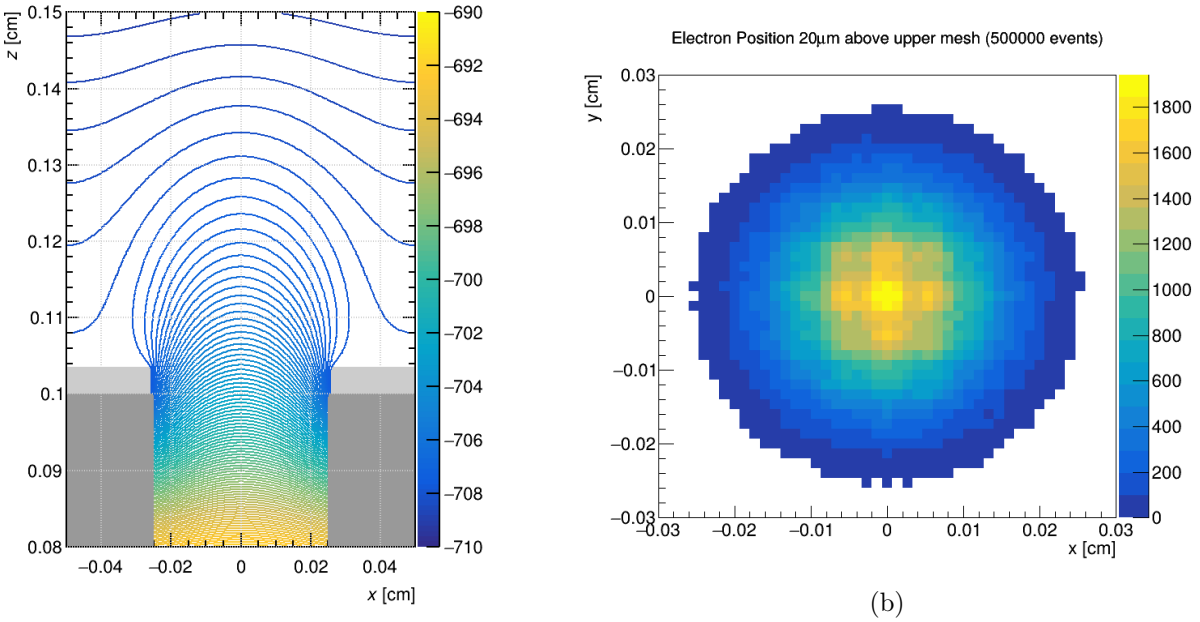


(a) (b)

Figure 4.21: *Equipotential lines of the field at the hole entrance funnel of the DMM (4.21a) and position of the electrons 20 µm above the upper mesh (4.21b). The electric field is slightly less intense at the center of the hole compared to the edges and the field lines converge towards the center, causing causes the convergence of the electrons in the center of the hole. The nominal field intensities are* $E_{drift} = 35\ V/cm$, $E_{top} = 700\ V/cm$.

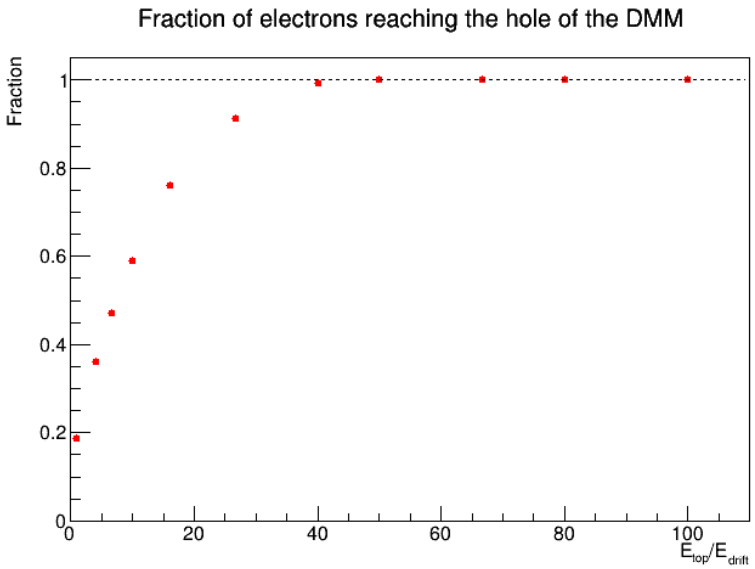


Figure 4.22: *Transparency of the electrons entering the hole depending on the ratio between the fields inside and outside the hole. $E_{top}$ is fixed to 800 $V/cm$ and $E_{drift}$ is changed to vary the ratio.*

this layer, and $E = \Delta V/\Delta z$ only gives a rough value of the field intensity in it. *Figure 4.21a* displays the deformation of the equipotential lines at the entrance of the hole, which follow in a less intense electric field at the center of the hole. It's also interesting to note that the shape of the equipotential lines imply a convergence of the field lines, therefore of the electrons towards the center of the hole. This means that at a later stage, near the amplification gap, the electrons and the subsequent avalanches would mostly gather in the center of the hole as shown in *Figure 4.21b*, and that the loss of electrons during the multiplication process due to wall capture will have a minor effect on the gain.
*Figure 4.22* displays the electron transparency of the funnel as the ratio between the two field changes. The electric field right on top of the upper mesh is fixed to 800 $V/cm$, while the field in the drift volume is variable and determines the value of the ratio between the two fields. The obtained result is similar to the one given by the micromegas mesh, as the fraction of surviving electrons rises quickly, exceeding 0.9 at a ratio $\approx 30$. This means that in a rough global transparency calculation this funnel can be almost considered as a mesh that has a slightly higher transparency.

### 4.4.3 Mesh transparencies

The two meshes in the detector are the other two electron transition bottlenecks. The geometric structure of the mesh itself is equal to the one used in the micromegas detector, so at first glance the transparency of the electrons is expected to be quite similar to the former case. However, this setup is quite different from the previous one and the involved variables are not the same in the two cases.

Firstly, the lower mesh potentially has an avalanche-inducing intense electric field not just below but also above it, thus the reciprocal dependence among the electrons in an avalanche must be taken into account as it may impact on the transparency of the mesh. Furthermore, the presence of a limit in the spatial coordinates along the two transversal directions differently from the micromegas setup is an issue that must be covered. Indeed, in the DMM setup an electron entering the hole might be caught from the inner walls of the DMM holes and never reach the mesh below, while electrons in a micromegas did not have such limitation[8]. Though this could potentially affect the number of electrons reaching the meshes and the multiplication gain of the avalanches occurring in the amplification region, the effect of this phenomenon is limited by another factor that differs from the micromegas setup: the electrons do not reach the mesh evenly distributed in this detector, but they are rather gathered in the center of the hole as shown in *Figure 4.21b*. Applying few changes to the premises used in the micromegas simulation is hence convenient in order to have a more practical and accurate estimate of the number of electrons in the various layers in the hole. In the case of the upper mesh it's useful to define an "effective transparency" that also takes into account the electrons lost in the walls of the top fiberglass layer, defined as the number of the electrons that cross the considered mesh over the number of electrons that entered the hole. As for the transparency of the lower mesh in the mid-mesh amplification configuration, it should be studied using electrons that are product of an avalanche process in a more intense electric field.
*Figure 4.23* displays the electron transparency of the upper mesh depending on the ratio $R$ between the fields on the two sides of the mesh. The electric field right in the amplification gap is fixed to 25 $kV/cm$, while the field in the top layer is variable and determines the value of the ratio between the two fields. The plot shows the previously defined effective transparency of the upper mesh and the standard transparency computed as the number of electrons making it through over the electrons reaching the height at the top of the mesh. The overall trend of the data matches the results attained in *Section 4.3.5* for the micromegas transparency: a rapid increase of the transparency as the ratio increases followed by a stabilization of its value in proximity of $R \approx 40$.
As expected the effective transparency is slightly lower than the transparency computed only considering the mesh effects, since a larger fraction of the considered electrons are lost in a longer path. In particular, for this case it is possible to see that the relative difference between the two datasets is much larger at smaller ratio values. This comes from the fact that the data at lower ratios have a higher electric field intensity above the mesh and allow a large number of electron attachment events, differently from the data at high ratios where the wall capture of the electrons is the main reason of the difference between the two datasets. Therefore this effect is a consequence of the intensity of the

[8]The main spatial constraint affecting the motion of the electrons in a bulk micromegas detector is due to the pillars supporting the mesh on the anode planes. However these pillars are point-like spots that are generically spaced between them by a distance of $\sim cm$. Considering the height of the mesh above the anode plane, this constraint is less relevant compared to the DMM detector.

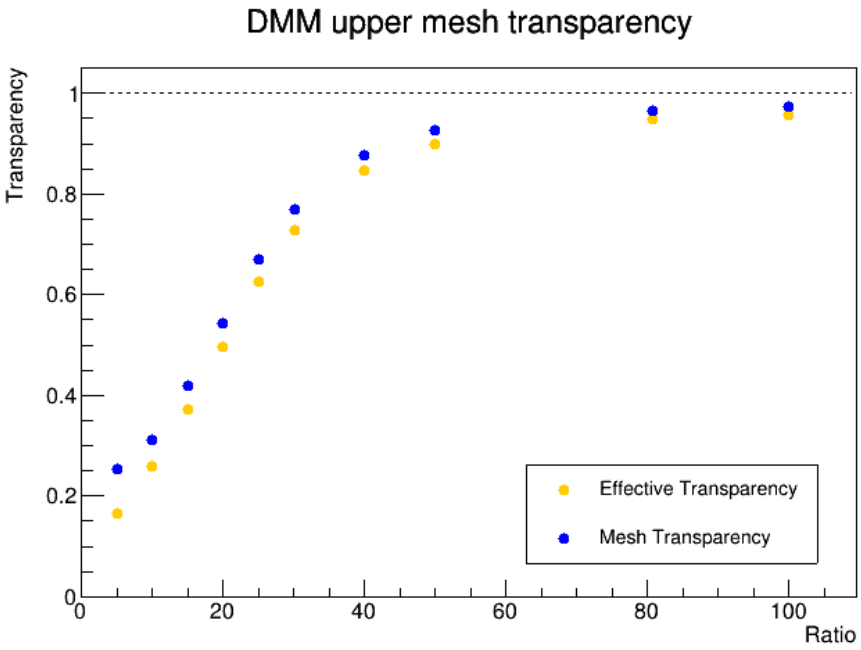


Figure 4.23: *Transparency of the electrons crossing the upper mesh depending on the ratio between the fields above and below the mesh. $E_{gap}$ is fixed to 25000 V/cm and $E_{drift}$ is changed to vary the ratio, 50000 events for each sample. The orange points show the effective transparency that include all the effects occurring between the hole entrance and the mesh such as wall capture, while the blue ones are the result derived considering only the mesh-crossing section.*

electric field and not of the ratio between the two fields. This is an example of an effect that highlights the deep correlation between some of the multiple variables that influence the transparency of the mesh.

*Figure 4.24* displays the electron transparency of the lower mesh depending on the electric field on the two sides of the mesh in the two amplification configurations at practical field values. The electric field right in the amplification gap is fixed to 12.5 $kV/cm$ in the bottom configuration and to 24 $kV/cm$ in the mid-mesh configuration, while the field in the bottom layer is variable and determines the value of the ratio between the two fields. The choice of the fields in the bottom configuration that has similar field intensities in the two lowest layers derives from a set of problems in the standard bottom configuration that involve the excess of transparency layers in the detector and the limited freedom in the choice of the field intensities which will be explained more in detail in *Section 4.4.5*. As the assumptions have changed, it is clearly visible that the transparency values are different from the results obtained in the simple micromegas setup. The bottom amplification configuration, that is characterized by a ratio $R = E_{bottom}/E_{gap}$ between 0.9 and 1.1, returns a transparency value of $\approx 0.2$, and the mid-mesh configuration, having $R$ between 0.2 and 0.5, returns a value ranging from 0.07 to 0.14. In both cases the obtained results are about twice the values obtained using the single mesh. This difference comes from the fact that the electron transparency of a mesh depends on many variables such as the intensity of the fields, the ratio between the fields on the two sides of the mesh,

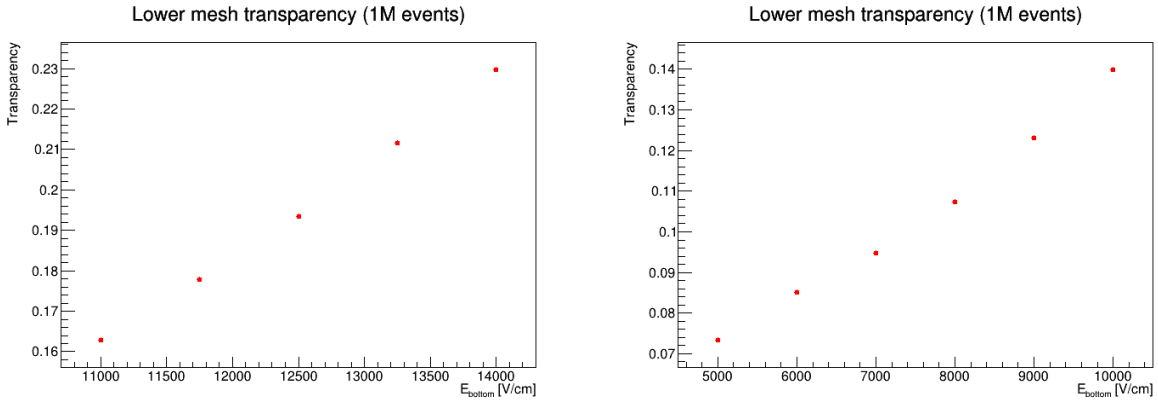


(a) (b)

Figure 4.24: *Transparency of the electrons crossing the lower mesh depending on the intensity of the field below the mesh at practical field intensities in bottom configuration (4.24a) and in mid-mesh configuration (4.24b). $E_{gap}$ is set to 12500 V/cm in the first case and to 24000 V/cm in the second one, therefore the ratio with $E_{bottom}$ ranges between 0.9 - 1.1 in the bottom configuration and 0.2 - 0.5 in the mid-mesh setup.*

the spatial distribution of the electrons reaching the mesh and the correlation between the incoming electrons. Therefore the precise estimate of the transparency is not a trivial issue and must be handled with care, considering the multiple factors that might affect it. For the purpose of this thesis, it is sufficient to have an estimate of it at field intensities that can be applied in a real setup. A computation was done in every necessary field configuration, and in most cases one electron makes it through out of 3 to 5 in the bottom configuration, while in a mid-mesh configuration the fraction of electrons reduces to one out of 7 to 15.

### 4.4.4 Multiplication gains

The DMM detector has three different layers inside the holes that can host three different electric field intensities. The two configurations of main interest are the ones that apply a high electric field that induces avalanches in the middle layer only and in the bottom layer only. The estimate of the mean gain of an avalanche in T2K gas for such height was obtained thanks to a separate parallel plates simulation having a gap distance of 200 $\mu m$ and 400 $\mu m$, which are respectively the heights of the mid-mesh and bottom layers. The results are shown in *Figure 4.25*.
Both datasets can be fit using an exponential function $f(x) = e^{Ax+B}$ as expected from *Equation 3.5*. As the multiplication length increases the gain does too, hence at longer multiplication length distances higher gains can be obtained with lower electric fields.
The computed gain values are the mean gain values of a Polya distribution which is a distribution that has a long tail, therefore a low mean gain does not exclude the possibility

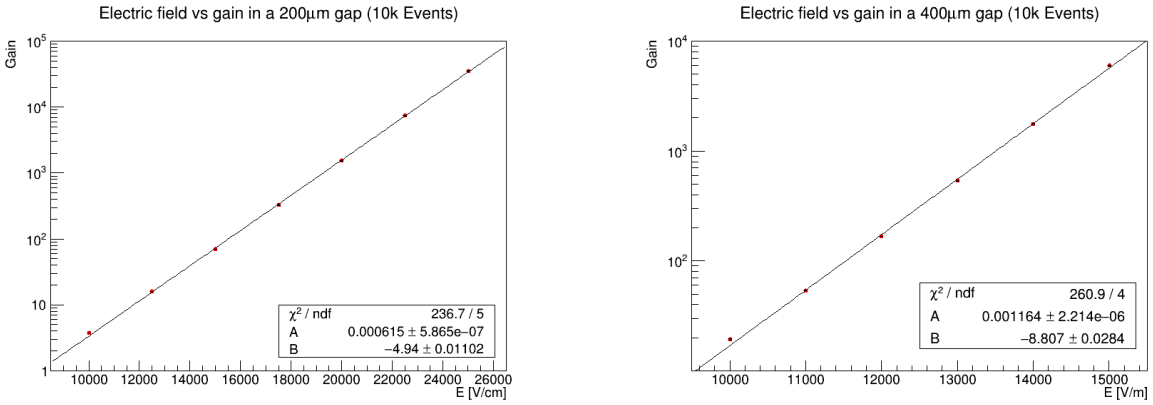


(a) (b)

Figure 4.25: *Relation between applied electric field and mean gain of electron avalanches in a parallel plate setup having a gap distance of 200 µm (4.25a) and 400 µm (4.25b).*

of having frequent avalanches that are larger and well above this gain value. Considering the mean gain of the Polya distribution $\bar{n}_e$ as in *Equation 3.6*, the events that have a gain below $5\bar{n}_e$ make up 99.95% of all the events in a Polya distribution. Therefore it is roughly possible to say that barely any electron starts the multiplication process for values of $\bar{n}_e$ such that $5\bar{n}_e \lesssim 1$ where $\bar{n}_e$ is the mathematical estimate of the mean gain obtained from the exponential fitting function. Following the exponential curves in both plots it is possible to compute that such value is obtained at an electric field intensity of about 6 $kV/cm$, below which the multiplication of electrons hence is a rare event in T2K gas in general.

Additionally, these results highlight an issue that have a non-negligible consequence on DMM detector simulations. Indeed, the objective of the detector is to reach approximately the same gain in the two detector configurations to compare the results with a similar gain. In a mid-mesh configuration the electrons multiply largely between the two meshes, but their number is reduced by a factor between 10-20 in the lower mesh crossing process. Considering realistic gain values trying to avoid sparks in the detector, the final number of electrons reaching the anode would be at most of few thousands. This puts a quite strict constraint on the intensity of the electric field in the bottom gap which should be around 15 $kV/cm$ at maximum. This adds up to the three transparency layers issue, as a relatively high ratio between the fields is required in all layers to be able to observe signals at a decent rate. These two factors imply that excessively prioritizing the ratio between the fields would lead to a low field in the drift region, which would cause the recombination the primary electrons with the ions in a real setup. On the other hand, putting the transparencies aside and increasing the field intensities is inefficient computationally as an excessive number of primary electrons does not make it to the amplification layers.

The choice of field intensities is therefore a delicate issue that is set as a compromise

between computational efficiency and likelihood to reality. However, as it will be better explained in *Section 4.4.5*, this problem can be partially solved allowing a weak multiplication between in the mid-mesh section, which basically reduces the number of transparency layers from three to two, gives more freedom in the choice of the electric fields in the upper layers and it has a limited impact on the final result. This problem is less evident in a real experimental setup, since a large number of primary ionization electrons, for instance from an $\alpha$ source, is barely affected by a reduction of transparency and can clear this issue.

### 4.4.5 Signal induction on the anode and ion signal suppression

The whole point of the design of this detector stands on its potential ability to suppress the ion component of the induced signal and isolate the electron-induced peak. To verify whether it works or not, simulations were run putting together the results obtained so far and choosing appropriate values for the electrode voltages.
As it was mentioned in *Section 4.4*, such result is achieved by comparing the signal induced in two different field configurations: the bottom gap amplification configuration, which generates avalanches only in the last gap right before the anode similarly to a micromegas setup, and the mid-mesh amplification configuration, which multiplies only in the layer between the two meshes. The ion tail induced in the mid-mesh configuration should theoretically be smaller than the bottom configuration, because most of the ions are generated in the upper layer and the signal induced on the anode by such ions is screened by the lower mesh.
*Figure 4.26* shows a typical event signal induced on the anode in the two configurations. The two configurations have their electrode voltages adjusted in order to have a similar final gain. It must be reminded that similarly to the micromegas case in *Section 4.3.6* the time scale involving the ion tail is not accurate because of the lack of information on the ion mobility.
Firstly, it is interesting to observe the shape of the ion tail signal and notice that it has a double-step structure, resembling the double-mesh structure of the detector. Indeed, comparing the position of the steps with the time values at which the ions were collected by the meshes, a step occurs when there are no longer drifting ions in one of the layers below the meshes in both cases. When this happens the signal drops and stabilizes at a lower value, because there are still ions drifting in the upper layers that induce a signal on the anode which is much weaker because of the mesh screenings. Moreover, the most relevant difference between the two signals is the position and the height of the first step. The difference in position is caused by the different velocity of the ions in the last gap, hence by the electric field intensity in the last gap, that affects the total collection time of the ions $t_{tot}$. The velocity affects the amplitude of the signal $i_{ionmax}$ indeed, but the other major cause of its variation is the screening effect of the lower mesh. In fact, considered

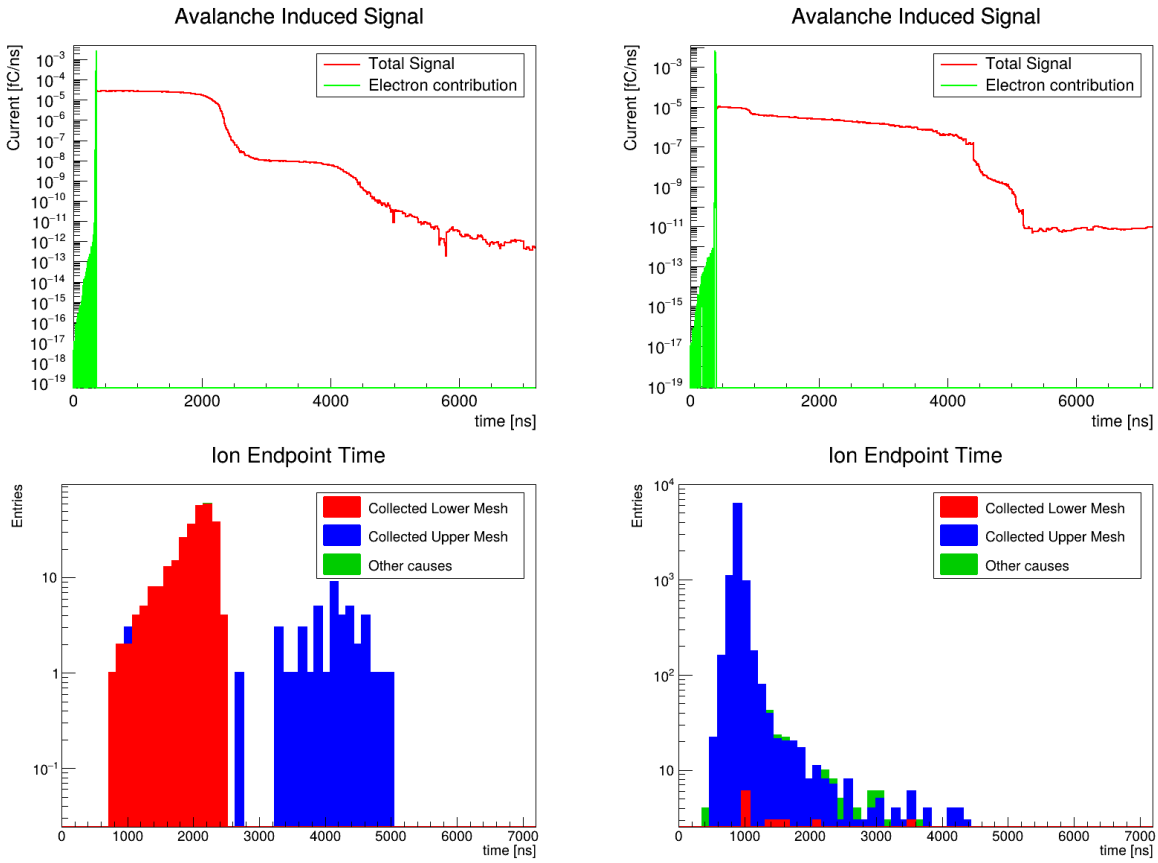


Figure 4.26: *Signal induced on the anode by an avalanche event in a bottom configuration (4.26a) and in a mid-mesh configuration (4.26b) with the corresponding spread of the timings the ions were recollected at. The simulations were run with* $E_{drift} = 35\ V/cm$, $E_{top} = 700\ V/cm$ *in both cases, then* $E_{gap} = 6000\ V/cm$ *and* $E_{bottom} = 13000\ V/cm$ *in the bottom case and* $E_{gap} = 22000\ V/cm$ *and* $E_{bottom} = 6000\ V/cm$ *in the mid-mesh case, with a nominal total gain of* $\sim 550$.

the intensity of the bottom fields used in these simulations, the expected $t_{tot}$ reduction and $i_{ionmax}$ increase factor would be roughly 2, proportionally to the electric fields. This number does indeed match with the simulations in the time case, as the total recollection time roughly doubled in the mid-mesh configuration ($t_{tot}^{mid} \approx 2t_{tot}^{bottom}$), which has the weaker field intensity in the bottom layer. But it will be shown that this is not true in the amplitude case.

*Figure 4.27* shows the cumulative signal, i.e. the charge induced on the anode over time, of the sample events in *Figure 4.26*. Both slopes can be divided in two sections: a first steep spike, induced by the electrons, and a gentler slope induced by the motion of the ions. The small contribution of the ion component in the mid-mesh configuration is an additional indicator that further confirms the suppression of the ion tail component of the signal.

To compare and quantify the signal magnitude difference between the two cases, it is help-

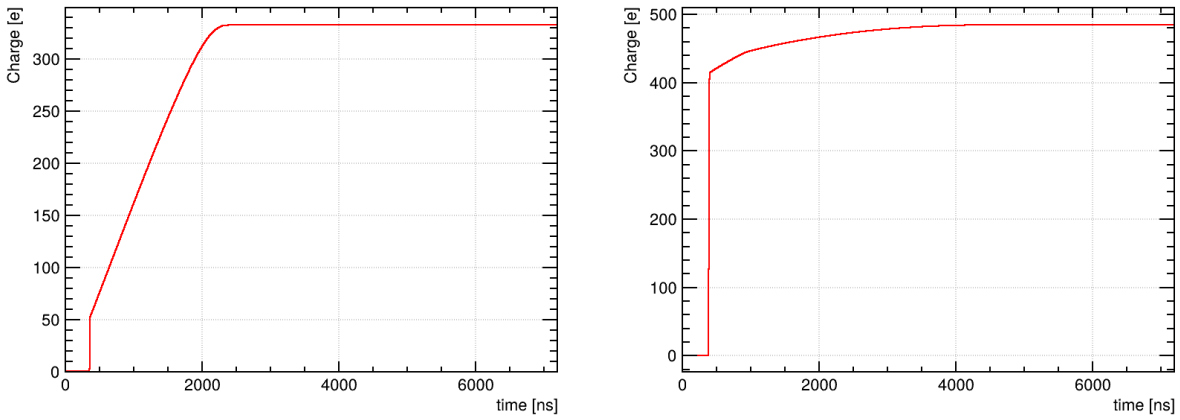


(a) (b)

Figure 4.27: *Cumulative signal of the events shown in Figure 4.26: bottom configuration (4.27a) and mid-mesh configuration (4.27b).*

ful to define a "signal ratio" quantity $R$, obtained from the ratio between the maximum amplitude value of the electron signal and the maximum amplitude value of the ion tail ($R = i_{emax}/i_{ionmax}$). Since the electrons are fast and the gains are set to be similar, $i_{emax}$ is approximately equal. In this situation the signal ratio can also be seen as an indicator of the ion tail suppression, and a high $R$ value would mean a large suppression of the ion tail. If the difference between the amplitudes of the ion tails were of a factor 2 as in the case of the ion recollection time, this would manifest as a variation of a factor 2 of $R$ between the two cases.

*Figure 4.28* displays the distribution of $R$ for multiple events in the two configurations used previously in *Figure 4.26*. In the bottom amplification case the mean signal ratio turns out to be $R \approx 90$, while in the mid-mesh amplification case it is much higher, at $R \approx 600$. The tail suppression factor $R_{mid}/R_{bottom}$ is much larger than the ratio between the field intensities in the bottom layer in the two cases. Indeed, $E_{bottom}$ is equal to 13 $kV/cm$ in the bottom configuration and 6 $kV/cm$ in the mid-mesh configuration, implying that if the intensity of the electric field was the only factor affecting the amplitude of the ion tail, the suppression factor should be $\approx 2$. However this is not true and it turns out to be $\approx 6.5$, meaning that the electric field on its own is not enough to explain such large suppression of the ion tail.

However these simulations focused more on computing efficiency and visibility and clarity of the results rather than its replicability on a real setup. The field intensities were set at a very low value, not only limiting the gain of the avalanche but also ignoring the fact that in a real detector the primary electron would recombine with the ion instead of drifting if the electric field is too weak. Additionally, the triple transparency bottleneck mentioned in the previous sections must be kept in mind to be able to see avalanche events at an efficient rate. So further simulations were run to demonstrate that the suppression of the

ion tail is indeed effective in such situations, setting the voltages at values which satisfy these constraints and improve the reliability of the simulations:

- The bottom gap amplification configuration was slightly modified allowing a very small amplification in the mid-mesh region too. This does reduce the transparency layers from 3 to 2, allowing more freedom in the choice of the electrode voltages and increasing the rate of successful multiplication events without affecting the signal ratio since most of the ions are still generated in the bottom layer.
- The drift field was increased to an intensity of 100 $V/cm$ which does indeed drift the electrons without having them recombining with the ions.
- The multiplication field intensities were increased in both cases to reach a higher gain value of about $\sim 1500$.

The results are summarized in *Figure 4.29* and in *Table 4.3*, demonstrating that the previous conclusions are hardly affected by these changes. Comparing the obtained $R$ values with the value obtained in micromegas simulations in *Section 4.3.6*, the bottom configuration has an $R$ value on the same order of magnitude. However it is clear that its value in a DMM in mid-mesh configuration is much higher, meaning that the amplitude of the ion-induced signal current is much more suppressed.
In summary, this result confirms that in principle the detector is indeed able to suppress the ion tail component of the signal induced on the anode by a factor $\approx 8$ compared to a simple micromegas detector operating at a similar gain value.

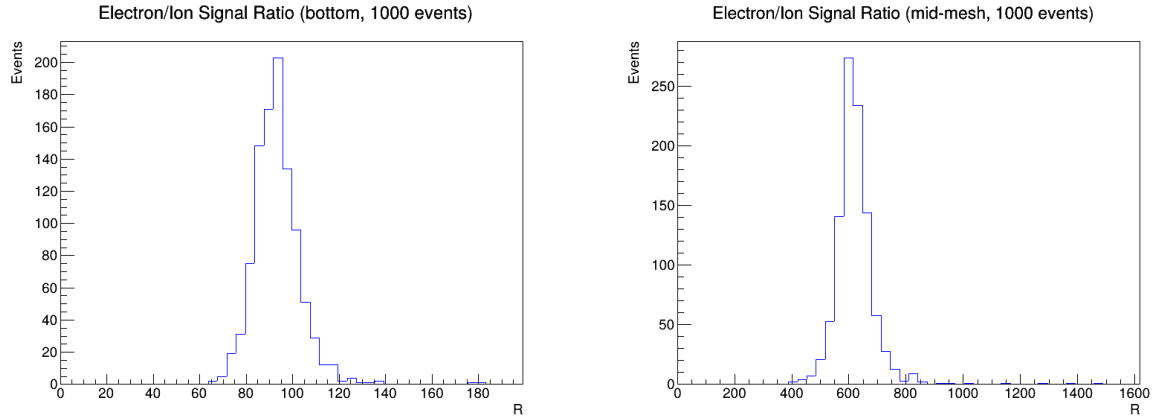


(a) (b)

Figure 4.28: *Histogram of the distribution of the signal ratio of 1000 avalanche events in the bottom gap amplification configuration (4.28a) and in the mid-mesh amplification configuration (4.28b). The simulations were run with $E_{drift} = 35\ V/cm$, $E_{top} = 700\ V/cm$ in both cases, then $E_{gap} = 6000\ V/cm$ and $E_{bottom} = 13000\ V/cm$ in the bottom case and $E_{gap} = 22000\ V/cm$ and $E_{bottom} = 6000\ V/cm$ in the mid-mesh case, with a nominal total gain of $\sim 550$. Only avalanches having at least 1 electron reaching the anode were considered.*

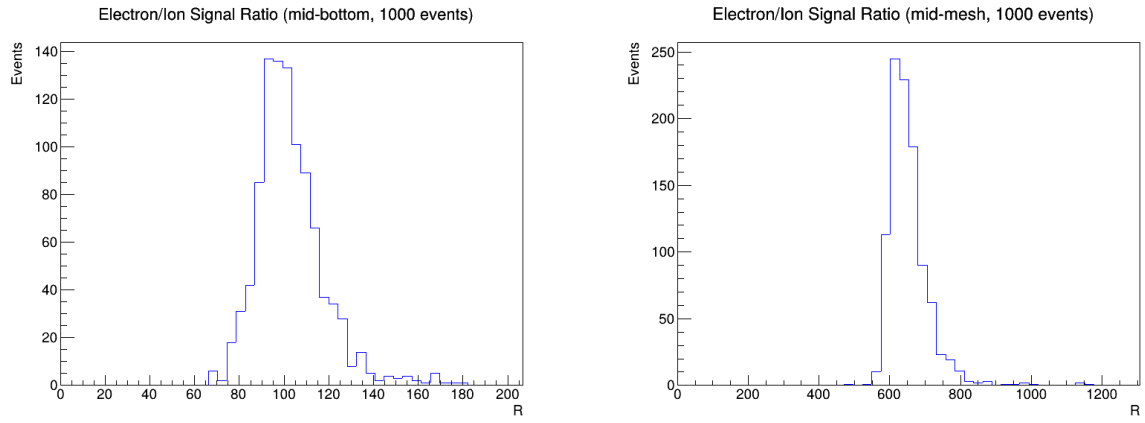


(a) (b)

Figure 4.29: *Histogram of the distribution of the signal ratio of 1000 avalanche events in the bottom gap amplification configuration (4.29a) and in the mid-mesh amplification configuration (4.29b). The simulations were run with $E_{drift}$ = 100 V/cm, $E_{top}$ = 1250 V/cm in both cases, then $E_{gap}$ = 12750 V/cm and $E_{bottom}$ = 12750 V/cm in the bottom case and $E_{gap}$ = 24000 V/cm and $E_{bottom}$ = 6000 V/cm in the mid-mesh case, with a nominal total gain of ∼ 1500. Only avalanches having at least 1 electron reaching the anode were considered.*

| | $R$ | $/R_{MM}$ | $/R_{bottom}$ |
|---|---|---|---|
| Micromegas | (75 ± 8) | 1 | |
| DMM (bottom) | (99 ± 10) | (1.3 ± 0.2) | 1 |
| DMM (mid-mesh) | (634 ± 30) | (8 ± 1) | (6.4 ± 0.7) |

Table 4.3: *Table summarizing and comparing the R values of DMM simulations and MM simulations in Section 4.3. The DMM in mid-mesh configuration can suppress the ion tail amplitude by a factor ≈ 6.5 compared to the bottom configuration and by a factor ≈ 8 compared to a micromegas detector.*

# Chapter 5

# DMM studies on a real setup

The second section of this study is centered around the assembly and testing of a DMM in a real experimental setup. The main goal of this part of the thesis is the study of the response of the detector when subject to ionizing particles and the observation of the ion tail suppression discussed in *Section 4.4.5*. This also implies gaining in the process a better understanding of a novel detector and of the real problems that affect its operation.

## 5.1 Experimental setup

The DMM detector was first produced and put together in a preliminary setup at CERN between September and December 2024, where basic tests were run to get to know the detector better. In February 2025 the detector was then moved to LNL, where the DMM was incorporated in a definitive setup. Several components were tested and changed in the process, but this section will focus on the configuration that actually did take data.

### 5.1.1 Chamber structure

The internal volume of the gaseous chamber is about 15.0×15.0×1.0 $cm^3$ large. It is mounted on PCB board that embeds the readout pads of the detector, a connector which sends the signal received from the pads to the Front-End Electronics (FEE) and few electrodes that connect the inner side of the chamber to the outside and supply the required voltages to the electrodes of the detector. The readout plane is made of 120 rectangular pads arranged in a 12×10 configuration that shape a square active surface of 10×10 $cm^2$. Each pad is electrically connected to the pins of a Panasonic 130-pin connector. The connector is interfaced to the FEE via a custom-made mezzanine PCB mounted on the connector itself. The mezzanine PCB has only passive elements and allows the analogical activation and deactivation of each pad of the detector by grounding the

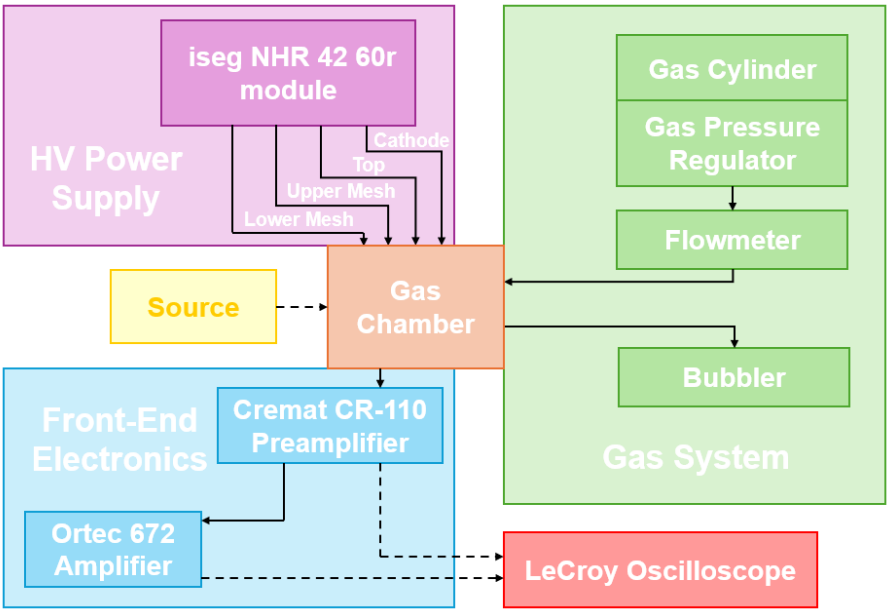


Figure 5.1: *Scheme of the various components of the experimental setup.*

inactive channels through a mechanism made of pins and jumpers. This allows a custom selection of the number and position of the active pads in the detector. The volume of the chamber is defined by a 1 *cm* high fiberglass frame hosting a copper-laminated cover on top of it. The frame features two openings on its sides serving as the input and output of the gas circulating in the chamber, a groove on its top and one on its bottom to accommodate two O-rings that keep the chamber gas-tight. The structure is mechanically kept together by a system of screws and nuts. The cover has a window right on top of the detector bulk, to allow the introduction of source-generated ionizing radiation in the detector. Multiple windows of different materials were made to optimize the transparency of the ionizing particles depending on the source nature: a Kapton one to let in the Fe-55 X-rays, a fused silica one for the UV photons and the most used mylar one for the Am-241 $\alpha$ particles.

The DMM board is placed right on top of the pads and is kept in position by four screws made of plastic material fixed to the board, that serve as a guide of the structures above. The cathode is a metal mesh glued on a fiberglass frame placed at a variable height between 5 to 8 *mm* on top of a stack of spacers above the DMM. The data collected in this work was taken having the cathode at a height of 6 *mm*. The top copper layer of the DMM, usually simply called "top", is segmented in six sections which are made to be electrically independent between them. This detail prevents potential damages in case of discharge in the detector by limiting the discharge magnitude and the affected area. In practice the six sections were connected between them by means of high resistances, making it possible to supply all the top electrodes to the same voltage while limiting such discharge effects as in the original situation. Additionally each section has a different number of holes, enabling the study of the effects of the presence or absence of holes close

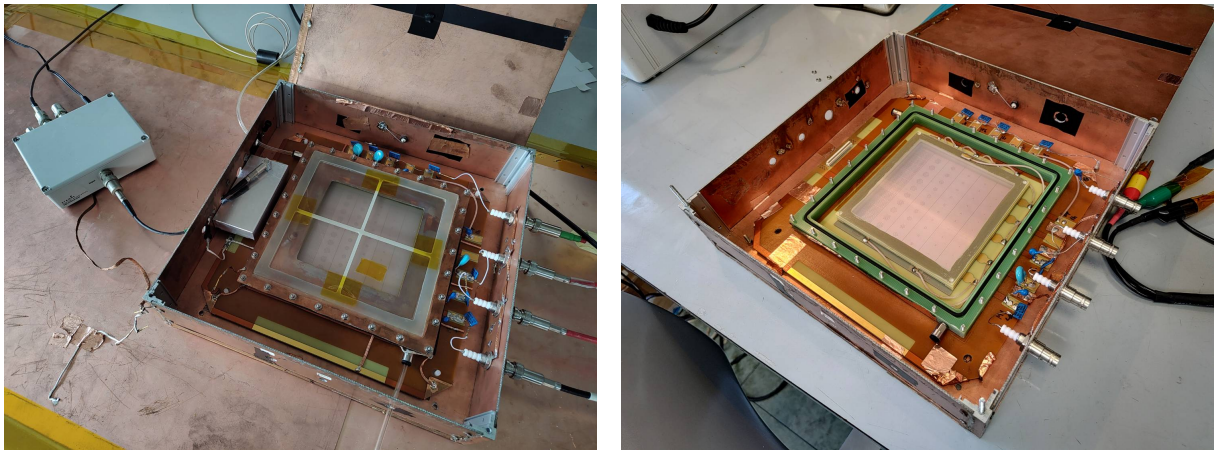

(a) (b)

Figure 5.2: *Picture of the whole gas chamber with a mylar window (5.2a) and without the cover (5.2b).*

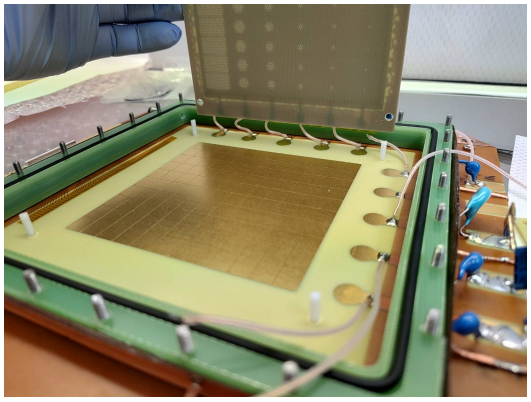

Figure 5.3: *Picture of the anode pads of the gas chamber.*

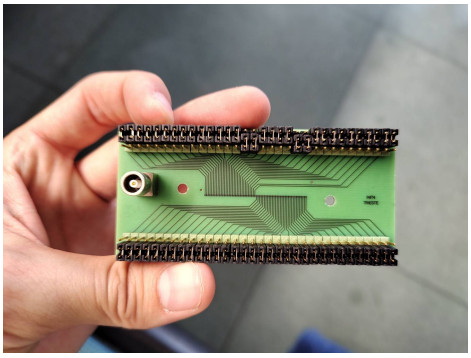

Figure 5.4: *Internal structure of the readout connector that allows to choose which pads to activate using a system made with pins and jumpers. The picture shows a configuration with 4 active pads.*

to the main one. The entire detector is contained in a grounded box made of copper which acts as an electrical shielding from the perturbations coming from outside.

### 5.1.2 Gas system

The detector mainly used T2K gas mixture during its operation, but eventually some tests were run using an 85:15 mixture of Ar-$CO_2$. Both gases were already premixed and stored in cylinders. The chamber is preceded by a flowmeter that regulates the ingoing flux of gas coming from such cylinders. The exhaust of the detector leads to a bubbler filled with paraffin that sets the pressure of the gas inside the chamber. The overpressure depends on the material of the window in use and its fragility, but generally it is set at

few *mbar* above the atmospheric pressure to contain air leaks inside the detector. It must be stressed that the fragility of the window is not a negligible factor in the operation of the detector, and setting an excessive gas pressure or flux might lead to damages such as leaks through the window.

### 5.1.3 Front-End Electronics

The signal is read out and processed by the Front-End Electronics (FEE) section of the setup, which includes a Cremat CR-110 charge sensitive preamplifier followed by an Ortec 672 Spectroscopy amplifier. This setting focuses on the identification of the signals and is able to integrate them over a long shaping time ($\sim \mu s$) suppressing the noise while amplifying the signal. As a consequence the signal-to-noise ratio of the waveform is quite large and the output signal is quite easy to identify, but it loses information on its time structure as a drawback.
The setup is made in a way such that it allows a smooth switch to a different FEE configuration. This also makes available the option of using a broadband fast amplifier, which can maintain the time profile of the original signal coming from the detector. However this setup is more challenging since it is more difficult to spot the signal pulse because of the lower signal-to-noise ratio.
The setup is usually used with an Aim-TTi TGF4242 Pulse Generator, which is able to send in the FEE a known signal. This device plays an fundamental role in the calibration

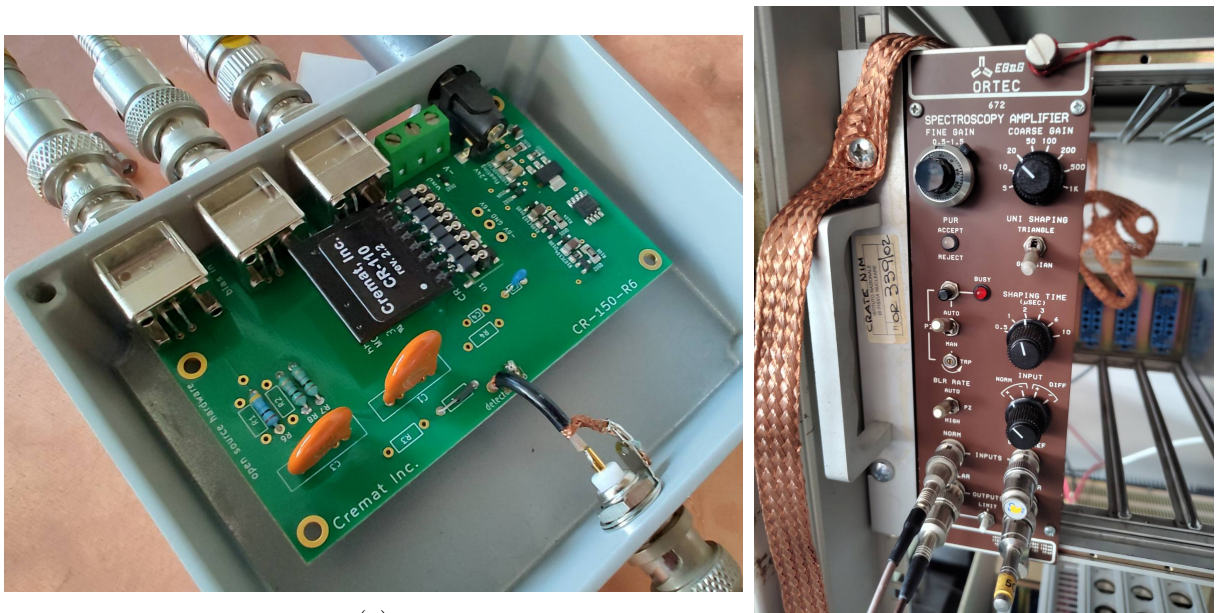


(a) (b)

Figure 5.5: *Cremat CR-110 charge sensitive preamplifier (5.5a) and Ortec 672 Spectroscopy amplifier (5.5b).*


(a) (b)

Figure 5.6: *Picture of the Aim-TTi TGF4242 Pulse Generator (5.6a) and LeCroy Waverunner 640Zi oscilloscope. (5.6b).*

of the amplitude of the signal. Indeed, the pulser makes possible the option of giving an estimate of the total charge collected by an event, as it can send in the FEE pulses with a known charge value by passing them through a known entrance capacity.
The signal processed by the front-end electronics can be used for multiple purposes and analyzed with several different methods. The main approach of this work consists in the use of an oscilloscope to carry out analyses directly on signal waveforms. The data was observed and collected by a LeCroy WaveRunner 640Zi oscilloscope, featuring 4 input channels, $4GHz$ bandwidth and a sampling rate of 40 $GS/s$.

### 5.1.4 DC Power supply

Considering that in most cases the pads are grounded, the detector has four electrodes to supply at different voltages: the cathode, the "top" copper layer on the DMM and the two meshes inside of it. They are all supplied a high voltage by the four channels of an iseg NHR 42 60r module. The voltages used in laboratory never exceeded 3 $kV$, but this module could potentially supply up to 6 $kV$. Each supply channel is provided with an RC low-pass filter to limit potential perturbations which might enter the detector from the supply module. Additionally, the iseg module was also occasionally used to bias the active pads of the detector moving the cathode supply channel to the bias input of the Cremat preamplifier and run some tests. The channels were all set to negative polarity except for when one of the channels was biasing the pads, where the channel at issue was set to positive polarity.

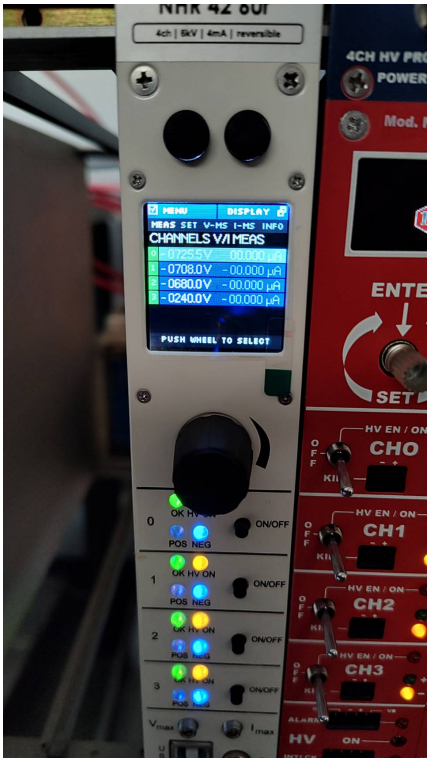


Figure 5.7: *Picture of the iseg NHR 42 60r power supply.*

## 5.2 Ion tail suppression with $\alpha$ source

The choice of the source of ionizing particles was established after multiple signal observation attempts. An Am-241 source was chosen over the more commonly used Fe-55 source because of its much higher ionization yield. Two possible drawbacks of the selection consist in the uniform spreading of the primary ionization electrons all along the 6 *mm* drift path compared to the point-like ionization of Fe-55, and the space charge effects that could potentially occur due to the very high ionization density. Depending on the availability, UV photons could also be a good candidate to generate signal in the detector. Indeed, UV photons that are energetic enough can photoextract an electron from the top copper surface of the detector, inducing an avalanche in the detector.
*Figure 5.8* displays the average waveform of 1000 events in pure-bottom, mid-bottom and mid-mesh configuration in T2K gas mixture, where mid-mesh amplifies only between the two meshes, pure-bottom (the "bottom gap" in *Section 4.4*) only between lower mesh and anode and mid-bottom in both layers. It is clearly visible that the tail in the mid-mesh configuration is much more suppressed than the other two situations where multiplication also occurs in the bottom layer. To prove that the tails shown in the plots are indeed the ion component of the signals, these plots must be compared with the simulation results shown in *Figure 4.26*. The behavior of the induced signal in the simulations does match the detector waveforms' one, since the first step in the simulated waveform (the only realistically visible one in a detector) in mid-mesh configuration is smaller in amplitude

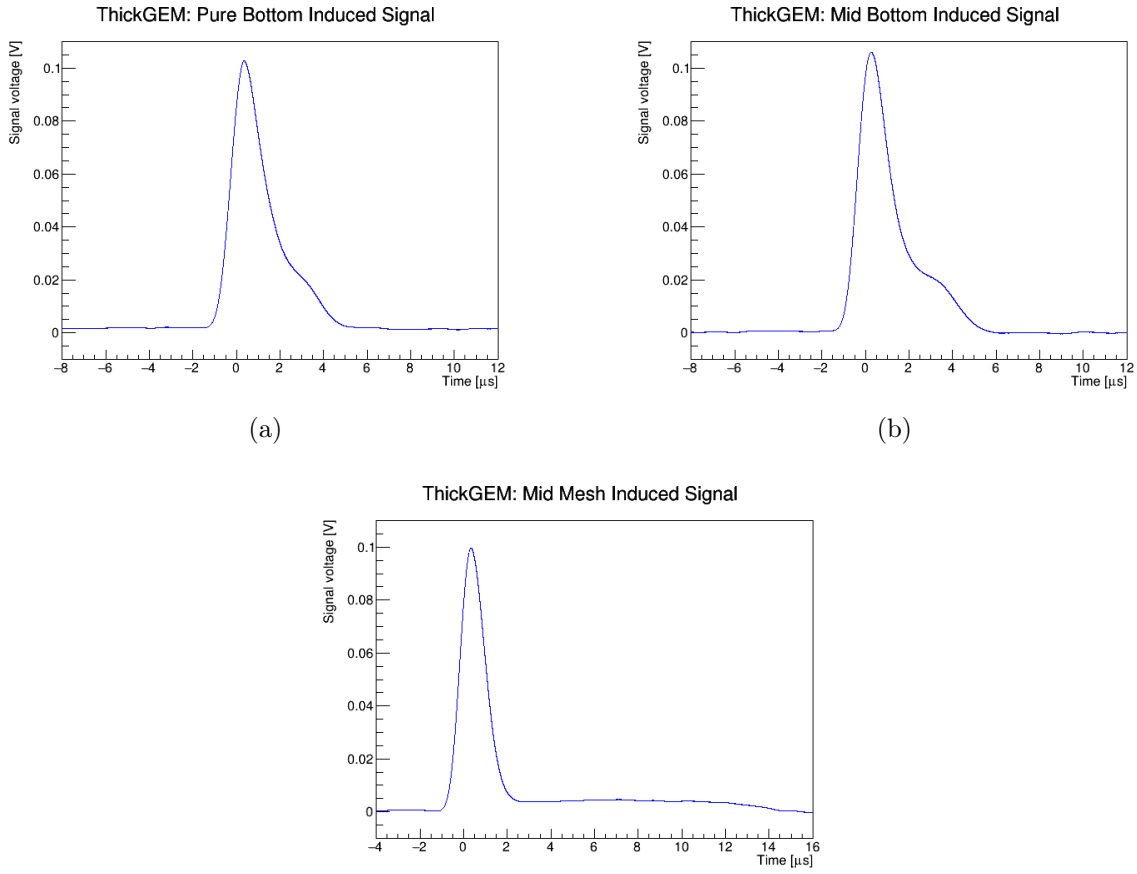


Figure 5.8: *Average waveform of 1000 events in pure-bottom (5.8a), mid-bottom (5.8b) and pure-bottom configuration (5.8c) in T2K gas. Field intensities and electrode potentials are summarized in Table 5.1.*

and longer in time. This effect is mainly due to two causes: the lower field intensity in the bottom region that stretches the signal in time and the screening effect of the lower mesh separating the anode plane from the ions generated between the meshes.
It is interesting to see that the ion tail is still visible after processing the waveform with a shaper, because the signal extends for a long time interval of few $\mu s$, well above the shaping time set on the amplifier (0.5 $\mu s$). Indeed, it was observed that increasing the shaping time of the amplifier to the length of the signal makes the tail disappear reducing the signal to a simple gaussian peak.
Since these signals are processed by a charge sensitive pre-amplifier and the response of a charge sensitive amplifier is proportional to the input charge, the voltage amplitude of the processed signal at the output of the shaping amplifier is proportional to the charge induced on the anode in the shaping time interval. This means that the amplitude of the peak of the final waveforms are proportional to the charge and not to the current induced by the charged particles on the pads in the detector. In other terms, even though the suppression of the tail is quite evident in the plots, it is not possible to use these data

| Voltages [$V$] | | | |
|---|---|---|---|
| Electrode | Pure-Bottom | Mid-Bottom | Mid-Mesh |
| Cathode | -974 | -1120 | -860 |
| Top (Copper) | -884 | -1030 | -770 |
| Upper Mesh | -860 | -990 | -730 |
| Lower Mesh | -740 | -660 | -240 |

| Electric Field [$V/cm$] | | | |
|---|---|---|---|
| Layer | Pure-Bottom | Mid-Bottom | Mid-Mesh |
| Drift | 150 | 150 | 150 |
| Top | 600 | 1000 | 1000 |
| Mid-Mesh | 6000 | 16500 | 24500 |
| Bottom | 18500 | 16500 | 6000 |

| Multiplication region | | | |
|---|---|---|---|
| Layer | Pure-Bottom | Mid-Bottom | Mid-Mesh |
| Drift | × | × | × |
| Top | × | × | × |
| Mid-Mesh | × | ○ | ○ |
| Bottom | ○ | ○ | × |

Table 5.1: *Tables summarizing the voltages of the electrodes, the electric fields in the different detector layers and the amplification regions in the various configurations. The anode pads are grounded in every configuration.*

to have an estimate of the suppression factor because they are not proportional to the original time profile of the signal current.
The tail suppression factor can be quantified by using a different FEE setup, replacing pre-amplifier and amplifier with a broadband fast amplifier, which outputs a waveform whose voltage amplitude is proportional to the induced current and has a limited impact on the time profile of the original signal. However these amplifiers are much more sensitive to noise and have a narrower band width compared to the former setup, making it difficult to see a clear signal. Work is currently still in progress in this sector, and more results are expected to come in the near future.

## 5.3 Time profile analysis in T2K gas mixture

An analysis of the time profile of the signals is a good start to get a solid idea of the signal structure and the requirements of the fast amplifier to be able to see a distinct signal. Since the shaper integrates over a relatively large shaping time and has a large impact on the time profile of the signal, it is not possible to deduce much information on the original signal structure. Therefore this section will study the signal sent out directly from the charge sensitive pre-amplifier to the oscilloscope. The pre-amplifier signal output is a voltage amplitude which is proportional to the integral of the signal current, therefore to the charge induced on the anode pads in the detector. Additionally, a charge sensitive pre-amplifier is characterized by a very slow exponential decay to the baseline (the nominal decay time constant of CR-110 is 140 $\mu s$), meaning that the voltage increase on the occasion of an event is maintained for much longer than a typical signal length.
*Figure 5.9* is the output of the pre-amplifier on the occasion of a sample signal induced in the detector by the $\alpha$ source in T2K gas mixture. Comparing this signal with the simulation results displayed in *Figure 4.27* can help to understand the structure of the waveform in the plot. The slope can be split in two sections: a steep section followed by a gentler section. The first section is not as steep as in the simulation ideal case, but is expected to be caused mainly by the electrons in the detector. The second section is gentler and extends for longer and is expected to be the result of the ions drifting.
The data collected by the pre-amplifier was processed by a noise rejection algorithm that rejects "noise type" events and "discharge type" events. Noise type events are simple fluctuation of the baseline that wrongly triggered the oscilloscope, and they can be mostly

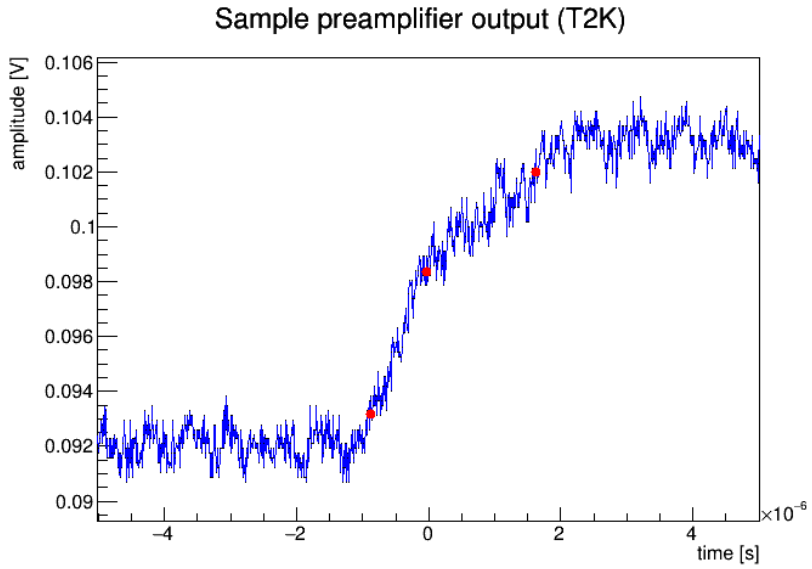


Figure 5.9: *Pre-amplifier output of a sample event induced by an $\alpha$ source in T2K gas mixture. The red markers indicate from the left the points at which the slope reaches 10% of its maximum height, the point where the slope changes and the point at 90% of the maximum height.*

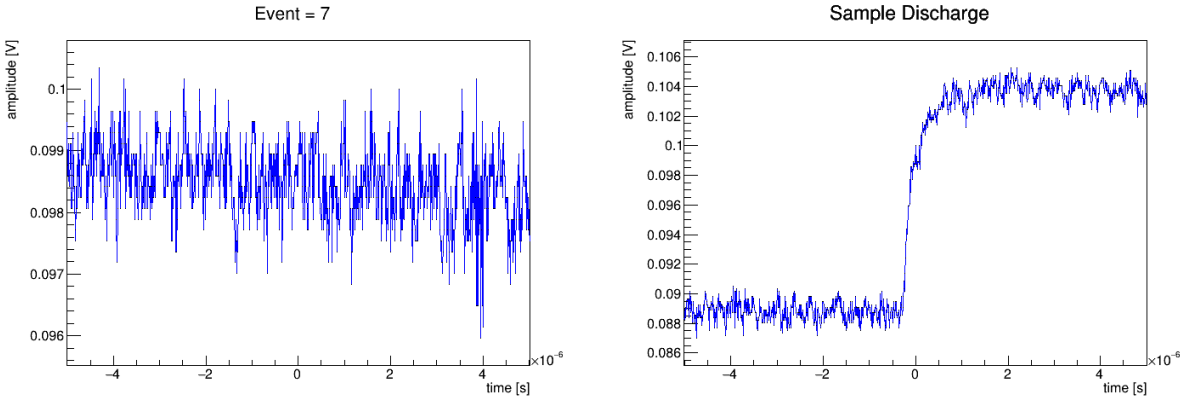


(a) (b)

Figure 5.10: *Noise type event (5.10a) and discharge type event (5.10b) sample.*

removed by checking the variation of the signal amplitude at the beginning and at the end of the waveform. Discharge type events are discharges that occur at high field intensities between the anode pads and the detector. It presents as a very steep signal that has a lower risetime compared to the source induced signals, therefore they can be mostly rejected checking their risetime. However only a relatively small fraction of events survived this rejection algorithm, because a low frequency noise caused a non negligible fluctuation of the baseline, activating the oscilloscope trigger inaccurately at a quite high frequency. *Figure 5.11* displays the distribution of the risetime resulting from the analysis on a dataset of 1000 waveforms in T2K gas mixture setting the detector in the mid-bottom configuration in *Table 5.1*. The risetime is here defined as the time interval between the timings at which the signal amplitude reaches 10% and 90% of the amplitude difference

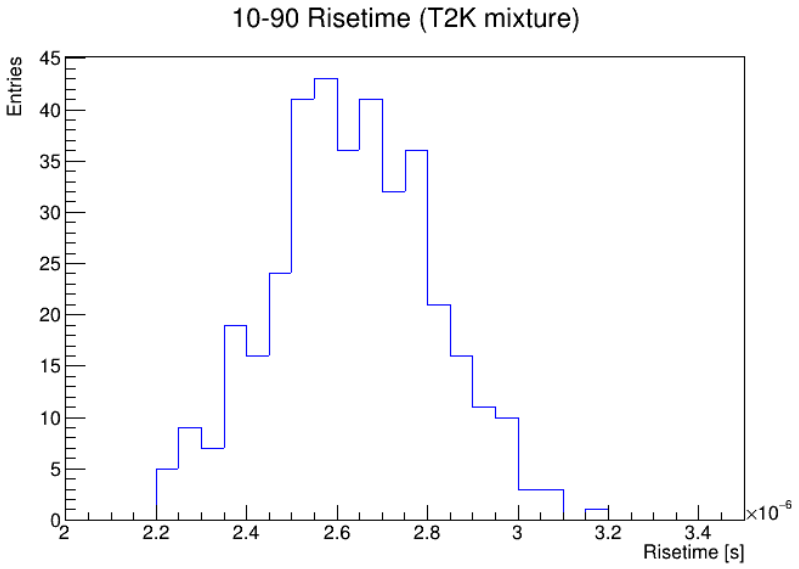


Figure 5.11: *Distribution of the risetime (from 10% to 90% of the maximum height) of the 374 waveforms surviving the noise event rejection algorithm.*

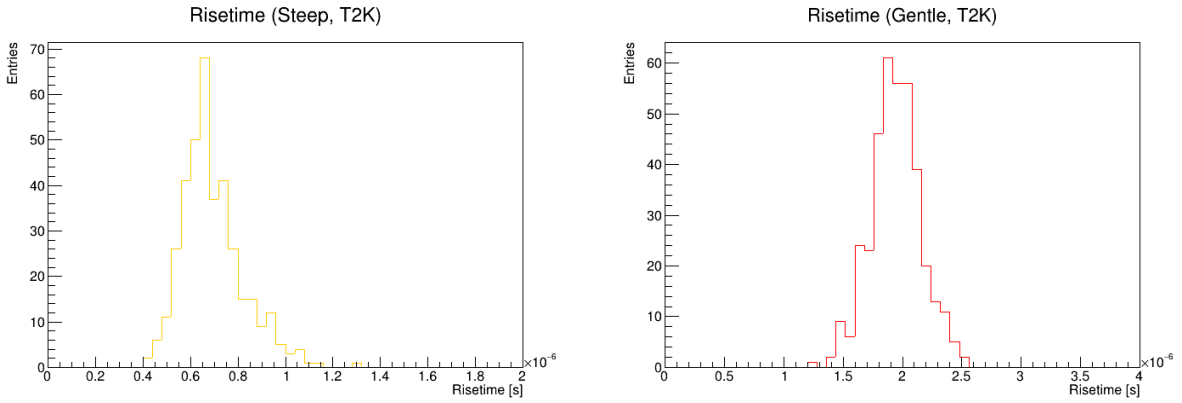


(a) (b)

Figure 5.12: *Distribution of the early section (5.12a) and late section (5.12b) of the risetime of the 374 waveforms surviving the noise event rejection algorithm.*

between the baseline before and the plateau after the signal. The time distribution of the first and second sections of the risetime are considered separately in *Figure 5.12*.
Applying a gaussian fit to the obtained distributions, the mean risetime turns out to be $(2.6 \pm 0.2)\ \mu s$, which can be split in an early steep rise of $(0.65 \pm 0.09)\ \mu s$ and a late slope lasting $(1.9 \pm 0.2)\ \mu s$. The reason of such a long first section is still unclear: 650 $ns$ is a long time interval for an electron to drift for few hundreds of $\mu m$. This result can even lead to suspect that this slope is not simply caused by the electrons, but that there are effects such as the convolution of the ion and electron signal causing the rise to stretch in time. Indeed, the use of an $\alpha$ source lead to a smearing of the signal caused by the large quantity of primary ionization electrons generated along the whole drift volume. Considering that the electrons at the set field have a drift velocity of $\approx 6\ cm/\mu s$ and that the drift height is about 6 $mm$, the expected smearing of the electron peak would be $\approx$ 100 $ns$, which is however still too fast to explain such slow signal.
Regardless of the cause, the crucial point is the fact that the signal is very slow, as it is few $\mu s$ long when most MPGD applications work at the $ns$ scale. This implies that this detector requires a fast amplifier having its bandwidth at lower frequencies compared to the standard fast amplifiers. Indeed, a 3 $\mu s$ risetime would imply a bandwidth minimum of about 300 $kHz$ at most to maximize the signal output without cutting low frequency components.
Moreover, the analysis of the amplitude of these signals brings out another interesting issue. The amplitude of the signal in $V$ can be converted to the amount of charged induced on the anode by applying

$$Q = \frac{V}{ke} \tag{5.1}$$

where $k = 1.4\ V/pC$ is the preamplifier conversion factor from charge to voltage. This conversion results in a mean induced charge of $(3.1 \pm 0.7)\cdot 10^4\ e$ per signal. However,

Monte Carlo simulations at such field intensities return signals inducing even above $3Me$ on the anode, implying a mismatch of two orders of magnitude between simulations and experimental results[9]. Garfield++ does not consider space charge effects that occur at high field intensities, so a mismatch between the two results is to be expected at a certain extent. It must also be considered that in an experimental setup the use of $\alpha$ particles usually generate multiple primary electrons, while the simulations are run starting from a single electron. This means that in absence of space charge effects the experimental data is expected to have a larger induced charge compared to the simulations. Therefore how much the space charge affects the effective gain is not deducible in a simple manner from this result. Additionally, the T2K gas mixture still has a lot of unknowns and there might be additional external factors that contribute to the reduction of the multiplication factor of the detector, such as the behavior of some ions in the gas.

## 5.4 Simulation reliability in Ar-$CO_2$ mixture

To better study the influence of the space charge effect in the DMM, simulations and experimental datasets were taken using an 85:15 Ar-$CO_2$ gas mixture, well known in literature and well implemented in Garfield++.
This test compares simulation and experimental data in the same detector configuration in Ar-$CO_2$ mixture, to see how similar the results are in a mainstream gas composition at high field intensities that induce charge multiplication. The simulations were run starting from a single electron released in the drift region of the detector. The experimental data was taken using the charge sensitive pre-amplifier similarly to *Section 5.3*. The results are summarized in *Figure 5.13*, *Figure 5.14* and *Table 5.2*.
The results turn out to be quite different between the two cases. The mean risetime of the experimental data turns out to be about twice the value given by the simulations, while the induced charge even follows a different distribution and its mean value differs of about a order of magnitude.
This discrepancy can be attributed to multiple causes. Firstly, the mismatch between the two distributions can be explained by the fact that the experimental setup uses an alpha source generating multiple primary electrons, while the simulations start from a single electron. Indeed, the polya distribution represents the distribution of the gain of a single electron in an electric field inducing multiplication, which is proportional to the charge induced on the anode, and it does not describe the overlap of multiple avalanches coming from a large number of primary electrons. This might also contribute

[9] Because of the large gain at these field intensities, Monte Carlo Simulations in T2K gas at these field intensities are very heavy computationally, therefore it was not realistic to have a large dataset of simulated events. The mismatch between the two scenarios is anyways still really evident. This is also an additional reason on why Ar-$CO_2$ simulations were run in *Section 5.4*.

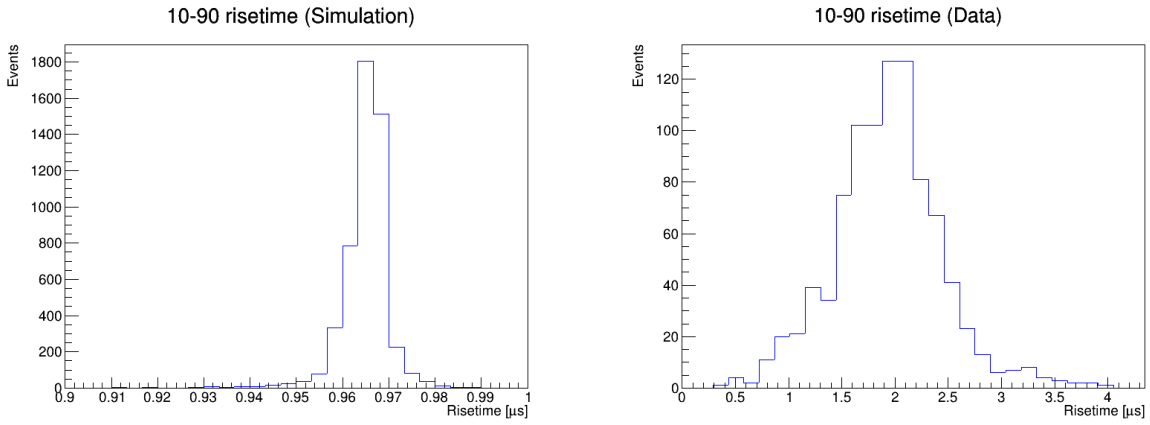


(a) (b)

Figure 5.13: *10% to 90% risetime distribution of simulated induced charge data (5.13a) and experimental pre-amplifier data (5.13b) in Ar-$CO_2$ gas mixture.*

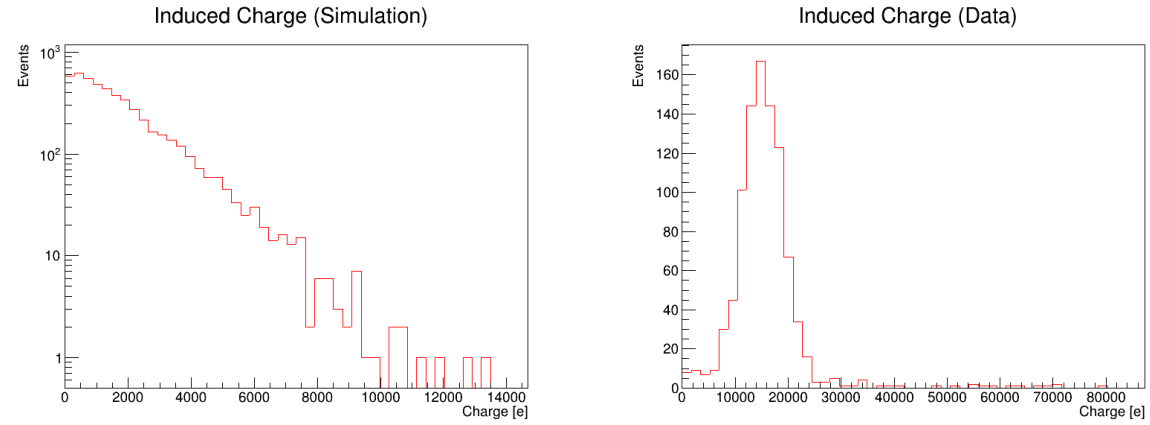


(a) (b)

Figure 5.14: *Charge induced on the detector anode in simulation data (5.13a) and signal amplitude proportional to the induced charge of the experimental pre-amplifier data (5.13b) in Ar-$CO_2$ gas mixture.*

to the larger mean gain value and risetime value too. Indeed, if an experimental signal is made by an overlap of multiple avalanches, its time span is longer since each avalanche starts at a slightly different timing and lasts for a different period of time. Secondly, the experimental setup triggers more easily on large signals, while smaller signals often blend with the noise and are simply more difficult to identify, also considering the non-negligible fluctuations of the baseline. It should also be stressed that the mean value of the experimental data is approximately equal to the upper end of the polya distribution of the simulation results, and that the mismatch between the results is still understandable compared to the mismatch of a factor above 100 in the T2K gas. Space charge effects have a limited impact on these results, since they should reduce the effective field in the detector and therefore the size of the electron avalanches in the detector, leading to a smaller charge induction on the anode in the experimental case. This is the opposite

| | Simulation | Data |
|---|---|---|
| Risetime | $(0.965 \pm 0.003)\ \mu s$ | $(1.9 \pm 0.4)\ \mu s$ |
| Mean Induced Charge | $(1.76 \pm 0.02) \cdot 10^3\ e$ | $(1.5 \pm 0.4) \cdot 10^4\ e$ |
| Charge distribution | Polya | Gaussian |

| Layer | Electric Field $[V/cm]$ | Multiplication |
|---|---|---|
| Drift | 600 | $\times$ |
| Top | 5000 | $\times$ |
| Mid-Mesh | 20000 | $\circ$ |
| Bottom | 23000 | $\circ$ |

Table 5.2: *Summary of Ar-$CO_2$ gas mixture simulation-experimental data comparison and field configuration in the detector.*

behavior of what can be seen by the results, so it is possible to say that the other factors have a major impact on the issue.
However, all things considered, there are two considerations that can be stated looking at these results. Firstly, even though the mismatch between experiment and simulations, the Ar-$CO_2$ results have a comparable order of magnitude and are still realistic. On the other hand, T2K mixture results are not comparable in any way, since experimental data induce a charge on the anode which is orders of magnitude smaller than the simulation predictions. Putting together this fact with the limited impact of the space charge effect in the Ar-$CO_2$ case, it is possible to say that there is still an unknown factor affecting charge multiplication in the T2K gas mixture. Even though the gas composition is different in the two mixtures, it is unlikely to say that space charge effects have such a large impact on the avalanches, and it would be more natural to think to different issues bound for instance to the composition of the gas mixture and to the properties of the ions generated in the gas.

# Conclusions

Monte Carlo simulations of the double-meshed DMM detector in T2K gas mixture led to a deeper understanding of the detector and its capabilities. By correctly tuning the voltages of the electrodes, it is possible to suppress the ion component of the current signal induced on the anode readout and isolate the electron-induced peak. The suppression factor of the ion-induced tail is predicted to be $\approx 10$ compared to an event in a standard micromegas. This suppression was also observed in the experimental setup by means of a charge sensitive amplifier and a shaping amplifier, successfully verifying the operation of the detector. This confirmation makes the next step possible, which is the study and the application of the signal in a detector with resistive anode. Attempts to see the signal using a broadband fast amplifier are still being made to have an experimental value of the tail suppression factor. In the meantime, comparing the results with Ar-$CO_2$ mixture data, it was found out that the T2K gas mixture might have unclear properties that affect the charge multiplication process in the gas, limit the development of the electron avalanche and lead to a mismatch between the data collected by the detector and Monte Carlo simulations. Future studies on the composition of the ions and their mobilities in the gas mixture will bring a more detailed knowledge on the processes occurring in the detector, allowing further applications on Micro Pattern Gaseous Detectors and on the gaseous detectors of T2K.

# Bibliography


[1] S. Navas et al. "Review of Particle Physics". In: *Phys. Rev. D* 110 (3 Aug. 2024), p. 030001. DOI: 10.1103/PhysRevD.110.030001. URL: https://link.aps.org/doi/10.1103/PhysRevD.110.030001.

[2] A. Bettini. "A Brief History of Neutrino". In: *Adv. Ser. Direct. High Energy Phys.* 28 (2018), pp. 1–36. DOI: 10.1142/9789813226098_0001.

[3] N. G. Cooper. *Los Alamos Science, Number 25 – 1997: Celebrating the neutrino*. Tech. rep. Los Alamos National Lab. (LANL), Los Alamos, NM (United States), Dec. 1997. DOI: 10.2172/569122. URL: https://www.osti.gov/biblio/569122.

[4] M. Kleesiek et al. "$\beta$-Decay spectrum, response function and statistical model for neutrino mass measurements with the KATRIN experiment". In: *The European Physical Journal C* 79.3 (Mar. 2019). ISSN: 1434-6052. DOI: 10.1140/epjc/s10052-019-6686-7. URL: http://dx.doi.org/10.1140/epjc/s10052-019-6686-7.

[5] M. Agostini et al. "Final Results of GERDA on the Search for Neutrinoless Double-$\beta$ Decay". In: *Phys. Rev. Lett.* 125 (25 Dec. 2020), p. 252502. DOI: 10.1103/PhysRevLett.125.252502. URL: https://link.aps.org/doi/10.1103/PhysRevLett.125.252502.

[6] S. Abe et al. "Search for Majorana Neutrinos with the Complete KamLAND-Zen Dataset". In: (June 2024). arXiv: 2406.11438 [hep-ex].

[7] J. H. Christenson et al. "Evidence for the $2\pi$ Decay of the $K_2^0$ Meson". In: *Phys. Rev. Lett.* 13 (4 July 1964), pp. 138–140. DOI: 10.1103/PhysRevLett.13.138. URL: https://link.aps.org/doi/10.1103/PhysRevLett.13.138.

[8] B. Aubert et al. "Observation of *CP* Violation in the $B^0$ Meson System". In: *Phys. Rev. Lett.* 87 (9 Aug. 2001), p. 091801. DOI: 10.1103/PhysRevLett.87.091801. URL: https://link.aps.org/doi/10.1103/PhysRevLett.87.091801.

[9] K. Abe et al. "Observation of Large *CP* Violation in the Neutral $B$ Meson System". In: *Phys. Rev. Lett.* 87 (9 Aug. 2001), p. 091802. DOI: 10.1103/PhysRevLett.87.091802. URL: https://link.aps.org/doi/10.1103/PhysRevLett.87.091802.

[10] R. Aaij et al. "Observation of *CP* Violation in Charm Decays". In: *Phys. Rev. Lett.* 122 (21 May 2019), p. 211803. DOI: 10.1103/PhysRevLett.122.211803. URL: https://link.aps.org/doi/10.1103/PhysRevLett.122.211803.

[11] Pablo Fernández. "Recent results from the long-baseline (LBL) neutrino oscillation experiments". In: *SciPost Phys. Proc.* (2019), p. 029. DOI: 10.21468/SciPostPhysProc.1.029. URL: https://scipost.org/10.21468/SciPostPhysProc.1.029.

[12] Hyper-Kamiokande Proto-Collaboration et al. *Hyper-Kamiokande Design Report*. 2018. arXiv: 1805.04163 [physics.ins-det]. URL: https://arxiv.org/abs/1805.04163.

[13] B. Abi et al. *Deep Underground Neutrino Experiment (DUNE), Far Detector Technical Design Report, Volume I: Introduction to DUNE*. 2020. arXiv: 2002.02967 [physics.ins-det]. URL: https://arxiv.org/abs/2002.02967.

[14] In: *Progress in Particle and Nuclear Physics* 123 (Mar. 2022), p. 103927. ISSN: 0146-6410. DOI: 10.1016/j.ppnp.2021.103927. URL: http://dx.doi.org/10.1016/j.ppnp.2021.103927.

[15] K. Abe et al. "The T2K experiment". In: *Nuclear Instruments and Methods in Physics Research Section A: Accelerators, Spectrometers, Detectors and Associated Equipment* 659.1 (Dec. 2011), pp. 106–135. ISSN: 0168-9002. DOI: 10.1016/j.nima.2011.06.067. URL: http://dx.doi.org/10.1016/j.nima.2011.06.067.

[16] T2K collaboration. *Tokai-to-Kamioka (T2K) Long Baseline Neutrino Oscillation Experiment Proposal*. 2006. URL: https://j-parc.jp/researcher/Hadron/en/pac_0606/pdf/p11-Nishikawa.pdf.

[17] M Friend. "J-PARC accelerator and neutrino beamline upgrade programme". In: *Journal of Physics: Conference Series* 888.1 (Sept. 2017), p. 012042. DOI: 10.1088/1742-6596/888/1/012042. URL: https://dx.doi.org/10.1088/1742-6596/888/1/012042.

[18] A.K. Ichikawa. "Design concept of the magnetic horn system for the T2K neutrino beam". In: *Nuclear Instruments and Methods in Physics Research Section A: Accelerators, Spectrometers, Detectors and Associated Equipment* 690 (Oct. 2012), pp. 27–33. DOI: 10.1016/j.nima.2012.06.045.

[19] K. Abe et al. "Measurement of the muon neutrino inclusive charged-current cross section in the energy range of 1–3 GeV with the T2K INGRID detector". In: *Phys. Rev. D* 93 (7 Apr. 2016), p. 072002. DOI: 10.1103/PhysRevD.93.072002. URL: https://link.aps.org/doi/10.1103/PhysRevD.93.072002.

[20] K. Abe et al. "Measurements of the T2K neutrino beam properties using the INGRID on-axis near detector". In: *Nuclear Instruments and Methods in Physics Research Section A: Accelerators, Spectrometers, Detectors and Associated Equipment* 694 (Dec. 2012), pp. 211–223. ISSN: 0168-9002. DOI: 10.1016/j.nima.2012.03.023. URL: http://dx.doi.org/10.1016/j.nima.2012.03.023.

[21] S. Assylbekov et al. "The T2K ND280 off-axis pi–zero detector". In: *Nuclear Instruments and Methods in Physics Research Section A: Accelerators, Spectrometers, Detectors and Associated Equipment* 686 (Sept. 2012), pp. 48–63. ISSN: 0168-9002. DOI: 10.1016/j.nima.2012.05.028. URL: http://dx.doi.org/10.1016/j.nima.2012.05.028.

[22] K. Abe et al. *T2K ND280 Upgrade – Technical Design Report*. 2020. arXiv: 1901.03750 [physics.ins-det]. URL: https://arxiv.org/abs/1901.03750.

[23] Claudio (LPNHE Paris) Giganti, Thorsten (IFAE Barcelona) Lux, and Masashi (University of Tokyo) Yokoyama. *NP07: ND280 Upgrade project*. Tech. rep. Geneva: CERN, 2020. URL: https://cds.cern.ch/record/2713578.

[24] T Ovsiannikova et al. "The new experiment WAGASCI for water to hydrocarbon neutrino cross section measurement using the J-PARC beam". In: *Journal of Physics: Conference*

*Series* 675.1 (Jan. 2016), p. 012030. DOI: 10.1088/1742-6596/675/1/012030. URL: https://dx.doi.org/10.1088/1742-6596/675/1/012030.

[25] M. Antonova et al. "Baby MIND: A Magnetised Spectrometer for the WAGASCI Experiment". In: *Prospects in Neutrino Physics*. Apr. 2017. arXiv: 1704.08079 [physics.ins-det].

[26] S. Fukuda et al. "The Super-Kamiokande detector". In: *Nuclear Instruments and Methods in Physics Research Section A: Accelerators, Spectrometers, Detectors and Associated Equipment* 501.2 (2003), pp. 418–462. ISSN: 0168-9002. DOI: https://doi.org/10.1016/S0168-9002(03)00425-X. URL: https://www.sciencedirect.com/science/article/pii/S016890020300425X.

[27] Yoichiro Suzuki. "The Super-Kamiokande experiment". In: *Eur. Phys. J. C* 79.4 (2019), p. 298. DOI: 10.1140/epjc/s10052-019-6796-2.

[28] Yasuo Takeuchi. "Recent oscillation results and future prospects of Super-Kamiokande". In: *PoS* NOW2022 (2023), p. 004. DOI: 10.22323/1.421.0004.

[29] K. Abe et al. "Second gadolinium loading to Super-Kamiokande". In: *Nuclear Instruments and Methods in Physics Research Section A: Accelerators, Spectrometers, Detectors and Associated Equipment* 1065 (Aug. 2024), p. 169480. ISSN: 0168-9002. DOI: 10.1016/j.nima.2024.169480. URL: http://dx.doi.org/10.1016/j.nima.2024.169480.

[30] Fabio Sauli. *Gaseous Radiation Detectors: Fundamentals and Applications*. Cambridge Monographs on Particle Physics, Nuclear Physics and Cosmology. Cambridge University Press, 2023.

[31] H. J. Hilke. "Time projection chambers". In: *Rept. Prog. Phys.* 73 (2010), p. 116201. DOI: 10.1088/0034-4885/73/11/116201.

[32] S. Levorato and on behalf of the T2K HATPC upgrade group. "Technical challenges for the new T2K ND280 High Angle TPCs". In: *Journal of Instrumentation* 20.04 (Apr. 2025), p. C04025. DOI: 10.1088/1748-0221/20/04/C04025. URL: https://dx.doi.org/10.1088/1748-0221/20/04/C04025.

[33] Özkan Şahin, Tadeusz Z Kowalski, and Rob Veenhof. "High-precision gas gain and energy transfer measurements in Ar–CO2 mixtures". In: *Nucl. Instrum. Methods Phys. Res., A* 768 (2014), pp. 104–111. DOI: 10.1016/j.nima.2014.09.061. URL: https://cds.cern.ch/record/2003219.

[34] T. Zerguerras et al. "Understanding avalanches in a Micromegas from single-electron response measurement". In: *Nucl. Instrum. Meth. A* 772 (2015), pp. 76–82. DOI: 10.1016/j.nima.2014.11.014.

[35] Fabio Sauli and Archana Sharma. "MICROPATTERN GASEOUS DETECTORS". In: *Annual Review of Nuclear and Particle Science* 49.Volume 49, 1999 (1999), pp. 341–388. ISSN: 1545-4134. DOI: https://doi.org/10.1146/annurev.nucl.49.1.341. URL: https://www.annualreviews.org/content/journals/10.1146/annurev.nucl.49.1.341.

[36] Y. Giomataris et al. "MICROMEGAS: a high-granularity position-sensitive gaseous detector for high particle-flux environments". In: *Nuclear Instruments and Methods in Physics Research Section A: Accelerators, Spectrometers, Detectors and Associated Equipment* 376.1 (1996), pp. 29–35. ISSN: 0168-9002. DOI: https://doi.org/10.1016/0168-9002(96)00175-1. URL: https://www.sciencedirect.com/science/article/pii/0168900296001751.

[37] D. Attié et al. "Characterization of resistive Micromegas detectors for the upgrade of the T2K Near Detector Time Projection Chambers". In: *Nuclear Instruments and Methods in Physics Research Section A: Accelerators, Spectrometers, Detectors and Associated Equipment* 1025 (Feb. 2022), p. 166109. ISSN: 0168-9002. DOI: 10.1016/j.nima.2021.166109. URL: http://dx.doi.org/10.1016/j.nima.2021.166109.

# Acknowledgements

I would like to thank all the people that made this work possible.

Prof. Giannmaria Collazuol for offering me the opportunity to work on this topic and have unforgettable experiences.

All the members of the T2K Padova group, Stefano Levorato, Daniele D'Ago, Camilla Forza, Marco Mattiazzi and Matteo Feltre for all the support they provided me during this work. In particular, Stefano for the technical assistance and bringing me on the right track when necessary, and Daniele for his help and guidance throughout this work. I'd also like to thank David Henaff for his support on software-related technicalities.

My mother and Diego, who supported me during my studies and allowed this long journey to come to an end.